Scuola Internazionale Superiore di Studi Avanzati
Theoretical Particle Physics

Search for an Invisibly Decaying Higgs Boson Produced via Vector Boson Fusion using the ATLAS Detector

Truong Thi Ngoc Loan
Supervisor: Bobby Acharya

September 17, 2015

Contents

List of Figures

List of Tables

Acknowledgements

Studying is a long journey, I would like to firstly thank my family for encouraging and supporting me along the way. Doing research implies to try and fail many times, it is important to have guidances to not get lost in the wrong tracks. I would like to thank my supervisor Bobby Acharya for giving me wise advices when needed. Working with the VBF Higgs to invisible group is a great experience for me, I would like to thank my very nice guide in the working group Ketevi Adikle Assamagan. Also to thank Bill Quayle, the working group convener, for being always patient and kind to explain things in detail, willingly provides help if needed. Thanks to Reyhaneh Rezvani, Rami Vanguri, Andy White and many others whom I have been working with in the group. I would like to thank Aaron Armbruster, who is not in the VBF working group however was willing to help us in many issues. For my service task, I have received kind instruction and help from Anthony Morley and Silvia Miglioranzi, thanks to both of you. Being in the ATLAS Udine/ICTP group is a great pleasure. Thanks much to Kate Shaw for extensive wonderful instructions in researches and collaboration in outreach activities. Many thanks to my colleagues Michele Pinamonti, Rachik Soualah for the plenty of discussions. Also thank to Leonid Serkin for many wise and kind encouraging advices, to Alexey Boldyrev for checking this thesis. Big thanks to the team leader Marina Cobal, in spite of being busy with a lot of work, still takes well care of us. Thanks to my friends who were or is now in the ATLAS experiment: Fabrice Balli and Tran Huong Lan for great companions. Thanks to many professors at ICTP and SISSA for the things I could learn from them and for inspiring ideas, working attitudes. Five years in Italy would not have been this memorable without the Vietnamese group, not needed to mention each name, thanks to you all for being always beside me. Also thank to my many friends and classmates especially Saeede Nafooshe for her great friendship.

Chapter 1

Introduction

The Standard Model (SM) of particle physics has been extremely successful at describing the fundamental particles and forces that make up our Universe, and the recent discovery in July 2012 of the Higgs boson using proton-proton collision data at 7 and 8 TeV at the LHC completed this theory.

Despite the success of the SM a number of observed phenomena are not described; the model does not include a description of Gravity, it cannot describe the neutrino masses, dark matter or dark energy, and there is the hierarchy problem which has to do with the fact that the Higgs boson mass is so light compared to the Planck mass. All this indicates there must be physics Beyond the Standard Model (BSM).

Dark matter is the name given to the unknown and unobservable matter that makes up approximately 25% of our Universe. Astrophysical observations provide strong evidence for dark matter that could be explained by the existence of weakly interacting massive particles (WIMP), see Ref. [1] and the references therein. The observed Higgs boson with a mass of about 125 GeV [2,3] might decay to dark matter or long-lived massive particles [4–8], provided this decay is kinematically allowed. This is referred to as an invisible decay of the Higgs boson. In the SM, the process $H \to ZZ \to 4\nu$ is an invisible decay of the Higgs boson, but the branching ratio is 1.2×10^{-3} [9,10], which is below the sensitivity of the search presented in this thesis.

This thesis presents a search for the Higgs boson produced via the vector boson fusion (VBF) process and decaying invisibly [11]. In addition to that, a combination of all the direct searches for Higgs boson decaying into invisible particles done by ATLAS [12] is described. The search is performed with a dataset corresponding to an integrated luminosity of 20.3 fb^{-1} of proton-proton (pp) collisions at $\sqrt{s} = 8$ TeV, recorded by the ATLAS detector [13] at the Large Hadron Collider (LHC).

In parallel with the analysis, there have been several other established analyses on direct searches for the invisible decay of the Higgs boson. The CMS Collaboration obtained an upper bound of 58% on the branching fraction of invisible Higgs boson decays using a combination of the VBF and ZH production modes [14]. Weaker limits were obtained using the $Z(\to \ell\ell)H + E_{\mathrm{T}}^{\mathrm{miss}}$ signature by both the ATLAS and CMS collaborations [14, 15], giving upper limits at 95% CL of 75% and 83% on the

branching fraction of invisible Higgs boson decays, respectively. By combining the searches in the $Z(\rightarrow \ell\ell)H$ and $Z(\rightarrow b\bar{b})H$ channels, CMS obtained an upper limit of 81% [14]. Using the associated production with a vector boson, VH, where the vector-boson decays to jets and the Higgs boson to invisible particles, ATLAS set a 95% CL upper bound of 78% on the branching fraction of $H \rightarrow$ invisible [16]. Other searches for large $E_{\mathrm{T}}^{\mathrm{miss}}$ in association with one or more jets were reported in Refs. [17–20]. These searches are less sensitive to Higgs-mediated interactions than the search presented here, because they are primarily sensitive to the ggF process and have significantly larger backgrounds.

In addition to the direct searches, assuming that the couplings of the Higgs boson to SM particles correspond to the SM values, global fits to measurements of cross sections time branching ratios of different channels allow the extraction of a limit on the branching ratio to invisible particles. The 95% CL upper limits on this branching ratio set by ATLAS and CMS are 0.27 and 0.32 respectively [21, 22]. There is an important complementarity between direct searches for invisible decays of Higgs bosons and indirect constraints on the sum of invisible and undetected decays. A simultaneous excess would confirm a signal, while non-zero branching ratio of $H \rightarrow$ invisible in the global fit, but no excess in the Higgs boson decaying to invisible particle searches, would point toward other undetected decays or model assumptions as the source of the global fit result.

In the search present in this thesis, the observed data events are consistent with the background estimations. An upper bound on the cross section times the branching ratio of the Higgs boson decays to invisible particles is computed using a maximum-likelihood fit to the data with the profile likelihood test statistic [23]. A constraint on the branching ratio alone is obtained assuming the SM VBF and ggF production cross sections, acceptances and efficiencies, for a Higgs boson with a mass of 125 GeV. The result is an upper bound of 28% at 95% CL on the branching ratio of the Higgs boson decaying invisibly, better than all the individual previous direct searches.

In the context of models where dark matter couples to the SM particles primarily through the Higgs boson [24], limits on the branching ratio of the Higgs boson decaying invisibly can be interpreted in WIMP-nucleon interaction models [25] and compared directly to experiments which search for dark matter particles via their direct interaction with the material of a detector [26–34]. The constraints on the WIMP-nucleon cross section resulting from the limit on invisible decays of the Higgs boson are complementary to those from direct detection experiments, in the sense that collider searches cover the mass region where direct detection experiments have less sensitivity [35].

I contributed to various parts of the analyses. For the direct search, I participated in the acceptance challenge to define the set of all the cuts designed to optimize signal and background separation, the dominant W+jets background determination, limit setting procedure and various uncertainties estimates. Moreover, I worked for the validation of the fitting methods for this analysis and for the combination of all the

direct searches for invisible decay of the Higgs boson.

The thesis is organized as follows. The Higgs boson and Higgs mechanism in the SM are introduced in Chapter 2. The LHC and ATLAS detector are briefly described in Chapter 3. Different SM processes including the Higgs productions, decay channels and discovery at the LHC are expressed in details in Chapter 4. Physics objects reconstruction is shown in Chapter 5. The search for VBF production of Higgs decaying invisibly is presented in Chapter 6, followed by the combination of all the searches for invisible decays of the Higgs boson at ATLAS in Chapter 7. Finally, concluding remarks are presented in Chapter 8.

Chapter 2

Higgs boson in Standard Model

2.1 Standard Model of particle physics

The SM (also known as Glashow-Weinberg-Salam model), was developed in the second half of the 20^{th} century and finalized in mid-1970s. It describes the electroweak and strong interaction of elementary particles by introducing the gauge group $SU(3)_{\mathrm{C}} \times SU(2)_{\mathrm{L}} \times U(1)_{\mathrm{Y}}$ and using spontaneous symmetry breaking. The model has been tested by a large number of precision measurements and discoveries. Those include the W [36, 37] and Z [38] bosons discovery at the UA1 experiment (also at the UA2 for W-boson) (CERN) in 1983 and the top-quark [39] at Fermilab in 1995. The final piece is the Higgs boson which was discovered in 2012 by ATLAS [40] and CMS [41] experiments at the LHC.

Including the Poincaré group Λ, the symmetry group of the SM is: $SU(3)_{\mathrm{C}} \times SU(2)_{\mathrm{L}} \times U(1)_{\mathrm{Y}} \times \Lambda$. Where $SU(3)_{\mathrm{C}}$ is the symmetry of the strong interaction, where quarks q^{α} ($\alpha = \overline{1,3}$ for three quark generations) are described as fundamental representation and eight gluons G^{a}_{μ} ($a = \overline{1,8}$) are described by the adjoint representation. $SU(2)_{\mathrm{L}}$ is the symmetry of the weak interaction, where left-handed fermions $q^{\alpha}_{L} = \begin{pmatrix} u^{\alpha}_{L} \\ d^{\alpha}_{L} \end{pmatrix}, \ell_{L} = \begin{pmatrix} \nu_{e_{L}} \\ e_{L} \end{pmatrix}$ are described as fundamental representation, three weak gauge bosons A^{i}_{μ} ($i = \overline{1,3}$) are described in the adjoint representation, and no Dirac mass terms for charged particles are allowed. $U(1)_{\mathrm{Y}}$ is the hypercharge gauge group with a gauge boson B_{μ}, other particles have charges assigned depending on their electromagnetic charge Q and isospin quantum number in the third direction T_{3L} of $SU(2)_{\mathrm{L}}$ so that $Q = T_{3L} + \frac{Y}{2}$. The scalar Higgs field is introduced as a doublet (fundamental representation) of $SU(2)_{\mathrm{L}}$. For the rest not mentioned fields in each gauge group, it means that they are singlet under that group. The SM Lagrangian

is then written:

$$\begin{aligned}\mathcal{L}_{SM} &= -\frac{1}{4}(W_i^{\mu\nu}W^i_{\mu\nu} + G_a^{\mu\nu}G^a_{\mu\nu} + B^{\mu\nu}B_{\mu\nu}) + \frac{1}{2}(D^\mu\Phi)^\dagger(D_\mu\Phi) + \\ &+ i\bar{\ell}_L\gamma^\mu D_\mu\ell_L + i\bar{q}_L^\alpha\gamma^\mu D_\mu q_{L\alpha} + i\bar{u}_R^\alpha\gamma^\mu D'_\mu u_{R\alpha} + i\bar{d}_R^\alpha\gamma^\mu D'_\mu d_{R\alpha} + i\bar{e}_R\gamma^\mu D'_\mu e_R + \\ &+ (y_d\bar{q}_L^\alpha\Phi d_{R\alpha} + y_u\bar{u}_L^\alpha\tilde{\Phi}u_{R\alpha} + y_e\bar{\ell}_L\Phi e_R + h.c.) - V(\Phi^\dagger\Phi) \qquad (2.1)\end{aligned}$$

The terms can be explained as below. The first two lines of equation 2.1 are the kinetic terms for gauge fields and fermions, with

$$\begin{aligned}W_i^{\mu\nu} &= \partial^\mu A_i^\nu - \partial^\nu A_i^\mu, \text{ with } i = 1,2,3 \qquad (2.2)\\ G_a^{\mu\nu} &= \partial^\mu G_a^\nu - \partial^\nu G_a^\mu, \text{ with } a = \overline{1,8} \qquad (2.3)\\ B^{\mu\nu} &= \partial^\mu B^\nu - \partial^\nu B^\mu \qquad (2.4)\end{aligned}$$

The first group of terms in the third line is the Yukawa interaction between the Higgs field Φ and the massive fermions and $\tilde{\Phi} = i\sigma_2\Phi^*$, with σ_2 is the second Pauli matrix. The last term is the Higgs potential:

$$V = m^2\Phi^\dagger\Phi + h(\Phi^\dagger\Phi)^2; \text{ with } h \geq 0, m^2 < 0 \qquad (2.5)$$

The quantum numbers: charge, third projection of isospin, hypercharge respectively for different fermion fields in the SM:

	Q	T_3	Y
ν_{e_L}	0	$\frac{1}{2}$	-1
e_L	-1	$-\frac{1}{2}$	-1
e_R	-1	0	-2
u_L^α	$\frac{2}{3}$	$\frac{1}{2}$	$\frac{1}{3}$
d_L^α	$-\frac{1}{3}$	$-\frac{1}{2}$	$\frac{1}{3}$
u_R^α	$\frac{2}{3}$	0	$\frac{4}{3}$
d_R^α	$-\frac{1}{3}$	0	$-\frac{2}{3}$

The transformations of different fields under the $SU(2)_\mathrm{L}$, $U(1)_\mathrm{Y}$ or $SU(2)_\mathrm{L} \times$

$U(1)_{\rm Y}$ groups:

$$\ell_{\rm L}(x) \xrightarrow{SU(2)_{\rm L}} U\ell_{\rm L}(x), \text{ where } U = e^{ig\frac{\overrightarrow{\mathscr{T}}}{2}\overrightarrow{\omega}(x)},$$
$$\overrightarrow{\omega}(x) \text{ are the 3 transform parameters} \tag{2.6}$$

$$q^{\alpha}_{\rm L}(x) \xrightarrow{SU(2)_{\rm L}} Uq^{\alpha}_{\rm L}(x) \tag{2.7}$$

$$\ell_{\rm L}(x) \xrightarrow{U(1)_{\rm Y}} e^{ig\prime\frac{1}{2}(-1)\alpha(x)}\ell_{\rm L}(x),$$
$$\alpha(x) \text{ is the transform parameter} \tag{2.8}$$

$$q^{\alpha}_{\rm L}(x) \xrightarrow{U(1)_{\rm Y}} e^{ig\prime\frac{1}{2}(\frac{1}{3})\alpha(x)}q^{\alpha}_{\rm L}(x) \tag{2.9}$$

$$e_{\rm R}(x) \xrightarrow{U(1)_{\rm Y}} e^{ig\prime\frac{1}{2}(-2)\alpha(x)}e_{\rm R}(x) \tag{2.10}$$

$$u^{\alpha}_{\rm R}(x) \xrightarrow{U(1)_{\rm Y}} e^{ig\prime\frac{1}{2}(\frac{1}{3})\alpha(x)}u^{\alpha}_{\rm R}(x) \tag{2.11}$$

$$d^{\alpha}_{\rm R}(x) \xrightarrow{U(1)_{\rm Y}} e^{ig\prime\frac{1}{2}(-\frac{2}{3})\alpha(x)}d^{\alpha}_{\rm R}(x) \tag{2.12}$$

$$A^{i}_{\mu}(x) \xrightarrow{SU(2)_{\rm L}} A^{i}_{\mu}(x) - (\omega^{j}(x) \times A_{j\mu}(x))^{i} - \frac{1}{g}\partial_{\mu}\omega^{i}(x) \tag{2.13}$$

$$A^{i}_{\mu\nu}(x) \xrightarrow{SU(2)_{\rm L}} A^{i}_{\mu\nu}(x) - (\omega^{j}(x) \times A_{j\mu\nu}(x))^{i} \tag{2.14}$$

$$\text{For } \ell_{\rm L} : \partial_{\mu} \xrightarrow{SU(2)_{\rm L}\times U(1)_{\rm Y}} D_{\mu} = \partial_{\mu} + ig\frac{\overrightarrow{\mathscr{T}}}{2}\overrightarrow{A}_{\mu} + ig'\frac{1}{2}[Y(\ell_{\rm L})]B_{\mu} \tag{2.15}$$

$$\text{For } \psi_{\rm R} : \partial'_{\mu} \xrightarrow{SU(2)_{\rm L}\times U(1)_{\rm Y}} D'_{\mu} = \partial_{\mu} + ig'\frac{1}{2}[Y(\psi_{\rm R})]B_{\mu}$$
$$\text{with } \psi_{\rm R} \text{ is either of } (e_{\rm R}, u_{\rm R}, d_{\rm R}) \tag{2.16}$$

$$B_{\mu} \xrightarrow{U(1)_{\rm Y}} B_{\mu} - \frac{\partial_{\mu}\alpha(x)}{g'} \tag{2.17}$$

$\overrightarrow{\mathscr{T}}$ are three generators of $SU(2)_{\rm L}$.

$$\mathscr{T}_1 = \begin{pmatrix} 0 & 1 \\ 1 & 0 \end{pmatrix} \quad \mathscr{T}_2 = \begin{pmatrix} 0 & -i \\ i & 0 \end{pmatrix} \quad \mathscr{T}_3 = \begin{pmatrix} 1 & 0 \\ 0 & -1 \end{pmatrix} \tag{2.18}$$

The gauge terms can be rewritten as the following:

$$\frac{\overrightarrow{\mathscr{T}}}{2}\overrightarrow{A}_\mu = \frac{\mathscr{T}_3}{2}A^3_\mu + \frac{1}{\sqrt{2}}(\mathscr{T}_+ W_\mu + \mathscr{T}_- W^\dagger_\mu) \tag{2.19}$$

$$\begin{aligned} \text{where } \mathscr{T}_\pm &= \frac{1}{2}(\mathscr{T}_1 \pm i\mathscr{T}_2) \\ \mathscr{T}_+ &= \begin{pmatrix} 0 & 1 \\ 0 & 0 \end{pmatrix} \\ \mathscr{T}_- &= \begin{pmatrix} 0 & 0 \\ 1 & 0 \end{pmatrix} \\ W_\mu &= \frac{A_{1\mu} - iA_{2\mu}}{\sqrt{2}} \end{aligned} \tag{2.20}$$

2.2 The Higgs Mechanism and Yukawa interaction

In the Lagrangian in equation 2.1, there are no mass terms for the weak gauge bosons nor the fermions while in nature they do have masses. The real symmetries observed are the $SU(3)_{\mathrm{C}}$ for strong interaction and $U(1)_{\mathrm{EM}}$ for electromagnetic interaction. Therefore, the original symmetry of the SM must be somehow broken to $SU(3)_{\mathrm{C}} \times U(1)_{\mathrm{EM}}$ and mass terms for the relevant fermions and weak bosons should be generated. That is done via the Higgs mechanism through spontaneous symmetry breaking.

The Higgs mechanism is a mechanism where the Higgs field is introduced to the Lagrangian and satisfies all the gauge invariant requirements so that the symmetries of the theory is preserved. However, the Higgs' vacuum state does not respect the symmetries when it obtains a non-zero vacuum expectation value (vev) which consequently provides mass terms for the corresponding particles. It is based on the "Goldstone theorem" saying that *"There is one Nambu-Goldstone boson for each generator that does not annihilate the vacuum"* applying for a global symmetry. In case of a local gauge symmetry, the "Nambu-Goldstone boson" becomes a pseudo-Nambu-Goldstone boson and is "eaten" by the gauge boson subsequently provides one extra degree of freedom or a mass to the gauge boson.

2.2.1 Spontaneously breaking Gauge Symmetry

Because the vev of the Higgs field takes non vanishing values, it must be a Lorentz scalar (otherwise it would break Lorentz symmetry as well).

For the group $SU(2)_{\rm L} \times U(1)_{\rm Y}$, assume coupling constants: g for $SU(2)_{\rm L}$ and g' for $U(1)_{\rm Y}$, gauges $\overrightarrow{A}_\mu(x)$ for $SU(2)_{\rm L}$ and $B_\mu(x)$ for $U(1)_{\rm Y}$. The aim is to break the symmetry from $SU(2)_{\rm L} \times U(1)_{\rm Y}$ to $U(1)_{\rm EM}$. There are certain choices one can consider:

1. If $\Phi(x)$ is $SU(2)_{\rm L}$ singlet then it cannot break $SU(2)_{\rm L}$
2. If $\Phi(x)$ is $SU(2)_{\rm L}$ triplet $h = \begin{pmatrix} h^+ \\ h^0 \\ h^- \end{pmatrix}$ then h cannot break $U(1)_{\rm Y}$ because h has $Y = 0$ so it cannot break $U(1)_{\rm Y}$. If considering $h = \begin{pmatrix} h^{++} \\ h^+ \\ h^0 \end{pmatrix}$ then $Y(h) \neq 0$ however it leads to wrong ratio of $\frac{m_W}{m_Z}$.
3. The number of degrees of freedom must not conflict with low energy phenomenology. What works for the symmetry breaking in this case is a Higgs doublet $\Phi(x) = \begin{pmatrix} \phi^+ \\ \phi^0 \end{pmatrix}$ which has the quantum numbers:

	Q	T_3	Y
ϕ^+	1	$\frac{1}{2}$	1
ϕ^0	0	$-\frac{1}{2}$	1

It can break the vacuum in two ways: the first way $\langle 0|\phi^+(x)|0\rangle \neq 0$ will cause breaking electric charge Q so it is not preferable, the second way is $\langle 0|\phi^0(x)|0\rangle \neq 0$ works. Then one has to choose the potential for obtaining $\langle 0|\phi^0(x)|0\rangle \neq 0$ (non-zero vacuum expectation value):

$$V = m^2\Phi^\dagger\Phi + h(\Phi^\dagger\Phi)^2 \tag{2.21}$$

where $h \geq 0$ so that V is bounded from below (no negative infinite energy). There are two cases for m^2:

1. For case 1: $m^2 > 0$, the minimal vacuum corresponds to $\Phi = 0$ and $V = 0$.
2. For case 2: $m^2 < 0$, then minimum of V (so that $\partial V/\partial\Phi = 0$) corresponds to $|\Phi|^2 = -\frac{m^2}{2h}$ and $V_{min} = -\frac{m^4}{4h^2} < 0$. In this case, the ground state is not

$SU(2)_{\rm L} \times U(1)_{\rm Y}$ invariant. The Lagrangian $\mathcal{L}$ has the symmetries, which are not respected along the vacuum of the system, that is spontaneously breaking of the symmetries.

The following derivation will show how the gauge bosons obtain mass terms after spontaneous symmetry breaking. Consider the Higgs Lagrangian:

$$\mathcal{L}_H = \big[\Phi^\dagger(x)\big(\partial^\mu + ig\frac{\overrightarrow{\mathscr{T}}}{2}\overrightarrow{A}^\mu + ig'\frac{1}{2}B^\mu\big)\big]\big[\big(\partial_\mu - ig\frac{\overrightarrow{\mathscr{T}}}{2}\overrightarrow{A}_\mu - ig'\frac{1}{2}B_\mu\big)\Phi(x)\big] - V(\Phi^\dagger\Phi) \tag{2.22}$$

$\Phi(x)$ has four real independent components which break $SU(2)_{\rm L}\times U(1)_{\rm Y}$ (four generators) to $U(1)_{EM}$ (one generator), thus 3 gauge fields become massive (corresponding to the breaking vacuum state generators) and one remains massless (the generator which does not break the vacuum).

One can write:

$$\Phi(x) = e^{i\overrightarrow{\mathscr{T}}\overrightarrow{\theta}(x)}\begin{pmatrix} 0 \\ \dfrac{\lambda + H(x)}{\sqrt{2}} \end{pmatrix} \tag{2.23}$$

Under $SU(2)_{\rm L}$ transformation: $\overrightarrow{\theta} \xrightarrow{SU(2)_{\rm L}} \overrightarrow{\theta} + \frac{1}{2}g\overrightarrow{\omega}(x)$.

The Lagrangian:

$$\begin{aligned}\mathcal{L}_H \;=\; & \begin{pmatrix} 0 & \dfrac{\lambda + H(x)}{\sqrt{2}} \end{pmatrix}\left\{\partial^\mu + ig\left[\frac{1}{\sqrt{2}}\big(\mathscr{T}_+W^\mu + \mathscr{T}_-W^{\mu+}\big) + \frac{1}{2}\mathscr{T}_3A^{3\mu}\right] + ig'\frac{1}{2}B^\mu\right\}\times \\ & \left\{\partial_\mu - ig\left[\frac{1}{\sqrt{2}}\big(\mathscr{T}_+W_\mu + \mathscr{T}_-W^+_\mu\big) - \frac{1}{2}\mathscr{T}_3A^3_\mu\right] - ig'\frac{1}{2}B_\mu\right\}\begin{pmatrix} 0 \\ \dfrac{\lambda + H(x)}{\sqrt{2}} \end{pmatrix}\end{aligned} \tag{2.24}$$

Since we have:

$$\mathscr{T}_3^2 = \mathbb{1}_{2\times 2} \tag{2.25}$$

$$\mathscr{T}_+^2 = \mathscr{T}_-^2 = 0 \tag{2.26}$$

$$[\mathscr{T}_+, \mathscr{T}_3] = -2\mathscr{T}_+ \tag{2.27}$$

$$[\mathscr{T}_-, \mathscr{T}_3] = 2\mathscr{T}_- \tag{2.28}$$

$$[\mathscr{T}_+, \mathscr{T}_-] = \mathscr{T}_3 \tag{2.29}$$

so we are left with:

$$\text{Term with } \mathscr{T}_3\text{: } -\left(\frac{\lambda+H(x)}{\sqrt{2}}\right)^2\left[ig\frac{1}{2}A^{3\mu}\big(-ig'\frac{1}{2}B_\mu\big)+ig'\frac{1}{2}B^\mu(-ig\frac{1}{2}A^3_\mu)\right]$$

$$=-\frac{(\lambda+H(x))^2}{4}gg'A^{3\mu}B_\mu \tag{2.30}$$

$$\text{Term with } \mathscr{T}_3\mathscr{T}_3\text{: } \frac{(\lambda+H(x))^2}{8}g^2A^{3\mu}A^3_\mu \tag{2.31}$$

$$\text{Term with } \mathbb{1}\mathbb{1}\text{: } \frac{(\lambda+H(x))^2}{8}g'^2B_\mu B^\mu \tag{2.32}$$

$$\implies \text{Sum: } \frac{(\lambda+H(x))^2}{8}[g'B^\mu B_\mu-2gg'B^\mu A^3_\mu+g^2A^3_\mu A^{3\mu}]$$

$$=\frac{(\lambda+H(x))^2}{8}[(g'B^\mu-gA^3_\mu)(g'B_\mu-gA^{3\mu})] \tag{2.33}$$

$$\text{Term with } \mathscr{T}_+\mathscr{T}_- \text{ and } \mathscr{T}_-\mathscr{T}_+\text{: } \frac{(\lambda+H(x))^2}{4}g^2W_\mu W^{\dagger\mu} \tag{2.34}$$

$$\text{is the mass term for } W_\mu \implies M_W^2=\frac{1}{4}\lambda^2g^2 \tag{2.35}$$

$$\text{Denote } Z_\mu=\frac{gA^3_\mu-g'B_\mu}{\sqrt{g^2+g'^2}} \text{ then from term (2.33) } \implies M_Z^2=\frac{1}{4}\lambda^2(g^2+g'^2) \tag{2.36}$$

$$A_\mu=\frac{gA^3_\mu+g'B_\mu}{\sqrt{g^2+g'^2}}\implies M_A^2=0 \tag{2.37}$$

$$\text{While for Higgs field } M_H^2=-2m^2 \tag{2.38}$$

2.2.2 Yukawa interaction and Higgs coupling with bosons

Higgs coupling with weak gauge bosons

From equation 2.22, one can write the part concerning Higgs field and gauge fields:

$$\mathcal{L}_{HG} \;=\; \frac{g^2}{4}(\lambda+H)^2W^\dagger_\mu W^\mu+\frac{1}{4}(g^2+g'^2)(\lambda+H)^2Z^\mu Z_\mu \tag{2.39}$$

The ratio of the W boson's mass and the Z boson's mass (square at leading order) is:

$$\frac{M_W^2}{M_Z^2}=\frac{g^2}{g^2+g'^2}=\cos^2\theta_W \tag{2.40}$$

where θ_W is Weinberg angle. It goes beyond the scope of the thesis so no further discussion about it in this thesis.

From equation 2.39, one can write the interaction terms between Higgs and the gauge fields:

$$HWW: \qquad \frac{g^2}{4} 2\lambda H W_\mu^\dagger W^\mu = g M_W H W_\mu^\dagger W^\mu \tag{2.41}$$

$$HZZ: \qquad \frac{g^2+g'^2}{4} 2\lambda H Z^\mu Z_\mu = \sqrt{g^2+g'^2} M_Z H Z_\mu Z^\mu \tag{2.42}$$

One can see from equation 2.41 and 2.42 that the coupling of the Higgs boson to the weak gauge bosons are proportional to their masses.

Yukawa interaction

The Yukawa coupling from the SM Lagrangian in equation 2.1

$$\mathcal{L}_{\text{Yukawa}} = (y_d \bar{q}_L^\alpha \Phi d_{R\alpha} + y_u \bar{u}_L^\alpha \tilde{\Phi} u_{R\alpha} + y_e \bar{\ell}_L \Phi e_R + h.c.) \tag{2.43}$$

There are three generations of quarks and leptons in the SM, the weak charged current will mix three mass eigenstates of the quarks. However that story goes beyond the scope of this thesis so in this case to give a simple picture of Higgs coupling with fermions, only one generation is considered, as the following:

$$\mathcal{L}_{\text{Yukawa}} = (y_d \bar{q}_L \Phi d_R + y_u \bar{u}_L \tilde{\Phi} u_R + y_e \bar{\ell}_L \Phi e_R + h.c.) \tag{2.44}$$

Substitute

$$\Phi(x) = \begin{pmatrix} 0 \\ \dfrac{\lambda + H(x)}{\sqrt{2}} \end{pmatrix} \tag{2.45}$$

one has:

$$\begin{aligned} \mathcal{L}_{\text{Yukawa}} &= y_d \begin{pmatrix} \bar{u}_{\text{L}} & \bar{d}_{\text{L}} \end{pmatrix} \begin{pmatrix} 0 \\ \dfrac{\lambda + H(x)}{\sqrt{2}} \end{pmatrix} d_{\text{R}} + y_u \bar{u}_{\text{L}} i \begin{pmatrix} 0 & -i \\ i & 0 \end{pmatrix} \begin{pmatrix} 0 \\ \dfrac{\lambda + H(x)}{\sqrt{2}} \end{pmatrix} u_{\text{R}} + \\ &\quad + y_e \begin{pmatrix} \bar{\nu}_{e_{\text{L}}} & \bar{e}_{\text{L}} \end{pmatrix} \begin{pmatrix} 0 \\ \dfrac{\lambda + H(x)}{\sqrt{2}} \end{pmatrix} e_{\text{R}} + h.c \\ &= y_d \bar{d}_{\text{L}} \frac{\lambda + H(x)}{\sqrt{2}} d_{\text{R}} + y_u \bar{u}_{\text{L}} \frac{\lambda + H(x)}{\sqrt{2}} u_{\text{R}} + y_e \bar{e}_{\text{L}} \frac{\lambda + H(x)}{\sqrt{2}} e_{\text{R}} + h.c \end{aligned} \tag{2.46}$$

Combining with the Hermitian conjugate (h.c) terms, one obtain terms:

$$\begin{aligned} &\frac{\lambda}{\sqrt{2}} y_d (\bar{d}_{\text{L}} d_{\text{R}} + \bar{d}_{\text{R}} d_{\text{L}}) + \frac{\lambda}{\sqrt{2}} y_u (\bar{u}_{\text{L}} u_{\text{R}} + \bar{u}_{\text{R}} u_{\text{L}}) + \frac{\lambda}{\sqrt{2}} y_e (\bar{e}_{\text{L}} e_{\text{R}} + \bar{e}_{\text{R}} e_{\text{L}}) = \\ &= m_d (\bar{d} d) + m_u (\bar{u} u) + m_e (\bar{e} e) \end{aligned} \tag{2.47}$$

where $m_d = y_d\frac{\lambda}{\sqrt{2}}$, $m_u = y_u\frac{\lambda}{\sqrt{2}}$, $m_e = y_e\frac{\lambda}{\sqrt{2}}$ for down quark, up quark and lepton respectively (here u, d, e are representative for a generation of fermions) while neutrino doesn't gain any mass.

The interaction terms between the Higgs boson and the massive fermions are then:

$$Hf\bar{f} \quad : \quad y\frac{H(x)}{\sqrt{2}}f\bar{f} = g\frac{y\lambda/\sqrt{2}}{2g\lambda/2}Hf\bar{f} = \frac{g}{2}\frac{m_f}{M_W}Hf\bar{f} \tag{2.48}$$

From equation 2.48, the coupling of the Higgs boson with massive fermions is proportional to the fermions' masses.

What are presented in this Chapter is the simplified content of the SM, there are other aspects to be considered such as the charged weak currents mediated by W bosons which mix different quarks mass eigenstates causing the Cabibbo-Kobayashi-Maskawa (CKM) quark mixing matrix being responsible for CP violation; the neutral weak current mediated by Z boson, etc.

The fact that the Higgs coupling to particles is proportional to the particles' masses is important for the Higgs searches and the analysis presented in this thesis in determining which production channel and decay channel to look for the Higgs boson.

Chapter 3

CERN, the LHC and the ATLAS Detector

In this Chapter, a short introduction is given concerning the biggest particle physics laboratory in Europe: CERN (Section 3.1). Afterwards, the LHC and the ATLAS detector are described in Section 3.2 and 3.3. Prospects for the incoming new data taking and for the LHC future will be discussed in Chapter 8.

3.1 CERN

CERN is the European Organization for Nuclear Research founded in 1954 by 13 founding member states (with the acronym stands for the French "Conseil Européen pour la Recherche Nucléaire"). The CERN laboratory is located in the Franco-Swiss border near the city of Geneva. It was one of Europe's first joint ventures and now it counts 22 member states.

CERN hosts the construction, development and operation of a large range of particle accelerators together with all the necessary infrastructure for high energy physics research. Since its birth, many experiments have been constructed at CERN as a result of international collaborations and many searches have been successfully carried on, leading to discoveries as well as precise measurements.

Since 2008 till now, the biggest accelerator running at CERN is the LHC, which will be discussed in more detail in the next Section 3.2

3.2 The Large Hadron Collider

The Large Hadron Collider at CERN is the world biggest accelerator located in a circular tunnel 27 km in circumference. The tunnel is about 100 m underground in the countryside between Geneva, Switzerland and St. Genis, France. Sketches of the CERN accelerators complex and of the LHC are shown in Figures 3.1 and 3.2.

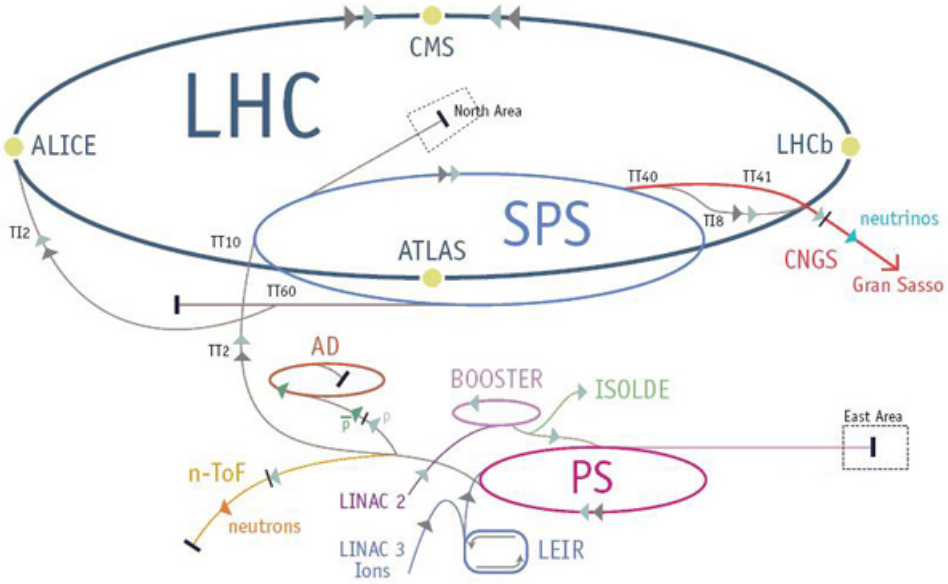

Figure 3.1: The CERN accelerators complex, including the LHC.[1]

Figure 3.2: A LHC sketch.[2]

The LHC has a design luminosity of 10^{34} $cm^{-2}s^{-1}$. It is built to collide two counter rotating beams of protons or heavy ions such as Lead ions. Proton-proton collisions are foreseen at an energy of 7 TeV per beam. The beams move around the LHC ring inside a continuous vacuum guided by magnets and accelerated by radio frequency cavities.

There are many theories have been developed so far to describe the fundamental blocks of matter and their interactions. There are also many experiments have been built for discovering new particles and checking those theories. The 80-90 decades

[2]Figure own by http://public.web.cern.ch/public/en/research/AccelComplex-en.html

showed us that most discoveries [36–39] [3] in the field of high energy physics occurred at hadron colliders. Moreover, the higher the centre-of-mass energy the colliding beams reach, the smaller is the mass scale which can be explored. The LHC can nowadays produce the highest centre-of-mass energy of 13 TeV ever reached and therefore will hopefully help to perform other discoveries besides the discovery of the Higgs boson, the last unidentified particle of the SM found by ATLAS and CMS experiment in July, 2012.

To accelerate a proton beam at the energy reached by the LHC one needs a chain of accelerators (see Figure 3.1). Protons are first created by bleaching electrons out of hydrogen atoms using an electric field. The protons are then accelerated to 50 MeV by the Linac II accelerator. The beam is then injected into the Proton Synchrotron (PS) Booster to be accelerated to 1.4 GeV and next to the PS where it reaches the energy of 25 GeV. As a last step before being injected into the LHC beam pipes, protons are accelerated to 450 GeV by the Super Proton Synchrotron (SPS) and then sent to the LHC, where they acquire final energy.

Inside LHC, two beams of particles (protons or heavy ions) at a speed close to the speed of light with very high energies travel in opposite directions before colliding with each other. They are guided around the accelerator rings by a strong magnetic field of 8 Tesla produced by 1232 15m-length superconducting dipole magnets. To bring the magnet to the superconducting state, a temperature of $-271^0\ C$ is required, so most of the accelerator is connected to a distribution system of liquid helium, which cools the magnets. Besides the dipoles, there are additional magnets of different varieties and sizes, like 392 quadrupole magnets, each 5-7 m long, to focus the beam. Just prior to collision, another type of magnet is used to "squeeze" the particles closer together to provide collisions

All the controls for the accelerator, its services and technical infrastructure are coordinated by the CERN Control Centre. From here, the beams inside the LHC are made to collide at four locations around the accelerator rings, corresponding to the positions of the first four particle detectors listed below. LHC hosts six experiments:

- ALICE: A Large Ion Collider Experiment.
- ATLAS: A large Toroidal LHC ApparatuS.
- CMS: The Compact Muon Solenoid.
- LHCb: Large Hadron Collider beauty experiment.
- TOTEM: Total Cross Section, Elastic Scattering and Diffraction Dissociation at the LHC.
- LHCf: Large Hadron Collider forward.

[3] We refer here to the W [36,37] and Z [38] boson discovery at the UA1 experiment (also at the UA2 for W-boson) (CERN) in 1983 and the top-quark [39] at Fermilab in 1995.

ALICE, ATLAS, CMS, LHCb are the four main experiments at the LHC. ATLAS and CMS are for general purpose of physics searches and measurements. ALICE is designed to study the physics of strongly interacting matter at extreme energy densities. LHCb is specialized in investigating the matter-antimatter asymmetry by studying physics processes involving b-quarks.

Collisions were produced at an interval of 50 ns and reached 25 ns in August this year. Run I with the first collisions at an energy of 3.5 TeV per beam started on March 30^{th}, 2010. A beam energy of 4 TeV was reached on April 4^{th}, 2012. Proton-Lead ion collisions started on January 20^{th} and then Run I stopped on Feb 11^{th}, 2013. Run II with stable beams at centre-of-mass energy of 13 TeV just began on June 3^{rd}, 2015. The accelerator has a long term schedule with possible upgrades in the future.

3.3 The ATLAS Detector

The ATLAS detector [42], centred on one of the LHC collision points, is designed to identify the particles produced in collisions, measure their energies and momenta, and make fast decisions about the content of each collision. It is 46 meters long, 25 meters high and weighs about 7,000 tonnes. To cover hermetic geometry and provide a sensitivity for as much as possible physical processes, structure, consisting of four sub-detectors are disposed in concentric cylinders with the axes along the beam pipe as shown in Figure 3.4. Each sub-detector is composed by a central part (barrel) and by two forward (end-cap) parts.

The ATLAS experiment uses the following coordinate system (see Figure 3.3):

- z-axis: coincides with the beam direction while the x-y plane is the transverse plane.
- The positive x-axis direction goes from the interaction point to the centre of the LHC ring, while the positive y-axis is pointing upwards. The azimuthal angle ϕ is measured around the beam axis, the polar angle θ is the angle from the beam axis. The rapidity is defined as $y = \frac{1}{2} \ln \frac{E+p_z}{E-p_z}$ where E and p_z are the energy and z-component of an object's momentum. In the relativistic limit, rapidity can be approximated by the pseudo-rapidity defined as $\eta = -\ln \tan(\frac{\theta}{2})$. Both differences in y or η are invariant under Lorentz transformations so that their use turns out to be very convenient.
- The transverse momentum p_{T} and the transverse energy E_{T}, as well as the missing transverse momentum $E_{\mathrm{T}}^{\mathrm{miss}}$ and other transverse variables, are defined as the variables' component in the x-y plane.
- The distance ΔR in the pseudo-rapidity-azimuthal angle space is defined as $\Delta R = \sqrt{(\Delta\eta)^2 + (\Delta\phi)^2}$.

Details of the structure and function of the different parts of the ATLAS detector are given in the following: Section 3.3.1 for Magnet System, Section 3.3.2 for Inner Detector (ID), Section 3.3.3 for Calorimeters, Section 3.3.4 for Muon Spectrometer. One hardware system for supporting data taking readout is also discussed here, the trigger system describe in Section 3.3.5.

3.3.1 Magnet Systems

The ATLAS detector includes two magnet systems. Their layout is shown in Figure 3.5.

A central solenoid (CS) is placed in between the ID and calorimeters. The CS provides a central magnetic field of 2 T with a peak value of 2.6 T at the superconductor itself within the ID (see Section 3.3.2). That magnetic field is oriented with

[4]The pseudo-rapidity distribution is taken from https://en.wikipedia.org/wiki/Pseudorapidity.

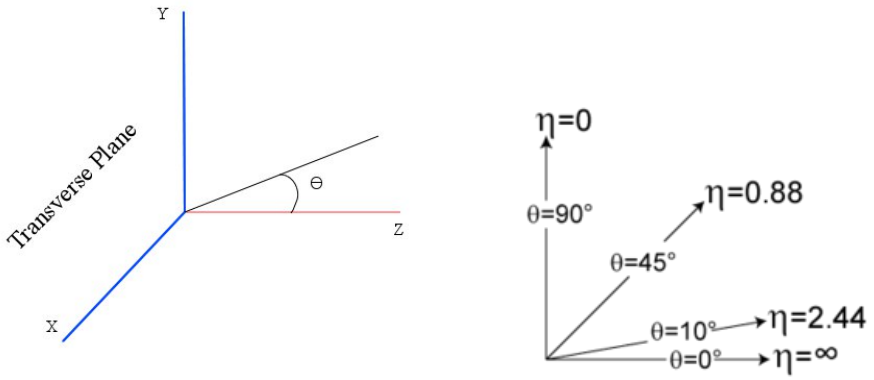

Figure 3.3: Detector coordinates (left) and pseudo-rapidity distribution [4](right).

the beam axis so that when positively charged particles pass perpendicular to the field, they are bent in the negative ϕ direction. From the curves of the tracks left in the ID caused by the magnetic field, the momentum and charges of the particles can be determined.

At the outer section of the detector there is a system of three large air-core toroids generating the intense magnetic field thanks to a current flowing through 80 km of conduction cable for the Muon Spectrometer. The two end-cap toroids (ECT) are inserted in the barrel toroid (BT) at each end and line up with the central solenoid. The peak magnetic fields on the superconductors in the BT and ECT are 3.9 and 4.1 T respectively, in the ϕ direction so that muons are bent in θ direction when passing by the Muon Spectrometer. The toroid magnets helps to bend the muons' tracks as much as possible to measure their 4-momenta.

3.3.2 Inner Detector

It is the closest detector to the beam pipe, has 2.1 m in diameter and 6.2 m in length. It is made of three sub-detectors: Pixel Detector, Semiconductor Tracker (SCT), Transition Radiation Tracker (TRT), described in more details below. During the long shut down in 2013-2014, an additional layer of the Pixel Detector called Insertable B-Layer (IBL) was installed as the innermost layer. ID's main function is measuring trajectories of charged particles which pass through it and are bent by the axial magnetic field of 2 Tesla generated by the CS. The coverage region of ID is $|\eta| < 2.5$. Its layout is shown in Figure 3.6.

Pixel detector

It is the innermost part of the ID. It consists of three barrels (at radii 50.5 mm, 88.5 mm and 122.5 mm) and three disks on each side of the detector (placed at

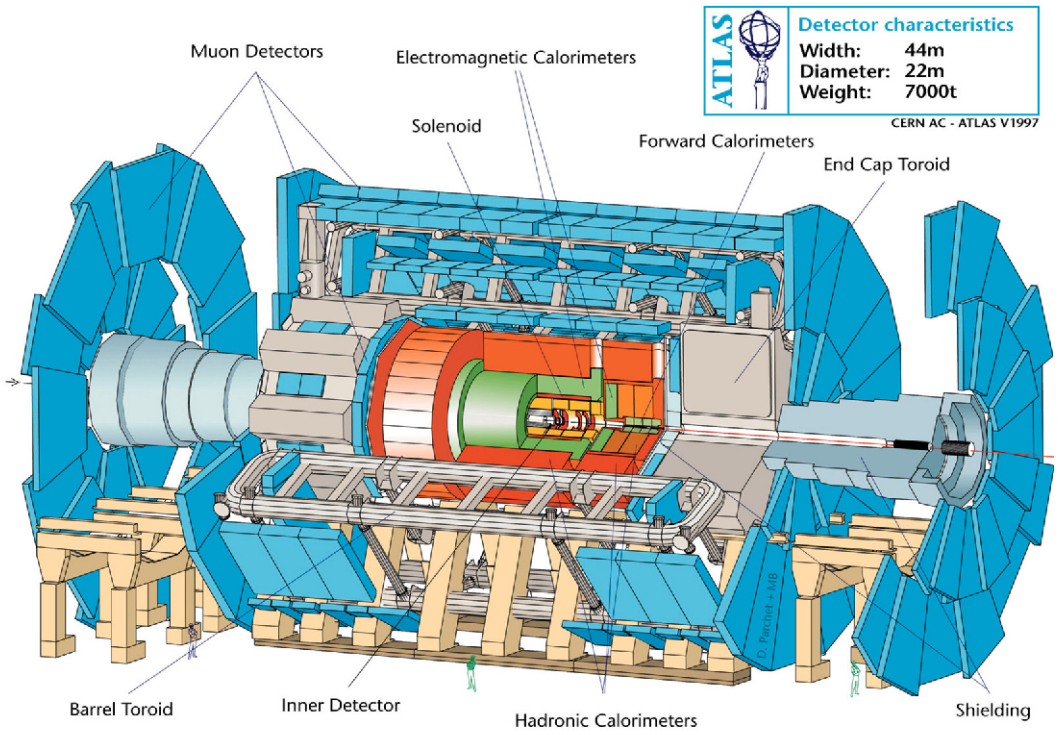

Figure 3.4: ATLAS layout.

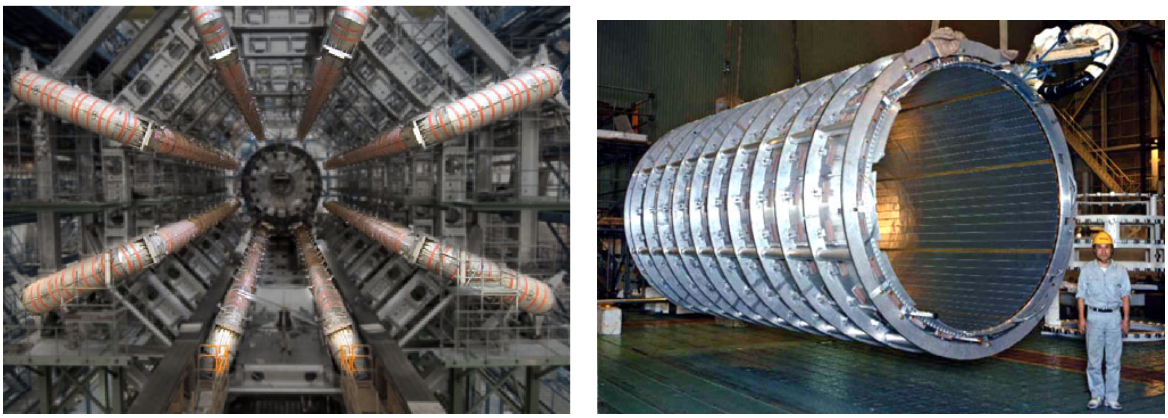

Figure 3.5: Magnet system layout: the toroid magnets (left) and the central solenoid (right).

495 mm, 580 mm and 650 mm from the detector centre). Those layers are made of a large amount of pixel modules. It provides three precision measurements of momentum, vertex and impact parameter [5], allows to measure secondary vertices

[5]Impact parameter is defined as the distance to the beam axis at the point of closest approach, signed according to the reconstructed angular momentum of the track about the axis.

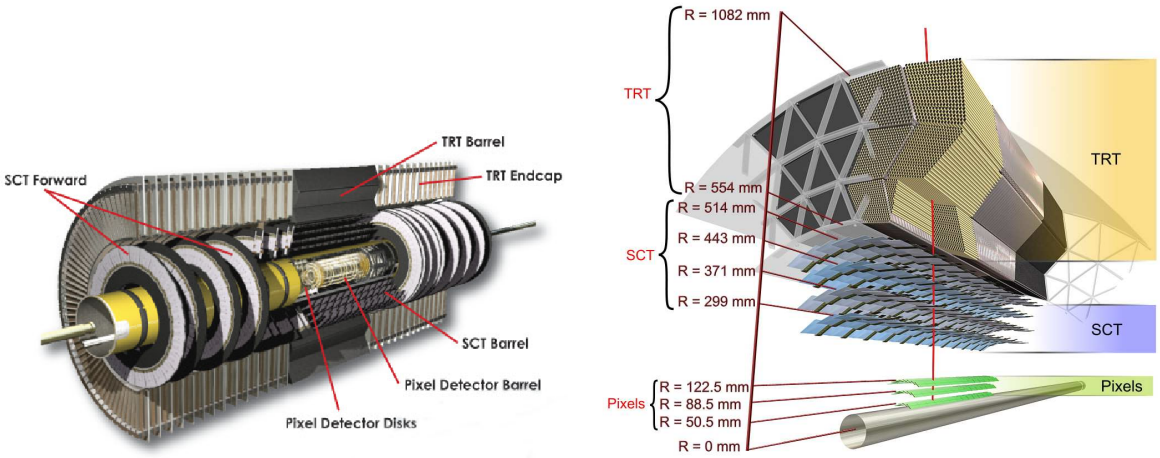

Figure 3.6: Inner Detector layout.

and plays an important role in finding short-lived particles such as B-hadrons and tau-leptons.

Semiconductor Tracker (SCT)

It is located in the middle of the ID. In the barrel it consists of eight layers (with radii between 299 mm and 514 mm and a full length of 1492 mm) of stereo Silicon microstrip detectors at an angle of 40 mrad while in the end-caps it has nine set of strips running radially on each side. Each strip has four singlesided p-on-n silicon detectors.

SCT gives eight precision measurements per track in the intermediate radial range, providing good pattern recognition.

The pixel module and the microstrip have the same working principle. Each of them consists of a thin top layer of Silicon connected to a lower layer of electronic through a larger range of spheres. When a charged particle passes through it, electrons are liberated and then move to the bottom of the strip making the electric current through one or more spheres. By seeing which sphere has the signal, one can convert it into binary numbers to store and analyse.

Transition radiation tracker (TRT)

It's located in the outermost layer of the ID (with the radii ranges from 563 mm to 1066 mm) and contains a huge number of straw tubes parallel to the beam pipe while all the end-cap tracking elements are perpendicular to the beam axis. Each straw is 4 mm in diameter and equipped with a 30 μm diameter Gold-plated Tungsten Rhenium (W-Re) wire providing a drift-time measurement. If a charged particle passes through the material (a Xe-based gas mixture in the straw tubes), it

will create transition-radiation photons. Those photons excite more electrons, those go to the wire inside the tube and create electric signals. The system creates two thresholds, one is tracking hit with lower threshold and one is transition radiation hit with higher threshold. Hence, the TRT gives good pattern recognition performance such as distinguishing between electrons and hadrons.

Summary of the resolution as well as some other characteristics of the ID sub-detectors is shown in Table 3.1

Sub-detector	Radius[cm]	Element size	Spatial resolution[μm]	Hits per track
Pixel	5 - 12	50 μm $\times$ 400 μm	10 (R-ϕ) $\times$ 115 (z)	3
SCT	30 - 52	80 μm	17 (R-ϕ) $\times$ 580 (z)	8
TRT	56 - 107	4 mm	130	30

Table 3.1: Summary of different ID sub-detectors, technical designs and expected performance.

3.3.3 Calorimeters

They occupy the second and third compartments of the ATLAS detector, placed next to the ID and CS. There are two sections: the Electromagnetic Calorimeter (EMCAL) and Hadronic Calorimeter (HCAL) which will be described in more details below. They provide measurements of the particles' energy, especially electrons and photons, which pass through and interact with absorber material. Their layout is shown in Figure 3.7.

Electromagnetic Calorimeter

It covers the pseudo-rapidity region $|\eta| < 3.2$. It is placed close to the CS and is a high granularity liquid-Argon (LAr) electromagnetic (EM) sampling calorimeter using lead plates as the absorber. The liquid Argon is cooled to -185 ^{0}C. The layout of the EM CAL is shown in Figure 3.8.

When electrons go into the absorber, they interact with the material and produce showers of low energy electrons, positrons and photons. The high energy electrons will travel through several layers of absorber and create a large shower before eventually stop. The shower of low energy particles pass into the liquid Argon and ionizes atoms, creating more negative charged electrons and positive charged ions. The negative charged ones are attracted toward the copper electrode where they are measured. From the amount of positive charges on each electrode along its path, one can measure the energy deposited by the original electron or photon when it enters the EMCAL.

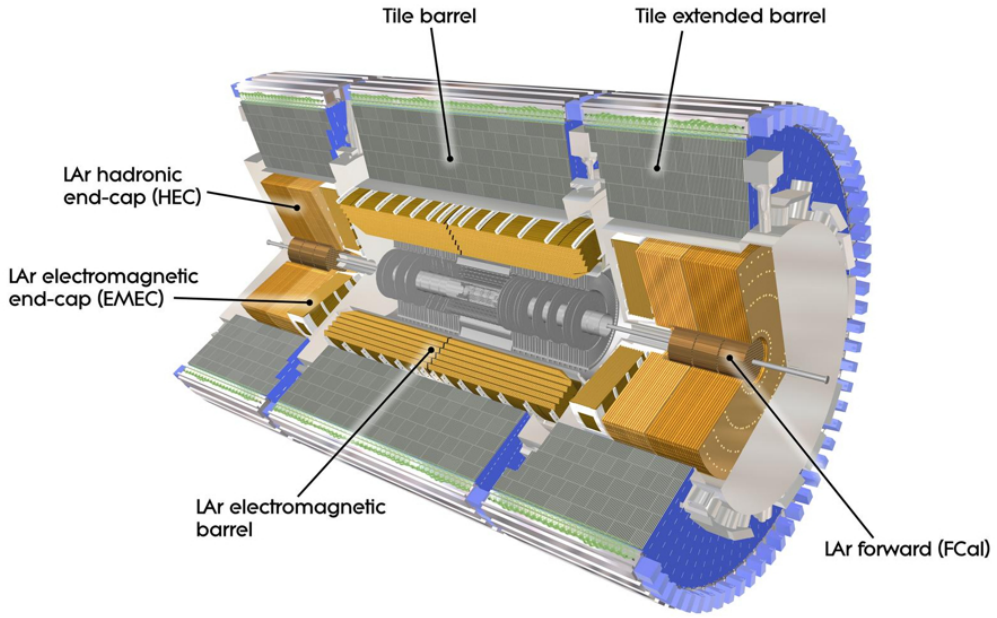

Figure 3.7: Calorimeters layout.

Hadronic Calorimeters

It is the second section of the Calorimeters, close to the Muon Spectrometer. HCAL covers the region $|\eta| < 4.9$ with different calorimeters. In the region $|\eta| < 1.7$ it uses iron scintillating-tile technique. In the region $1.5 < |\eta| < 4.9$ it uses LAr calorimeters with the Hadronic End-cap calorimeter (HEC) covering $|\eta| < 3.2$ and the high density forward calorimeter (FCAL) covering $3.1 < |\eta| < 4.9$.

HCAL provides good containment for hadronic showers and reduces punch-through into the muon system. It provides a good missing transverse momentum measurement, which is very important for many physics signatures. It measures energies of hadrons such as protons, neutrons, mesons via a large range of interleaved steel with layers of scintillators ("tiles") which emit lights when crossed by particles. When a high energy hadron passes through the steel, it will interact with atoms' nuclei. The nuclear interaction will create more particles which initiate further interactions and create showers. The showers of particles, which are produced, enter the scintillator cause light emission. Long fibers then carries the light to devices where the light intensity measured and converted into electric current. Using the intensity of light, the energy possessed by the high energy hadron which enters the HCAL can be measured.

The energy resolution and pseudo-rapidity coverage for the calorimeter system

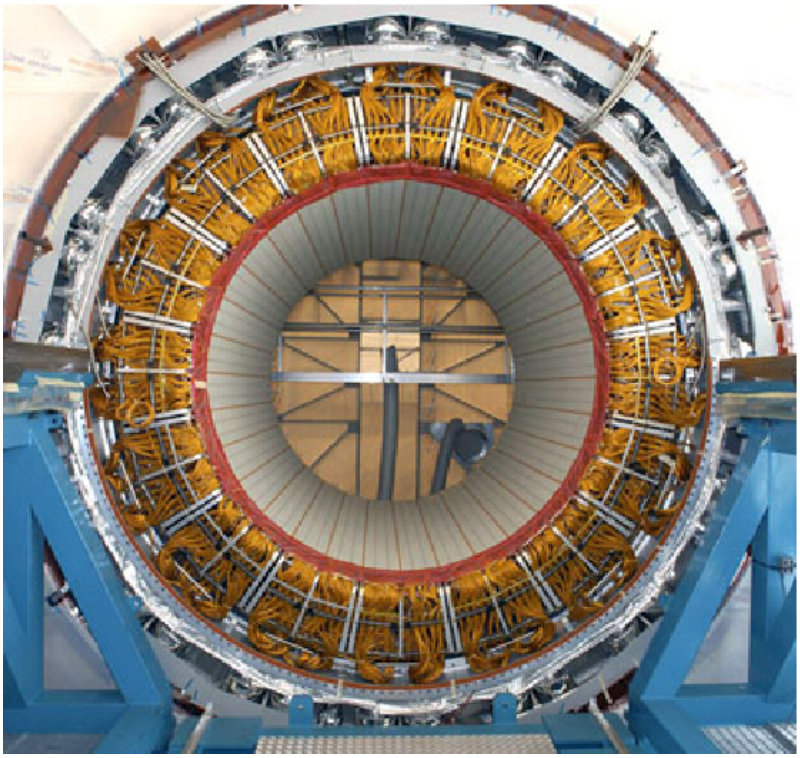

Figure 3.8: Electromagnetic calorimeter layout.

is summarized in Table 3.3.3.

Detector component	Energy resolution (σ_E/E)	$\|\eta\|$ coverage
EM calorimetry	$10\%/\sqrt{E} \oplus 0.7\%$	< 3.2 (< 2.5 for the trigger)
Hadronic calorimetry Barrel & End-Cap	$50\%/\sqrt{E} \oplus 3\%$	<3.2
Forward	$100\%/\sqrt{E} \oplus 3.1\%$	$\in [3.2, 4.9]$

Table 3.2: Nominal detector performance goals and coverage for the ATLAS calorimetric system

3.3.4 Muon Spectrometer

The Muon Chamber layout is shown in Figure 3.9. The Muon Spectrometer, which measure the trajectories of muons, is located outside and embraces all of the Calorimeters. It consists of Monitored drift-tube chambers, Cathode strip chambers, Resistive plate chambers and Thin gap chambers. Over the range of $|\eta| \leqslant 1.0$

a magnetic field is provided by the large barrel toroid already mentioned in Section 3.3.1. In the region $1.4 \leqslant |\eta| \leqslant 2.7$, muon tracks are bent by the two end-cap magnets inserted into both ends of the barrel toroid. Over the range $1.0 \leqslant |\eta| \leqslant 1.4$, or the transition region, magnetic deflection is provided by a combination of barrel and end-cap toroids so that the magnetic field is perpendicular to the muon trajectories.

As an example of how a muon chamber works, one segment of the Monitored drift-tube chamber contains many small tubes filled with gas. When a muon passes through these tubes, it leaves a trail of electric charge of ions and electrons which then drift to the side and centre of the tube. One can identify the drifting starting point of the drifting in each tube. By measuring the time attached for these charges to drift from the starting point, the muon position can be determined.

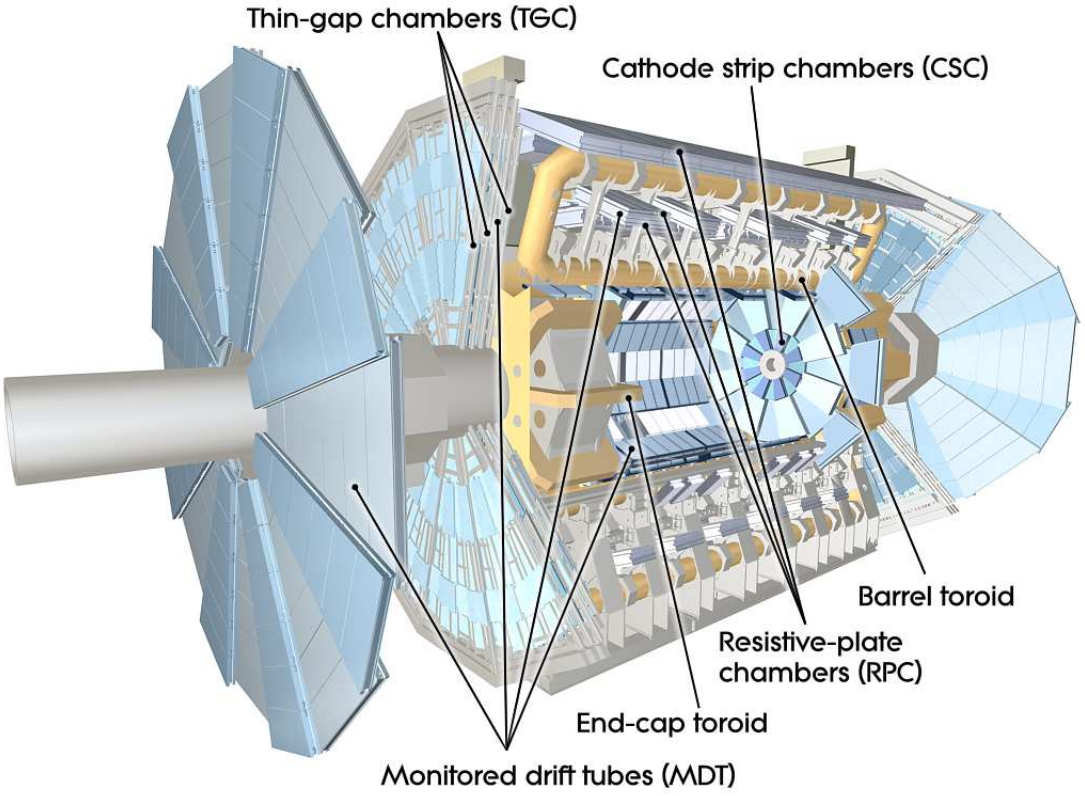

Figure 3.9: Sketch of the Muon Chamber layout.

The transverse momentum resolution:

$$\frac{\sigma_{p_{\mathrm{T}}}}{p_{\mathrm{T}}} = \frac{0.29 \text{ GeV}}{p_{\mathrm{T}}} \oplus 0.043 \oplus 4.1 \times 10^{-4} \text{ GeV}^{-1} \times p_{\mathrm{T}}$$

for p_{T} between 5 and 400 GeV.

3.3.5 Trigger system

The LHC is designed to have a very high instantaneous luminosity of $10^{34} cm^{-2} s^{-1}$ so that each second a huge amount of raw data are produced by the collisions. Besides the fact that there are not enough resources to store those data (saving the full data stream would require a space for 40 TB of raw data per second), most of them are not interesting to be analysed. Therefore, the ATLAS trigger system is designed to filter the events produced by the LHC and reduce the enormous rate of 20 MHz to a much more manageable of 400 Hz, to be stored for offline analyses. This is achieved through a three levels sequential process consisting of a Level 1 (L1) hardware trigger and a software based High Level Trigger (HLT), which is itself divided into a Level 2 (L2) and Event Filter (EF). The analysis presented in this analysis uses an $E_{\mathrm{T}}^{\mathrm{miss}}$ trigger to select events which have high missing transverse momentum. Because of further corrections made in the offline reconstructed $E_{\mathrm{T}}^{\mathrm{miss}}$ and the resolutions of the L1 and L2 calculations, this trigger is not fully efficient until the offline $E_{\mathrm{T}}^{\mathrm{miss}}$ is greater than 150 GeV.

Besides the ones described above, there are detector chambers placed in the forward region to measure particles produced at small angle to the proton beams.

Chapter 4

Standard Model Processes at the LHC

For physics analyses at the LHC, one wants to extract the relevant signals which can be SM or beyond SM processes. In either case, it is very important to determine precisely different possible electroweak and QCD contributions either as signal or background. As discussed in Section 3.2, the LHC is a hadron collider using protons and heavy ions as rotating beams so QCD contribution is very huge. This chapter mainly discusses about QCD at the LHC in Section 4.1, the Higgs production modes and decay channels as well as its discovery and probe of Higgs invisible decay in Section 4.2.

4.1 QCD at the LHC

4.1.1 Parton Distribution Function

Proton is a composite particle. It contains valence quarks including two up quarks and one down quark, sea quarks including $u, \bar{u}$, $d, \bar{d}$, $c, \bar{c}$, $s, \bar{s}$, $b, \bar{b}$ and gluons.

We can understand proton collisions in term of the constituent quarks and gluons. Each proton has energy 4 TeV (for the centre-of-mass energy 8 TeV), but quarks and gluons inside the proton don't have that much energy. They can just carry a fraction of momentum from the proton with a certain probability which is determined by the parton distribution functions (or parton density functions-PDFs). Shown in the diagram in Figure 4.1 are the PDFs for partons in a proton.

Some particular properties of the PDFs of a proton's constituents and anti-

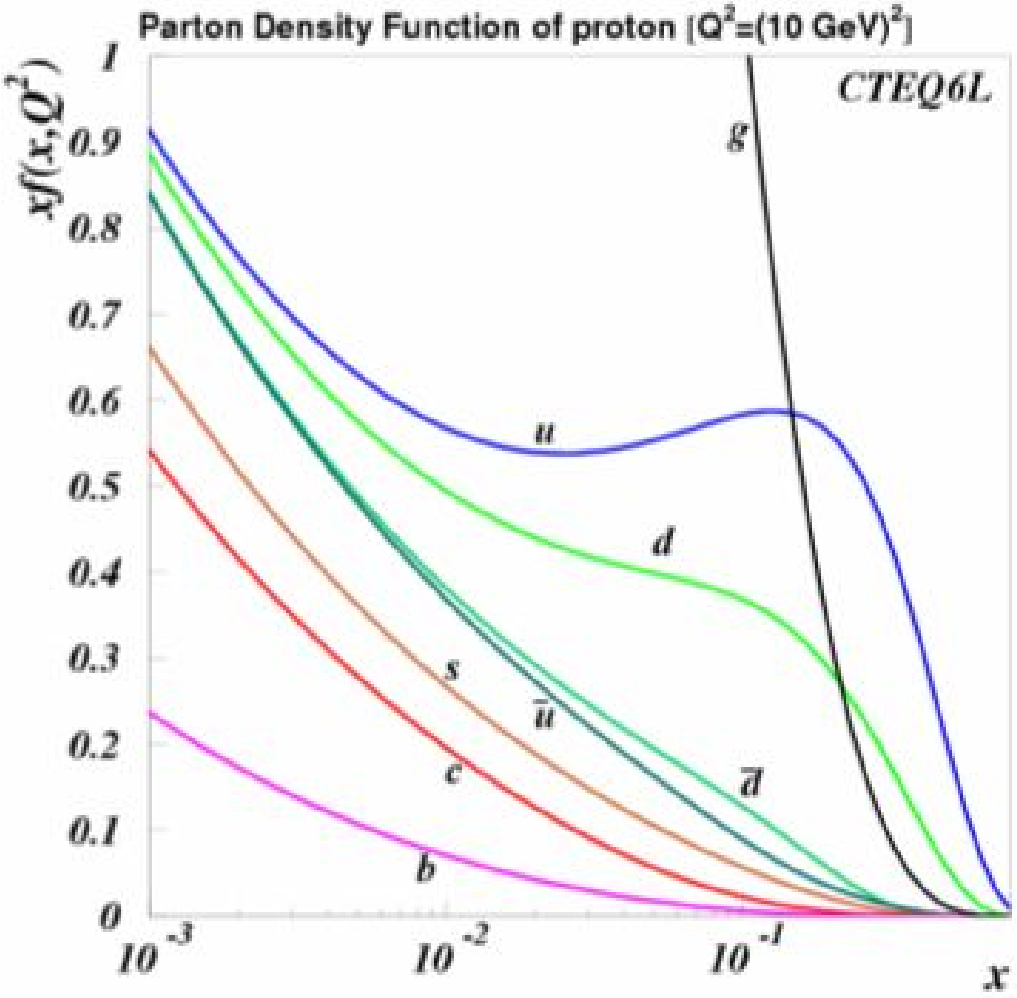

Figure 4.1: Parton distribution functions of gluons and quarks in a proton. x is fraction of momentum of a quark (or gluon) inside a proton. $0 < x < 1$, and $f_i(x)$ is the PDFs of parton i^{th}.

proton's:

$$\int_0^1 x dx \sum_{i=q,g} f_i(x) = 1, \tag{4.1}$$

$$\int_0^1 dx[f_{s/p}(x) - f_{\bar{s}/p}(x)] = 0, \tag{4.2}$$

$$\langle N_u \rangle = \int_0^1 dx[f_{u/p}(x) - f_{\bar{u}/p}(x)] = 2, \langle N_d \rangle = \int_0^1 dx[f_{d/p}(x) - f_{\bar{d}/p}(x)] = 1, \tag{4.3}$$

$$f_q^{\bar{p}}(x) = f_{\bar{q}}^p(x) \tag{4.4}$$

where x is the fraction of momentum of a quark (or a gluon) inside a proton. $0 < x < 1$, $f_i^p(x)$ is the PDF of parton i^{th} inside proton, $f_i^{\bar{p}}(x)$ is the PDF of parton i^{th} inside anti proton. $\langle N_u \rangle, \langle N_d \rangle$ are the expectation values for the number of u-quark and d-quark in a proton. From Figure 4.1, one sees that the different parton densities have very different behaviour, for the valence quarks (uud) they peak somewhere around $x = \frac{1}{3}$, while for gluons PDF is small at x ~ 1 and grows very rapidly towards small x. For some typical part of the relevant parameter space ($x = 10^{-3}, ..., 10^{-1}$) it roughly scales like $f_g(x) \sim x^2$. Towards smaller x values it becomes even steeper. This steep gluon distribution was initially not expected and means that for small enough x LHC processes will be dominant by gluon fusion processes.

4.1.2 Cross sections of SM processes at the LHC

To calculate the cross section of a specific process at the LHC, we have to involve the PDFs using the general formula as the following:

$$\sigma_{tot} = \int_0^1 dx_1 \int_0^1 dx_2 \sum_{ij} f_i(x_1) f_j(x_2) \hat{\sigma}_{ij}(x_1 x_2 s) \tag{4.5}$$

Where i, j are the incoming partons with the momentum fractions x_i, x_j . The partonic energy of the scattering process is $\hat{s} = x_1 x_2 s$ with the LHC centre-of-mass energy of $\sqrt{s} = 8$ TeV for the search discussed in this thesis. $\hat{\sigma}_{ij}$ corresponds to the partonic cross section and σ_{tot} is the total cross section with proton-proton initial state.

Considering two cases: first, the process $q\bar{q} \to q'\bar{q}'$; second, the process $gg \to q'\bar{q}'$ (see Feynman diagrams in Figure 4.2) in the limit of q' as light quarks. At the LHC, massless fermions are a good approximation except for the top-quark while the bottom-quark's mass is important for some situations.

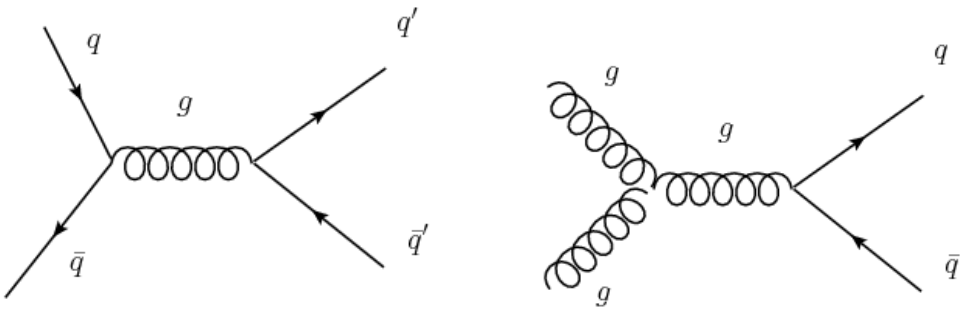

Figure 4.2: Feynman diagrams of the $q\bar{q}$ production at the LHC with quarks initial states (left) and gluons initial states (right).

The following rough estimates are from the Particle Data Group (PDG) [43], shown as a demonstration for the PDFs. The differential cross sections of light quark pairs are as the following:

$$\frac{d\hat{\sigma}_1}{d\Omega}(q\bar{q} \to q'\bar{q}') = \frac{\alpha_s^2}{9s}\frac{s^2+u^2}{t^2} \tag{4.6}$$

$$\frac{d\hat{\sigma}_2}{d\Omega}(gg \to q'\bar{q}') = \frac{\alpha_s^2}{24s}(t^2+u^2)\left(\frac{1}{tu} - \frac{9}{4s^2}\right) \tag{4.7}$$

In which, we have some relations for the Mandelstam variables:

$$s = (p_1+p_2)^2 \tag{4.8}$$

$$t = -s\frac{1+\cos\theta}{2} \tag{4.9}$$

$$u = -s\frac{1-\cos\theta}{2} \tag{4.10}$$

where p_1, p_2 are 4-momentum of the incoming particles. Without any calculation, one sees the resulting partonic cross sections are inversely proportional to the centre-of-mass energy meaning that the partonic cross sections will decrease with the energy level they reach to. However, due to the PDFs, as in Figure 4.3 from Ref. [44] , at the LHC the $\sigma(pp \to b\bar{b})$ increases with the centre-of-mass enegery and $\sim 10^5 nb$ at $\sqrt{s} = 14$ TeV; and the cross sections of quarks processes are very small comparing with cross sections of gluon fusion processes.

Figure 4.3 (from Ref. [44]) shows that at the LHC the production cross section for a pair of bottom quarks is larger than 10^5 nb thus to be the dominant process. It creates such a huge background for many processes, such as for Higgs signal $H \to b\bar{b}$. There are other important processes, which are dominant backgrounds for Higgs searches at the LHC, such as W, Z boson, top-quark involving processes.

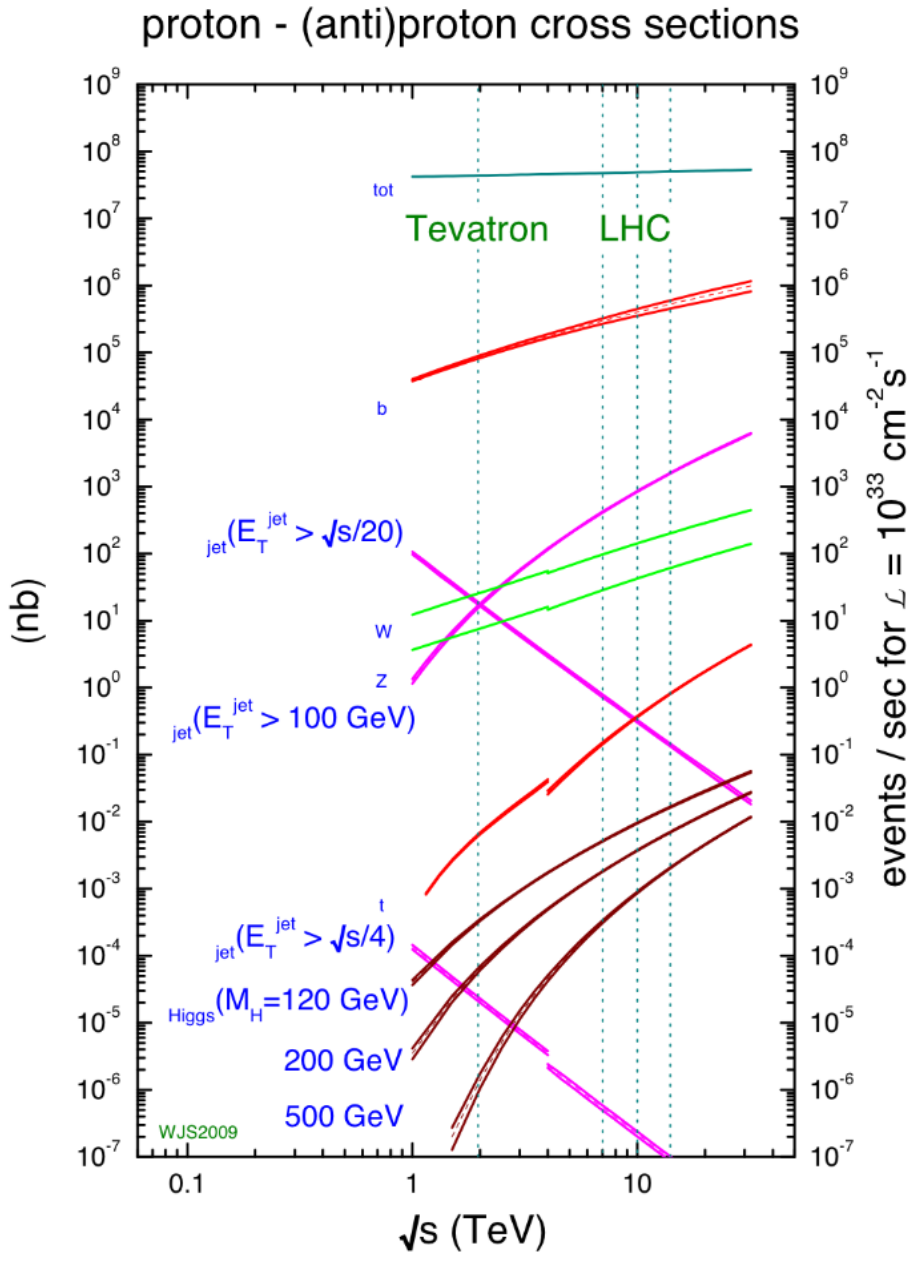

Figure 4.3: Production rates for different processes at hadron colliders. The discontinuity is due to the Tevatron being a proton-antiproton collider while the LHC is a proton-proton collider. The two colliders centre-of-mass energy corresponds to the x-axis values of 2 TeV and between 7 TeV and 14 TeV.

4.2 Processes with Higgs boson at the LHC

In the SM, the Higgs couplings to gauge bosons and fermions are proportional to the masses of the particles so the Higgs boson tends to decay into the heaviest ones allowed by phase space. Higgs boson can just be detected through its decay products. The Higgs decay and production processes have large backgrounds from W, Z, top-quark, light hadron and especially QCD involving processes. Therefore, at the LHC, the reconstruction of those backgrounds are very important for the Higgs searches. Higgs productions and decay channels will be discussed in Section 4.2.1 and 4.2.2 respectively following the study presented in Ref. [45].

4.2.1 The Higgs production at the LHC

As mentioned above, in the SM the Higgs boson couples preferentially to the heavy particles which are the W boson, Z boson, top-quark and at a much lower strength with the bottom-quark. Thus, the four main production processes for Higgs particles at the LHC are: the associated production with W/Z bosons, the weak vector boson fusion processes, the gluon-gluon fusion mechanisms and the associated Higgs production with top quarks. The distributions of the cross sections from different production modes as a function of the Higgs's mass is shown in Figure 4.4 from Ref. [46].

The gluon-gluon fusion mechanisms

At leading order the Higgs boson productions via the gluon-gluon fusion processes are from heavy quarks' (top-quark or in a lesser extent the bottom-quark) triangle loops. This is the dominant contribution to the Higgs production cross section at the LHC. See Feyman diagram (a) in Figure 4.5.

The vector boson fusion processes

In the vector boson fusion production channel, the SM Higgs boson is produced in association with two hard jets in the forward and backward regions of the detector in contrast to other jet production mechanisms. This provides the second dominant cross section for Higgs production at the LHC and is the main process relevant for this thesis, thus the kinematics of the process will be discussed in detail as below.

This channel is a three-body production process where the Higgs boson couples to weak vector bosons which connect two quark lines, and it is dominated by t- and u-channel-like diagrams thus represents a genuine VBF channel. Its kinematics is rather involved but plays an essential role to discriminate the signal from the large QCD backgrounds. The intermediate weak vector bosons tend to carry a small fraction of the initial quarks' energies while they must have an energy of $\mathcal{O}(\frac{1}{2}M_H)$ to produce the Higgs boson. Thus, the resulting two quarks must carry a big fraction of the must-be high-energy initial two quarks, as a consequent their energies are of

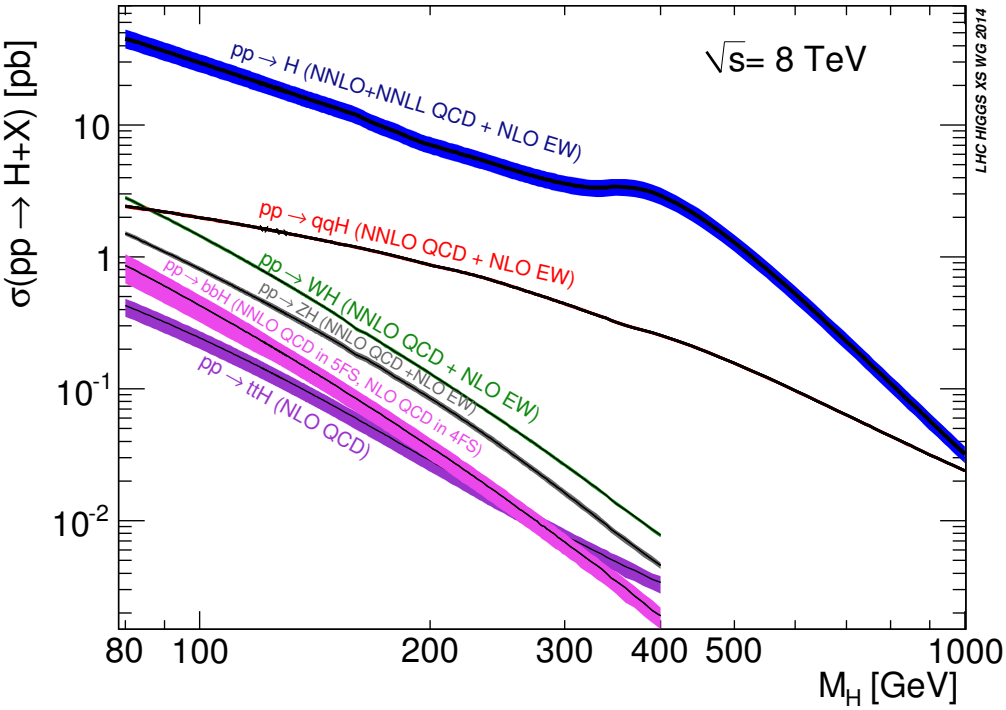

Figure 4.4: The production cross section of the SM Higgs boson as a function of the Higgs' mass at the LHC.

the order 1 TeV at the LHC. On the other hand, their transverse momenta are set by the vector boson propagators so $p_{\mathrm{T}} \sim M_V$, which are small comparing with the large energies they obtained. Since $p_{\mathrm{T}} = |\overrightarrow{p}| \sin\theta$, so the relatively small transverse momenta and high energies of the final state quarks correspond to rather small scattering angle θ, in term of pseudo-rapidity for each jet it would be $1 \lesssim \eta \lesssim 5$ (see Figure 3.3 for pseudo-rapidity distribution). The two jets are produced in opposite hemispheres so the product of their pseudo-rapidities is negative. Moreover, the two forward jets tend to be very well separated in pseudo-rapidity, so we can require a large pseudo-rapidity gap between the two forward jets ($\gtrsim 4.4$). The requirements up to now form the basic ingredients to isolate the VBF signal at the LHC from the various QCD backgrounds.

The decay products of the Higgs boson must have a substantial p_{T} and they must be well separated from the final state jets mentioned above, thus should be observable. Higgs production occurs in the central region so its decay products also tend to be central (pseudo-rapidity less than 1), this is different from the QCD background which gives a higher rapidity for the same final states.

There is a difference in the amount of jets in the central region between Higgs signal and QCD backgrounds. When taking into account the QCD corrections (soft emitting gluons), the VBF process proceeds without colour exchange between the scattered quarks, and gluons will be preferentially emitted at rather small angles in

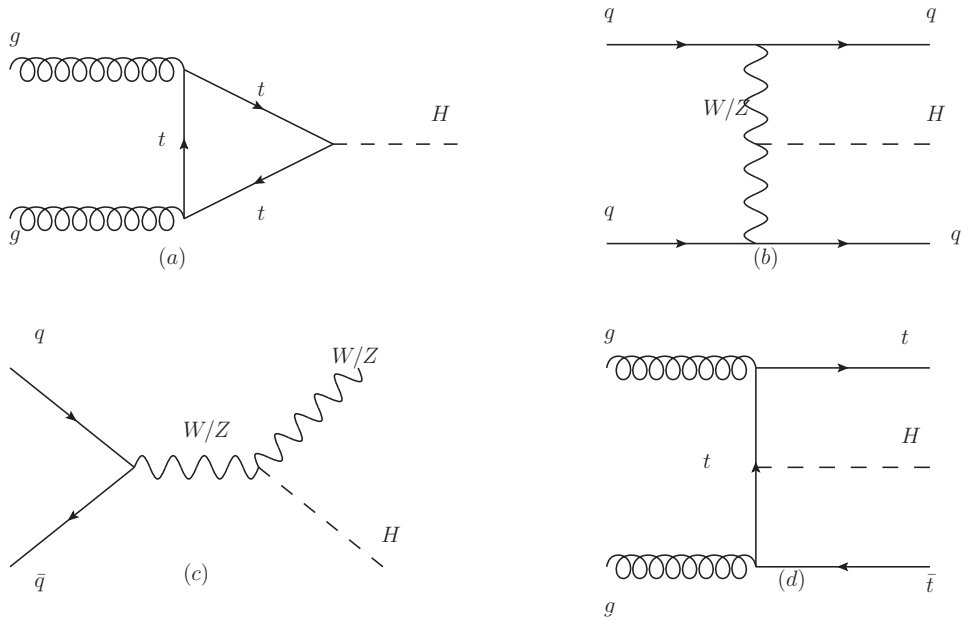

Figure 4.5: Feyman diagrams at leading order for four main production processes of Higgs particles at the LHC: (a) gluon fusion, (b) weak vector boson fusion, (c) associated production with a weak boson, (d) associated production with a pair of $t\bar{t}$.

the forward and backward directions (emitting from the two final quarks) and not in the central region. While the QCD background proceeds via colour exchange of the incident partons and where the gluons are often in the central region. Therefore applying jet-vetoes in the central region will substantially reduce the QCD backgrounds.

The associated production with W/Z bosons

At leading order, the Higgs particle is produced in association with the massive gauge bosons, which then decay into two fermions. This contributes as the third dominant cross section for Higgs production at the LHC. The corresponding Feyman diagram is (c) in Figure 4.5.

Associated Higgs production with a pair of top-quarks

At tree-level, the process originates from a pair of quark-antiquark annihilation creating a pair of top-antitop quarks and the Higgs boson emitted from the mediator top-quark line; at higher energy like at the LHC, the processes with gluons becomes significant, this production mode is mainly through gluon fusion and the Higgs boson is emitted from both the external and internal top-quark line (see Feyman diagram (d) in Figure 4.5 for the latter).

4.2.2 The Higgs total decay width and branching ratios

Since the Higgs coupling to particles are proportional to their masses so at the LHC, taking into account the PDFs of partons inside a proton, the various decay modes of the Higgs boson is as the following.

Considering the fermions mode, in the "low mass" range 110 GeV $\lesssim M_H \lesssim$ 130 GeV, the main decay mode of the Higgs boson is $H \to b\bar{b}$ with a branching ratio of the order greater than 50% for $M_H = 115 - 130$ GeV, followed by the decays into $\tau^+\tau^-$ and $c\bar{c}$ pairs with branching ratios of the order of greater than 5% and 2%, respectively.

Considering the bosons mode, the $H \to gg$ decay with a branching fraction of around 7% for $M_H \sim 120$ GeV. The $\gamma\gamma$ and $Z\gamma$ decays are rare, with branching ratios at the level of a few per mille, while the decays into pairs of muons and strange quarks are at the level of 10^{-4}. The $H \to WW^*$ decay is $\sim 30\%$ at $M_H \sim 130$ GeV while $H \to ZZ^*$ occurs at the percent level with that Higgs mass value. Figure 4.6 shows the branching ratios BR of different decay channels of the SM Higgs boson as a function of the Higgs' mass, figure is from LHC Higgs cross section working group (LHCHXSWG) [46].

For the total decay width, the Higgs boson is very narrow in the low mass range, $\Gamma_H < 10$ MeV. The recent result of SM width ($M_H = 125.1$ GeV) is 4.1 MeV(result from LHCHXSWG [46]).

Table 4.1 listed the most recent observed Higgs branching ratios at $M_H =$ 125.1 GeV obtained by combining Higgs results from ATLAS and CMS collaborations. This table is presented at The European Physical Society Conference on High Energy Physics (EPS-HEP) conference in Vienna 2015.

Process X	BR($H \to X$)
bb	0.58
WW	0.22
$\tau\tau$	0.06
ZZ	0.027
$\gamma\gamma$	0.0023
$Z\gamma$	0.0016
$\mu\mu$	0.0002

Table 4.1: Recent result branching ratios of the Higgs at $M_H = 125.1$ GeV from ATLAS and CMS combination presented at EPS conference in Vienna 2015.

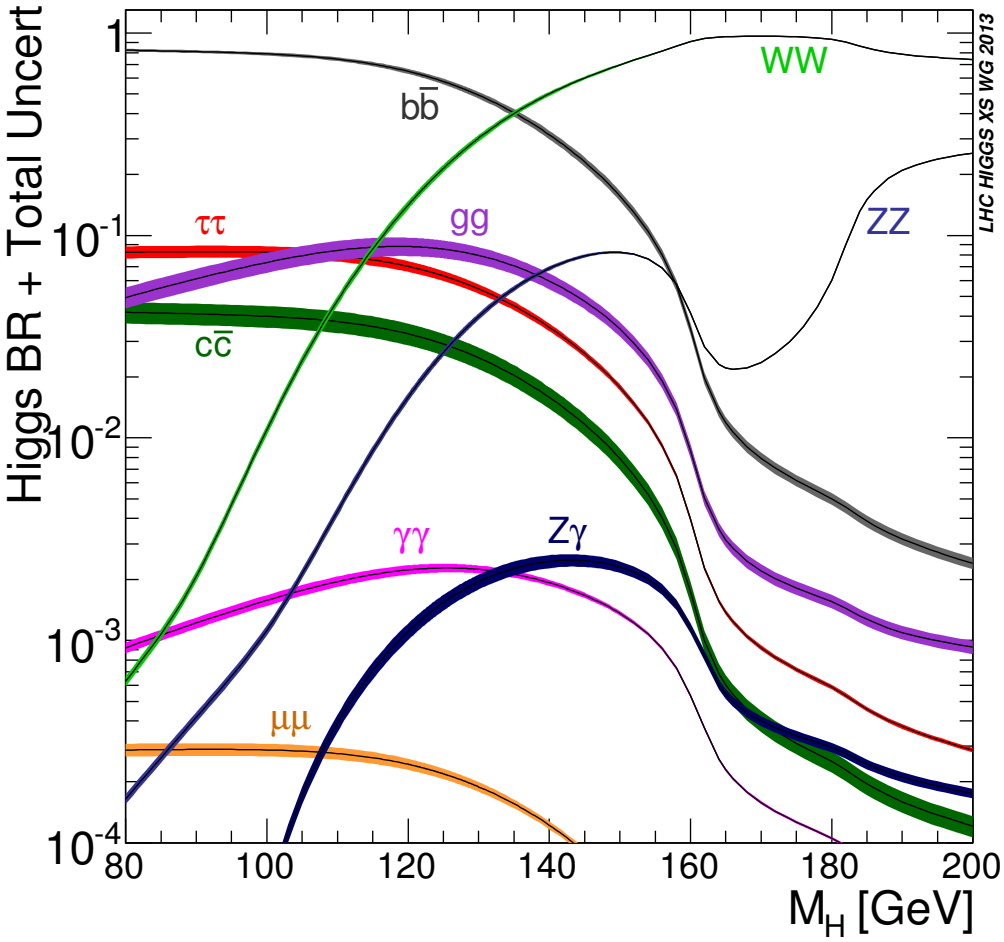

Figure 4.6: The branching ratios BR of the SM Higgs boson as a function of the Higgs' mass at the LHC from the LHCHXSWG.

4.3 The Higgs Discovery at the LHC

Since the time of being proposed in the 60s by Peter Higgs, François Englert and some other physicists, there were searches at different colliders such as Tevatron, LEP to find the Higgs boson. Those searches narrowed down the mass range of the possible "Higgs boson" rather than claiming any discovery until the operation of the LHC since 2010. Accumulating data in 2011 and a part of 2012, the ATLAS and CMS experiments announced the observation of a Higgs-like boson in July 2012. CMS saw the signal with mass 125.3 ± 0.4 (stat) ± 0.5 (syst) GeV [41], the excess is most significant in the two decay modes with the best mass resolution, $H \to \gamma\gamma$ and $H \to ZZ^* \to 4\ell$. ATLAS saw a boson with mass 126.0 ± 0.4 (stat) ± 0.4 (syst) GeV [40], the excess is also more significant in the diboson channels $H \to ZZ^* \to 4\ell$, $H \to \gamma\gamma$ and $H \to WW^* \to \ell\nu\ell\nu$.

Further measurements done by the two collaborations for its properties agree with the SM spin-parity $J^P = 0^+$ hypothesis [47, 48], showed evidence of Higgs produced via VBF [49]. The recent combined Higgs mass measurement of ATLAS and CMS Collaborations results: $m_H = 125.09 \pm 0.21(stat.) \pm 0.11(syst.)$ GeV [50]. The combination of the Higgs boson production and decay rates as well as its coupling strengths to vector bosons and fermions results the measured signal yield, normalised to the SM expectation, as $1.18^{+0.15}_{-0.1}$ by ATLAS [51] and $1.00 \pm 0.09(stat)^{+0.08}_{-0.07}(theo) \pm 0.07(syst)$ by CMS [52]. All measurements are consistent with expectations for the SM Higgs boson.

4.4 Probe of Invisible Higgs Boson Decays

The Higgs boson may decay to very weakly interacting particles, that produce no significant signal in the detector. Such final states are termed "invisible" and can be inferred indirectly through missing transverse momentum. The observed decaying branching ratios of the Higgs boson to SM di-bosons (on-shell and off-shell), fermions as listed in table 4.1 still leaves an open window for the branching ratio of the Higgs boson decaying to invisible particles. One can use the measurement of cross sections time branching ratios of different channels to indirectly put a constraint on the invisible branching ratio.

As mentioned in Chapter 1 there are many direct searches for the invisible decay of the Higgs boson. They are: the same VBF process with the analysis presented in this thesis done by CMS [14, 53], using process $ZH \to \ell\ell + E_{\mathrm{T}}^{\mathrm{miss}}$ signature by both the ATLAS and CMS Collaborations [35, 54], using the associated production with a vector boson, VH, where $V \to jj$ and $H \to$ invisible by ATLAS [55] giving upper limits at 95% CL of 57%, 65%, 75%, and 78% on the branching ratio of the Higgs boson decaying invisibly, respectively. Other searches for large $E_{\mathrm{T}}^{\mathrm{miss}}$ in association with one or more jets have been performed in [17–20], they are primarily sensitive to the ggF process and have significantly larger backgrounds so the results are less competitive.

The analysis using VBF Higgs production process to search for the invisible decay of the Higgs boson is presented in Chapter 6 followed by Chapter 7 discusses a combination of all the ATLAS direct searches to the invisible Higgs decay.

Chapter 5

Physics Objects Reconstruction

To increase the possibility of interacting between protons from opposite beams inside a detector, around a trillion of protons are squeezed into a bunch then meets another at the centre of the detector. As a result, there are generally more than one proton-proton collision in a bunch crossing. In addition to the hard process from two protons, further semi-hard interactions may occur between the partons of two other incoming protons causing "pileup".

After every proton collision inside the ATLAS detector, a huge number of electric signals is produced in each sub-detector. Further work has then to be done to find interesting physics signatures: reconstruct objects inside detectors, identify whether they come from the interested events or pileups. With the help of the reconstruction software, we can convert the electric signals into physics information to identify particles and reconstruct their energies, momenta, trajectories, etc. The reconstruction proceeds in three stages. At first, data from each detector is reconstructed in a stand-alone mode. Secondly, the information from all detectors is combined to get the most accurate measurements and identification of the final objects used in the analysis: photons, electrons, muons, taus, jets, b-jets, missing transverse momentum or $E_{\mathrm{T}}^{\mathrm{miss}}$, etc. The third stage is the analysis-specific part: reconstruction of exclusive B hadron decays, W bosons, Z bosons, top quark decays, Higgs bosons, Super Symmetry (SUSY) particles, etc.

Among the SM particles produced at the LHC, electrons, neutrinos and photons are the only reconstructable stable particles. Since the LHC operates at a very high centre-of-mass energy, muon with a lifetime $\tau_{\mu} \sim 2.2 \times 10^{-6}$ s can penetrate a path of 2.2×10^{-6} s $\times\, c = 6.6 \times 10^{2}$ m and can be considered stable too. The tau, charm and bottom are instead short-lived particles. Quarks and gluons create jets of hadrons which then can be seen through their stable decay products.

In this chapter, the physics objects, which are used in the search of vector boson fusion production of the Higgs decaying into invisible particles, are mainly discussed such as electron, muon, tau, jets, $E_{\mathrm{T}}^{\mathrm{miss}}$. Their reconstruction is described in the following Sections 5.1, 5.2, 5.3,5.4 and 5.5.

Figure 5.1 sketches how different particles behave in the different sub-detectors

where they are detected and reconstructed. Electrons leave tracks in the ID and deposit energy in the EMCAL. Photons are neutral so they don't leave any tracks in the ID and deposit their energies in the EMCAL. Muons penetrate through all the sub-detectors leaving track in the ID and the Muon Spectrometer, depositing some energy in the calorimeters. Charged hadrons leave tracks in the ID, some energy in the EMCAL and most of their energies in the HCAL. Neutral hadrons don't create any tracks in the ID but deposit energies in the HCAL. Neutrinos are not detected at all by any of the sub-detectors because of their weakly interacting characteristic.

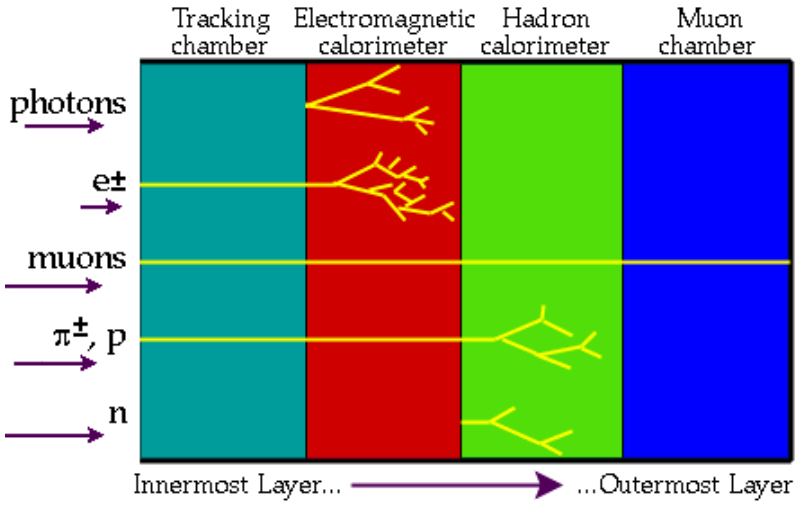

Figure 5.1: Decay Chart of particles travelling through different ATLAS sub-detectors. [1]

5.1 Electrons

Electron is the lightest charged lepton in the SM and stable. Electrons are reconstructed using information from both the Calorimeters (energy deposit) and Inner Detector (track and momentum) [56]. The trusty range is $|\eta| < 2.47$ - the Inner Detector coverage to have a good electron's trajectory.

Electron from top-quark, W-boson, Z-boson decay are usually "isolated", i.e. are produced outside jets. Non-isolated electrons can come from bottom and charm quarks, which hadronize and give many jets in the final states. Those electrons are close to the jets containing in the b- and c-hadrons.

ATLAS applies a simple cut-based method to classify electrons into three classes of quality, each with different degrees of true electron efficiency and fake rejection

- Loose electrons: candidates passing requirements on hadronic leakage as well as lateral shower shape and cluster width variables based on the middle layer of

[1] Figure from http://www.atlas.ch

the EM calorimeter. They have the best efficiency, but the lowest background rejection.

- Medium electrons: further required to pass quality cuts on strips in the first layer of the EM calorimeter as well as inner detector tracks. These selections increase background rejection by a factor of 3 or 4 and reduce the reconstruction efficiency by $\sim 10\%$.

- Tight electrons: using TRT in distinguishing electron from other charged particles because electron has greater path length through the radiator material and fewer straw detectors. Further cuts on the number of vertex layer hits; on the number of TRT hits; on the ratio of high threshold to total TRT hits; on the difference in η and ϕ between the cluster and track; and on E/p. At this point two different selections can be chosen depending on the expected electron topology: A tight calorimeter isolation requirement based on cells within $\Delta R < 0.2$ of the EM cluster, or tighter TRT selections based on already selected TRT variables.

The electrons used in the analysis described in this thesis are tight and medium electrons.

For the sake of information, another EM object-photon, is purely narrow electromagnetic object and it deposits energy primarily in the second layer of the EMCAL, thus, it can be reconstructed.

5.2 Muons

Muon leptons decay preferably into electrons in 3-body decay with the BR($\mu \rightarrow e + \dots$) $\approx 100\%$. However, their lifetime is rather long $\tau_\mu = 2.2 \times 10^{-6}$ s and at the LHC its free path $\approx 10^{-6} \times c = 6.6 \times 10^2$ m, so it can penetrate through all the detectors and leave a track in the muon chamber. Therefore, muons, especially those with high p_{T} and those that are isolated (from other activities in the detector) are much more difficult to fake than electrons.

The muon spectrometer covers the pseudo-rapidity range $|\eta| < 2.7$ and allows identification of muon with momenta above 3 GeVand precise determination of p_{T} up to around 1TeV. Energy measurements in the calorimeter can aid in muon identification because of their characteristic minimum ionizing signature and can provide a useful direct measurement of the energy loss. ID detects muon and other charged particles with hermetic coverage for $|\eta| < 2.5$, therefore providing important confirmation of muon found by the spectrometer over that η range.

There are different strategies to reconstruct and identify a muon: "standalone muon" by finding tracks in the muon spectrometer and then extrapolating these to the beam line, "combined muons" by matching standalone muons to nearby inner detector tracks and then combining the measurements from the two systems,

"tagged muon" by extrapolating inner detector tracks to the spectrometer detectors and searching for nearby hits. For each strategy, there are two algorithms: Staco and Muid.

The analysis in this thesis selects StacoCB candidates meaning muons reconstructed by Staco algorithm with the combined approach requiring a match between a track in the inner detector and a track in the muon spectrometer [57].

5.3 Tau

Tau is the heaviest charged lepton in the SM, at ATLAS tau decays before reaching to the ID (tau free path length $c\tau_\tau = 87$ μm). It decays via electroweak interaction hadronically almost 65% and leptonically into electron or muon almost 35%. However, leptonic modes cannot realistically be separated from directly produced electrons or muons, and there are not yet any experimental handle whether they originated from a tau. Therefore, tau is usually hadronically reconstructed [58].

Interesting transverse momentum range of tau spans from less than 10 GeV up to at least 500 GeV. Tau reconstruction is done only for the visible part of the decay products, about 55% of the energy is carried by π (generally one or three $\pi^{\pm}$ possibly accompanied by one or more π^0) present among the decay products. Tau is reconstructed as the following, using discriminating variables calculated from tracking and calorimeter information. Firstly, the three-dimensional topological cluster around calorimeter cells with significant energy compared to noise ($|E| > 4\sigma$ of noise) is built. Secondly, the clusters are calibrated using the local topology of the energy depositions. Tau jets are reconstructed by using the Anti-kt jet algorithm with distance parameter 0.4 (more about jet reconstruction in Section 5.4) on calibrated clusters and consider jets within tracking acceptance ($|\eta| < 2.5$) as tau candidate. Then it is combined with the ID's information on the charged hadronic track or the collimated multi-track system reconstructed in isolation from the rest of the event. These tracks should neither match track segments in the muon spectrometer nor reveal features characteristic of an electron track (e.g high threshold hits in TRT). In the case of a multi-track system, they should be well collimated in (η, ϕ) space and the invariant mass of the system should be less than the mass of the tau lepton.

5.4 Jets Reconstruction

Hard proton-proton scattering results in the fragmentation of the colour partons inside the protons, with each fragment carrying away some of the colour charges. Because of the QCD confinement, the fragments-quarks cannot exit from collisions in free states but undergo the process called hadronization (except top-quark will decay before) by involving in other colour quarks to create colourless objects, baryons and mesons. Those hadronic particles create collimated clusters which we call "jets"

inside the EMCAL (EM jets) and mostly the HCAL (hadronic jets) depending on the initial energy of the original quarks or gluons. The reconstruction of jets is briefly discussed below.

The EM jets are created by the electromagnetic interaction of charged particles and photons with the absorbers and produce showers of electrons, positrons and photons. The hadronic jets are created by strong interaction of hadrons with the absorbers and produce more showers of hadrons which cross the scintillators in HCAL causing light emissions. The hadronic showers take longer to develop and generate less signal than the electromagnetic ones which deposit the same energy. The reconstruction of jets then is based on the cells' information: energy, time, quality and gain. Primarily, the cells are calibrated with electrons so the signals are correct at EM scale for EM showers. Due to all those reasons, the hadronic scale is underestimated, and because the ATLAS calorimeters are non-compensating, thus further jet calibration is needed to give corrections for jets' energies and momenta.

There are several jet collections determined by tools to reconstruct jets called Jet Finders. A jet collection is defined by the following information for the corresponding Jet Finder: input type, algorithm type, calibration method to be described below.

- Input to Jet Finder can be either of the following objects.
  - Truth particles: using simulated particles (which are interacting and are not muons) as constituents to build truth jets. This allows to retrieve the full truth history of a jet constituent for simulated events.
  - Calorimeter Towers: are built from a two-dimensional grid in pseudo-rapidity (η) and azimuthal angle (ϕ) with a grid size of $\eta \times \phi = 0.1 \times 0.1$, filled with the calorimeter cell energies calibrated at the EM scale.
  - TopoClusters: means topological clusters. It can be either clusters at the EM scale or local hadronic calibration (LC) meaning calibrated TopoClusters. Cluster formation follows a 4/2/0 algorithm: first seed cells are identified with energy above 4σ where σ is the sum in quadrature of electronic and pile-up noise, then seed clusters are formed by iteratively adding all neighbours having energy higher than 2σ, and then adding an extra ring of direct neighbour cells to the final cluster
- Jet Finder algorithm: the so-called jet clustering procedure consists basically in grouping some 4-momenta from a given set (the jet constituents) into different sub-sets (the jets, the jet 4-momentum being the sum of 4-momenta in the subset). There are two groups of algorithms: cone algorithms and cluster algorithms
  - Cone Algorithms: applied to a wide range of jet algorithms which broadly aim to maximise energy (or p_{T}) in a geometric cone. The cone gives a circle when projected in $(\eta - \phi)$ space, and the radius of the circle, R, is a key parameter of the algorithm.

  - Cluster Algorithms: based upon pair-wise clustering of the initial constituents. In general, the algorithms define a distance measured between objects, and also some conditions upon which clustering should be terminated. Amongst cluster algorithms, ATLAS has chosen the Anti-k_t [59] clustering algorithm as its preferred Jet Finder. For Anti-k_t, the combination depends on jet p_{T} and angular distance in (η, ϕ) space, highest constituents are clustered first. An advantage of this algorithm is that high p_{T} Anti-k_t jets have regular shapes and are stable under pile-up.

- Calibration method: ATLAS is considering two approaches for jet calibration: a global calibration in which the jets are calibrated once built out of calorimeter object at EM scale and a local calibration where jets are built from hadronic-calibrated calorimeter clusters.

  - Global Calibration: In this method truth jets are matched to reconstructed jets. The weights to correct for calorimeter non-compensation and dead-material losses are derived from a fit that gives the best resolution of the reconstructed jet with respect to the true jet.
  - Local Hadronic Calibration (LC) [60, 61]: A bottom-up approach that first calibrates the calorimeter cluster by discriminating EM and hadronic cluster, and also identifying and correcting various losses separately.

For the analysis presented in this thesis, LCTopo jets are used meaning that jets are reconstructed from local calibrated energy clusters, using the anti-k_{t} algorithm with radius parameter $R = 0.4$. Jets are corrected for pileup using the event-by-event jet areas subtraction method and calibrated to particle level by a multiplicative jet energy scale factor [60, 61].

5.4.1 b Reconstruction (b-tagging algorithms)

The b-quark is the second heaviest quark in the SM, around 4.2 GeV. Therefore it can decay both hadronically and leptonically via weak interaction and create jets containing B-hadrons. It also appears dominantly in top-quark decay, so it is a very important object for top-quark identification; in the analysis presented in this thesis, we want to suppress background from top-quark decays.

Among the properties of b-jets we have the following: first, the fragmentation is hard and the b-hadron retains about 70% of the original b quark momentum. In addition, the mass of B-hadrons is relatively high (greater than 5 GeV). Thus, their decay products may have a large transverse momentum with respect to the jet axis and the opening angle if the decay products is large enough to allow separation. The third and most important property is the relatively long lifetime of B-hadrons, of the order of 1.5 ps so it can travel up to a distance $L = c.\tau \sim 0.45\ mm$). The

tracks from B-hadron decay products tend to have rather large impact parameters which can be distinguished from tracks stemming from the primary vertex.

The goal of b-tagging algorithms is to identify jets containing B-hadrons by assigning a b-weight (w) for each selected jet to reflect the probability that the jet originates from a b-quark. The algorithms (or "taggers") can be defined, based on these discriminating variables: L, impact parameters d_0 [2] and z_0 [3] and on secondary vertex properties as well as on the presence of leptons within b-quark jets. Different threshold cuts (known as "working point") on the w variable is defined for each tagging algorithm to define a "tagged" jet. The choice of the working point sets the tagging efficiencies for b-, c- and light quark jets. For the analysis presented in this thesis, 0.80 working point is used meaning that the tagging efficiency for b-quark jets is 80%.

5.5 Missing transverse momentum

Neutrinos only interact weakly with the detector material and therefore do not produce a signal. ATLAS is not able to identify them in a direct way but in an indirect way. Besides the SM neutrinos, there are many models such as SUSY and Dark Matter models which predict weakly interacting particles. Those neutrinos and the predicted particles are not detected by the ATLAS detector and therefore carry away a fraction of the constituents' momenta leading to a "missing momentum". Knowing this quantity of missing momentum will help us to detect these weakly interacting particles. However, the exact momentum of the protons' constituents which collide is not known, while we know that their momenta in the transverse plane must be 0. Based on the conservation of energy and momentum in the transverse plane, the so called missing transverse momentum $E_{\mathrm{T}}^{\mathrm{miss}}$ can be reconstructed.

For the analysis presented in this thesis, the $E_{\mathrm{T}}^{\mathrm{miss}}$ is constructed as the magnitude of the negated vectorial sum of the transverse momenta of all calibrated objects (identified electrons, muons, photons, hadronic decays of tau-leptons, and jets) and an additional term for transverse energy in the calorimeter not included in any of the other objects [62].

[2] The transverse impact parameter, d_0 is the distance of closest approach of the track to the primary vertex point, in the $r - \phi$ projection.

[3] The longitudinal impact parameter, z_0, is the z coordinate of the track at the point of closest approach to the primary vertex

Chapter 6

Search for an invisibly decaying Higgs boson produced via weak boson fusion

This chapter presents a search for the Higgs boson produced via the VBF process (see Section 4.2.1) and then decays into invisible particles (objects not directly identified in the detector) [11]. Based on the kinematic characteristic of VBF topology, the main production mode considered is the VBF Higgs boson production. In addition, there is a smaller contribution due to the 2-jet final state from the gluon fusion (ggF)+2 jets process (treated as signal), depending on the selections applied. The search is performed with a dataset corresponding to an integrated luminosity of 20.3 fb^{-1} (see Figure 6.1 [1]) of proton-proton collisions at $\sqrt{s} = 8$ TeV, recorded by the ATLAS detector at the LHC.

The search is theoretically well motivated [63]: VBF channel is the most promising channel to search for the invisible decay of the Higgs boson because it is the second dominant production mode at the LHC and its unique signature can be used to effectively remove the physics backgrounds. VBF Higgs invisibly decay is the process where two initial quarks radiate weak bosons (W or Z) which fuse to produce a Higgs boson, and scatter off two final quarks. Hence it can be identified by the presence of two jets (from the two final quarks) with a large separation in pseudo-rapidity and a large amount of missing momentum in the transverse plane $E_{\text{T}}^{\text{miss}}$ (from the Higgs' invisible decay). The process has large backgrounds from the W/Z+jets processes, where a Z decays to two neutrinos or a W decays leptonically with the lepton not reconstructed (see Figure 6.2 for the Feynman diagrams of VBF signal and Z boson background). The QCD production of multijet event contributes a minor fraction of background while all the other backgrounds (di-boson, top-antitop, single top-quark production, ...) are negligible. The VBF process, in its most extreme topology (high di-jet invariant mass for example), offers strong rejec-

[1] Figure is from https://twiki.cern.ch/twiki/bin/view/AtlasPublic/LuminosityPublicResults.

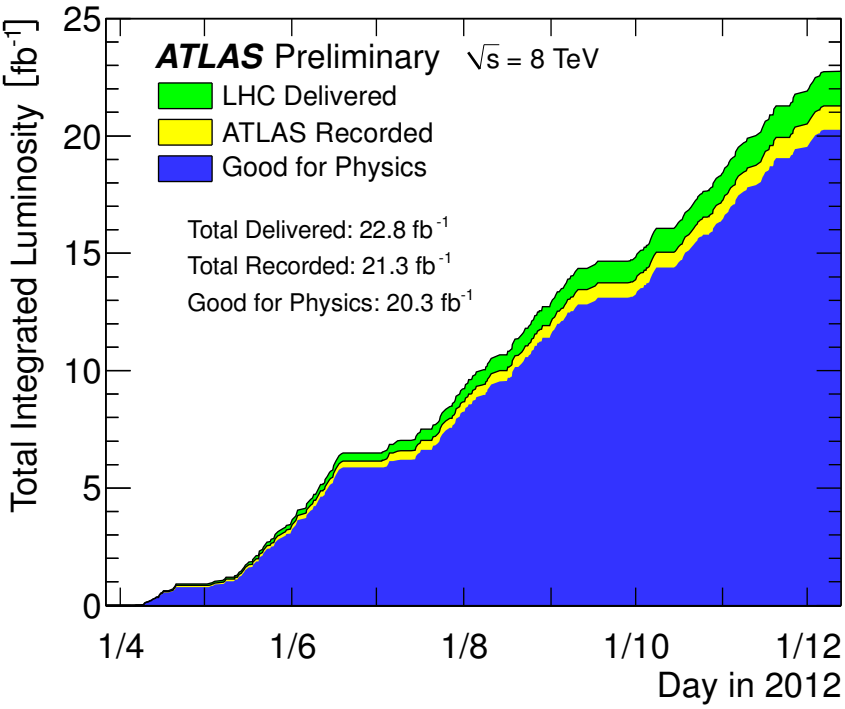

Figure 6.1: The integrated luminosity recorded by the ATLAS detector in 2012. The blue area shows the total integrated luminosity which is used for this analysis.

tion against the QCD-initiated V (W, Z)+jets backgrounds. The resulting selection has a significantly better signal-to-background ratio than the selections targeting the ggF process.

The chapter is organized as follows. The signal and background modellings are presented in Section 6.1. The dataset, triggers, event reconstruction, and event selection with the signal region definitions are described in Section 6.2. The background estimations are presented in Section 6.3. In Section 6.4, the systematic uncertainties are discussed. The results are shown in Section 6.5, and interpretations are presented in Section 6.6 and 7.3 (after the combination of all Higgs to invisible decay searches). Finally, concluding remarks are given in Section 8.

The work was done with many contributions from different members of the working group, not all are written here since many of them are cross checks, validations and contain technical details. My main contributions which are worth mentioning: acceptance challenge to define the set of all the cuts designed to optimize signal and background separation, cross checking the dominant W+jets background determination, estimate the uncertainties on the Higgs p_{T} distribution for the gluon fusion Higgs production with two jets signal, construct and validate the limit setting procedure to get the final result.

6.1 Simulation

Simulated signal and background event samples to be compared with data events are produced using Monte Carlo (MC) event generators, passed through a GEANT4 [64] simulation of the ATLAS detector [13] and reconstructed with the same software as the one used for the data. Additional pp collisions in the same and nearby bunch-crossings (pileup) are included by merging diffractive and non-diffractive pp collisions simulated with PYTHIA-8.165 [65]. The multiplicity distribution of these pileup collisions is re-weighted to agree with the distribution in the real data.

Both the VBF and ggF signals are modelled using POWHEG-BOX [66–71] with CT10 PDFs [72] as structure functions, and PYTHIA-8.165 to simulate the parton shower, hadronization and underlying event[2]. The VBF and ggF Higgs boson production cross sections and their uncertainties are taken from Refs. [46]. The transverse momentum (p_{T}) distribution of the VBF Higgs boson is re-weighted to reflect electroweak (EW) radiative corrections computed by the HAWK-2.0 [73] code. The ggF contribution to the signal is re-weighted [74, 75] so that the p_{T} distribution of the Higgs boson in events with two or more associated jets matches that of the next-to-leading-order (NLO) ggF+2jets calculation in POWHEG-BOX MiNLO [76], and the inclusive distributions in jets match that of the next-next-to-leading-order (NNLO) and next-to-next-to-leading-logarithm (NNLL) calculation in HRES-2.1 [77]. The effects of finite quark masses are also included [71].

For the most relevant backgrounds, one has to have dedicated control samples (more in Section 6.2). For $W(\to \ell\nu)$+jets and $Z(\to \ell\ell)$+jets processes are generated using SHERPA-1.4.5 [78] including leading order (LO) matrix elements for up to five partons in the final state with CT10 PDFs and these matrix elements are merged with the parton shower following the procedure described in Ref. [79]. The $W(\to \ell\nu)$+jet and $Z(\to \ell\ell)$+jet processes are divided into two components based on the number of electroweak vertices in the Feynman diagrams. Diagrams which have only two electroweak vertices contain jets that are produced via strong interaction, and are labeled "QCD" Z+jets or W+jets. Diagrams which have four electroweak vertices contain jets that are produced via the electroweak interaction, and are labeled "EW" Z+jets or W+jets [80]. The MC predictions of the QCD components for W+jets and Z+jets are normalized to NNLO in FEWZ [81, 82], while the EW components are normalized to VBFNLO [83], with the latter calculation including the jet p_{T} and di-jet invariant mass requirements. Finally, the interference between the QCD and EW components of Z+jets and W+jets is evaluated with the SHERPA-1.4.5 simulation to be 7.5–18.0% of the size of the EW contribution depending on the signal regions and is included by scaling up the EW contribution by the estimated size of the interference term. Figure 6.2 shows the leading order Feynman diagrams for the signal, one of the possible diagram describing the vector boson background.

[2]The invisible decay of the Higgs boson is simulated by forcing the Higgs boson (with mass $m_H = 125$ GeV) to decay via $H \to ZZ^* \to 4\nu$.

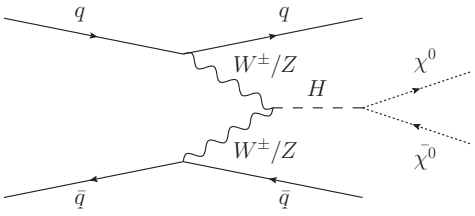

(a) Signal

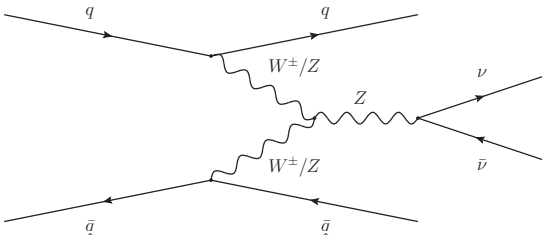

(b) Strongly produced (QCD) Z+jets

(c) Weakly produced (EW) Z+jets

Figure 6.2: Feynman diagrams for the signal and example vector boson backgrounds.

There are additional small backgrounds from $t\bar{t}$, single top, di-boson and multijet production. The $t\bar{t}$ process is normalized and modeled using POWHEG-BOX, with PYTHIA-8.165 modeling the parton shower, hadronization and underlying event. Single-top production samples are generated with MC@NLO [84] for the s- and Wt-channel [85], while ACERMC-v3.8 [86] is used for single-top production in the t-channel. A top-quark mass of 172.5 GeV is used consistently. The AUET2C and AUET2B [87] set of optimized parameters for the underlying event description are used for the $t\bar{t}$ and single-top processes. CT10 and CTEQ6L1 [88], respectively are the PDFs. Approximate NNLO+NNLL pQCD cross sections, as determined in TOP++-2.0 [89], are used in the normalization of the $t\bar{t}$ [90] and Wt [91] samples. Di-boson samples $W\gamma$, $Z\gamma$, WW, WZ and ZZ ($\rightarrow \ell\nu\nu\nu, \ell\ell\nu\nu, \ell\ell\ell\nu, \ell\ell\ell\ell$) are normalized at NLO and generated in HERWIG-6.5.20 [92] with CT10 PDFs including the parton shower and hadronization, and Jimmy [93] to model the underlying event, whereas the WW, WZ, and ZZ ($\rightarrow \ell\ell qq, \nu\nu qq$) processes are generated together with EW W+jets and Z+jets samples. Di-boson WW, WZ and ZZ ($\rightarrow \ell\ell qq, \nu\nu qq$) samples generated in SHERPA-1.4.5 with CT10 PDFs and normalized with NLO pQCD predictions [94] are used as a cross check. Multijet and γ+jet samples are generated using PYTHIA-8.165 with CT10 PDFs.

6.2 Event Selection

The analysis uses a range of samples modelling processes with various physics objects such as $E_{\mathrm{T}}^{\mathrm{miss}}$, jets, leptons (e, μ). The physics object selections are defined depending on the standard ATLAS recommendations as well as on the kinematic properties of the corresponding processes.

The invisible decay products of the Higgs boson cannot be seen by the ATLAS detector so events with large $E_{\mathrm{T}}^{\mathrm{miss}}$ is required. The data used in this analysis were recorded with a $E_{\mathrm{T}}^{\mathrm{miss}}$ trigger (see Section 3.3.5) during periods when all ATLAS sub-detectors were operating under nominal conditions. This trigger is not fully efficient until the offline $E_{\mathrm{T}}^{\mathrm{miss}}$ is greater than 150 GeV.

LCTopo jets (see Section 5.4) are used, the selected jets are required to have $p_{\mathrm{T}} > 20$ GeV and $|\eta| < 4.5$ for jets to be in the central region of the detector. To discriminate against jets originating from minimum bias interactions, selection criteria are applied to ensure that most of the jet transverse momentum, for jets within $|\eta| < 2.5$, is associated with tracks originating from the primary vertex, which is taken to be the vertex with the highest summed p_{T}^2 of associated tracks. Information about the tracks and clusters in the event is used to construct multivariate discriminators to veto events with b-jets and hadronic τ-jets. The requirements on these discriminators identify b-jets with 80% efficiency (estimated using $t\bar{t}$ events) [95], one-track jets from hadronic τ decays with 60% efficiency (measured with $Z \to \tau\tau$ events), and multiple-track jets from hadronic τ decays with 55% efficiency [58].

Medium electrons, tight electrons (see Section 5.1) and StacoCB muons (see Section 5.2) are used.

The $E_{\mathrm{T}}^{\mathrm{miss}}$ (see Section 5.5) is constructed as the magnitude of the negated vectorial sum of the transverse momenta of all calibrated objects (identified electrons, muons, photons, hadronic decays of tau-leptons, and jets) and an additional term for transverse energy in the calorimeter not included in any of the other objects [62].

The event selections in this analysis is well motivated by the kinematic characteristic of the Higgs production via VBF process (see Section 4.2.1). The selection defines three orthogonal signal regions, SR1, SR2a and SR2b. They are distinguished primarily by the selection requirements on the invariant mass m_{jj} of the two highest p_{T} jets and their separation in pseudo-rapidity $\Delta\eta_{jj}$. For each signal region, there are two dedicated control regions where the requirements on leptons are reversed with the processes of $Z(\to \ell\ell)$+jets and $W(\to \ell\nu)$+jets, $(\ell = e, \mu)$ to study the backgrounds $Z(\to \nu\nu)$+jets and $W(\to \ell\nu)$+jets in the signal region. Depending on which signal region, some validation regions (which are signal depleted) are defined to validate the background estimates as well as the statistical methods used for getting the result.

The SR1 selections require events to have two jets: one with $p_{\mathrm{T}} > 75$ GeV and one with $p_{\mathrm{T}} > 50$ GeV. Events must have $E_{\mathrm{T}}^{\mathrm{miss}} > 150$ GeV in order to suppress the background from multijet events. To further suppress the multijet background, the two leading jets are required to have a transverse opening angle $|\Delta\phi_{jj}| < 2.5$ radians

and a transverse opening angle with respect to the $E_{\mathrm{T}}^{\mathrm{miss}}$ of $|\Delta\phi_{j,E_{\mathrm{T}}^{\mathrm{miss}}}| > 1.6$ radians for the leading jet and $|\Delta\phi_{j,E_{\mathrm{T}}^{\mathrm{miss}}}| > 1$ radian otherwise. In the VBF process, the forward jets tend to have large separations in pseudo-rapidity ($\Delta\eta_{jj}$), with correspondingly large di-jet masses, and little hadronic activity between the two jets. To focus on the VBF production, the leading jets are required to be well-separated in pseudo-rapidity $|\Delta\eta_{jj}| > 4.8$, and have an invariant mass $m_{jj} > 1$ TeV. Events are rejected if any jet is identified as arising from the decay of a b-quark or a τ-lepton. The rejection of events with b-quarks suppresses top-quark backgrounds, especially in the $W(\rightarrow e\nu/\mu\nu)$+jets control region. Similarly, rejection of events with a τ-lepton suppresses the $W(\rightarrow \tau\nu)$+jets contribution to the signal region and the $W(\rightarrow e\nu/\mu\nu)$+jets control region. Further, events are vetoed if they contain any reconstructed leptons passing the transverse momentum thresholds $p_{\mathrm{T}}^{e} > 10$ GeV for electrons, $p_{\mathrm{T}}^{\mu} > 5$ GeV for muons, or $p_{\mathrm{T}}^{\tau} > 20$ GeV for τ-leptons. Finally, events with a third jet having $p_{\mathrm{T}} > 30$ GeV and $|\eta| < 4.5$ are rejected. The expected yields in the SR1 expected for 20.3 fb^{-1} of $\sqrt{s} = 8$ TeV data are shown in Table 6.1.

Cut	ggH Signal	VBF Signal	QCD $Z \rightarrow \nu\nu$+jets	EW $Z \rightarrow \nu\nu$+jets	QCD+EW W+jets	Dijets	Other BGs	Total BG
$\Delta\eta_{jj} > 4.8$	156 ± 17.2	766 ± 8.40	2333 ± 39.1	503 ± 6.27	3702 ± 63.2	289317 ± 158130	38.8 ± 1.37	295895 ± 158130
m_{jj} >1 TeV	129 ± 15.6	673 ± 7.87	1739 ± 33.0	464 ± 6.02	2983 ± 55.3	188684 ± 130368	30.8 ± 1.22	193900 ± 130368
$\Delta\phi_{jj} < 2.5$	126 ± 15.4	606 ± 7.47	1375 ± 29.3	327 ± 5.06	2149 ± 47.0	114195 ± 108395	23.3 ± 1.04	118069 ± 108395
Jet Veto	63.2 ± 10.9	529 ± 6.98	680 ± 22.0	272 ± 4.61	975 ± 31.2	-	2.03 ± 0.38	1928 ± 38.5
$\Delta\phi_{j_{2}x,MET} > 1$	63.2 ± 10.9	522 ± 6.94	667 ± 21.9	265 ± 4.55	942 ± 30.8	-	1.96 ± 0.37	1875 ± 38.1
$E_{\mathrm{T}}^{miss} > 150$ GeV	17.1 ± 5.51	267 ± 4.96	214 ± 8.00	111 ± 2.95	225 ± 10.6	-	0.71 ± 0.21	550 ± 13.6

Table 6.1: Expected yields after successive cuts in 20.3 fb^{-1} of 2012 data, as evaluated using Monte Carlo.

The SR2 consists of events which have either $500 < m_{jj} < 1000$ GeV, $\eta_{j1} \times \eta_{j2} < 0$, and $|\Delta\eta_{jj}| > 3$ (SR2a), or $m_{jj} > 1000$ GeV and $3 < |\Delta\eta_{jj}| < 4.8$ (SR2b). Several other selections common to SR2a and SR2b also differ from the ones of SR1. First, the leading jet is required to have $p_{\mathrm{T}} > 120$ GeV and $|\eta| < 2.5$. Additionally, the sub-leading jet is required to have $p_{\mathrm{T}} > 35$ GeV, the $\Delta\phi_{jj}$ requirement is removed, the requirement on $\Delta\phi_{j,E_{\mathrm{T}}^{\mathrm{miss}}}$ is relaxed to $|\Delta\phi_{j,E_{\mathrm{T}}^{\mathrm{miss}}}| > 0.5$, and the $E_{\mathrm{T}}^{\mathrm{miss}}$ requirement is tightened to $E_{\mathrm{T}}^{\mathrm{miss}} > 200$ GeV. A common threshold of $p_{\mathrm{T}} > 7$ GeV is used to veto events with electrons and muons, and no τ-lepton veto is applied.

Figure 6.3 shows the distributions of m_{jj} and $\Delta\eta_{jj}$ in Monte Carlo of the VBF signal and $Z + jets$, $W + jets$ backgrounds. The distributions are shown after the requirements on leading and sub-leading jet p_T and the requirement that the jets be in opposite hemispheres, but before the central jet veto and the requirements on m_{jj}, $\Delta\eta_{jj}$, $\Delta\phi_{jj}$, $\Delta\phi_{j,E_{\mathrm{T}}^{\mathrm{miss}}}$, and $E_{\mathrm{T}}^{\mathrm{miss}}$.

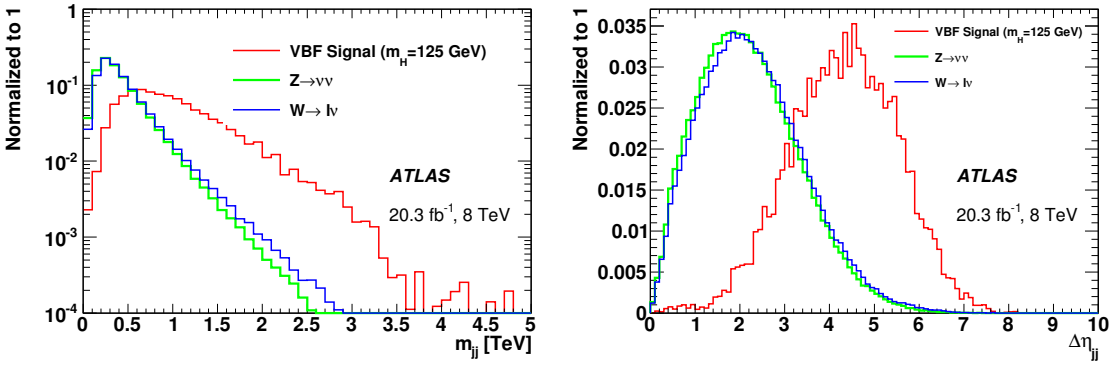

(a) m_{jj} distribution

(b) $\Delta\eta_{jj}$ distribution

Figure 6.3: The distributions of m_{jj} (a) and $\Delta\eta_{jj}$ (b) in Monte Carlo. The plots are normalized to unit area, after the requirements on leading and sub-leading jet p_T and the requirement that the jets be in opposite hemispheres, but before the central jet veto and the requirements on m_{jj}, $\Delta\eta_{jj}$, $\Delta\phi_{jj}$, $\Delta\phi_{j,E_{\mathrm{T}}^{\mathrm{miss}}}$, and $E_{\mathrm{T}}^{\mathrm{miss}}$.

6.3 Background Estimations

The smaller backgrounds of $t\bar{t}$, single top and di-bosons are taken from their MC predictions. In order to reduce the impact of theoretical and experimental uncertainties, and of the statistical uncertainty due to limited numbers of MC events on the multijet, Z+jets and W+jets background estimations, data control regions are used to estimate these backgrounds as described in Section 6.3.1 and Section 6.3.2 respectively. In the case of the multijet background, different data-driven techniques are employed. For the Z+jets and W+jets background expectations, data control regions are constructed to match the signal region selections, differing only in the lepton selection. Indeed, in the signal regions lepton vetoes are imposed, whereas in the Z+jets and W+jets control regions, isolated leptons are required.

The expected and observed yields in these control regions will be inputs for a global fit (see Section 6.5) which uses a maximum likelihood fit to get the final number of events in the respective signal regions.

6.3.1 Data-drive Estimation of the Multijet Background

Multijet events which have no prompt (from the primary interactions) neutrinos can pass the $E_{\mathrm{T}}^{\mathrm{miss}}$ selection due to instrumental effects. Because of the very large rejection from the $E_{\mathrm{T}}^{\mathrm{miss}}$ requirement, it is not practical to simulate this background, so it is estimated using data-driven methods instead.

In the SR2 selections, the multijet background is estimated from data, using a jet smearing method as described in Ref. [96], which relies on the assumption that the $E_{\mathrm{T}}^{\mathrm{miss}}$ of multijet events is dominated by fluctuations in the detector response to jets measured in the data. The estimated multijet background in SR2 is 24 ± 24 events.

In SR1, the multijet background is also estimated from data as follows: an efficiency for each selection requirement is estimated from a control region, then assumed to be applied back to the signal region to obtain the final number of mutijet events. Firstly, a control region is defined where the $\Delta\phi_{j,E_{\mathrm{T}}^{\mathrm{miss}}}$ requirement is inverted, so that the $E_{\mathrm{T}}^{\mathrm{miss}}$ vector is in the direction of a jet in the event. The resulting sample is dominated by multijet events. Secondly, the signal region requirements on the leading and sub-leading jet p_{T} and on the $E_{\mathrm{T}}^{\mathrm{miss}}$ trigger are applied. Then an efficiency of each subsequent kinematic requirement is determined using this sample. Finally the obtained efficiencies are applied to the signal region where there is the nominal $\Delta\phi_{j,E_{\mathrm{T}}^{\mathrm{miss}}}$ requirement.

A systematic uncertainty is assessed based on the accuracy of this assumption in a control region with $|\Delta\eta_{jj}| < 3.8$ and in a control region with three jets (by reverting the requirement of vetoing a third jet in the central region of the detector as mentioned in Section 6.2). Since the inverted $\Delta\phi_{j,E_{\mathrm{T}}^{\mathrm{miss}}}$ requirement-control

region cannot give the efficiency for the $\Delta\phi_{j,E_{\mathrm{T}}^{\mathrm{miss}}}$ selection itself, another multijet-dominated control sample is defined to account for that. It is the region where the $\Delta\phi_{jj}$ requirement is inverted, requiring back-to-back jets in ϕ. Combining all the efficiencies with the observed control region yield gives an estimate of 2 ± 2 for the multijet background.

To validate multijet background estimation in SR1, two signal-depleted neighboring regions are defined by (1) reversing the veto against three-jet events by requiring that the third jet in the event has transverse momentum $p_{\mathrm{T}}^{j3} > 40$ GeV, and (2) requiring both $|\Delta\eta_{jj} < 3.8|$ and $p_{\mathrm{T}}^{j3} > 30$ GeV. Good agreement between expectation and observation is found in these validation regions, as shown in Table 6.2.

Table 6.2: Expected and observed yields for the validation regions in 20.3 fb^{-1} of data. 3-jet: reversal of the veto against three-jet events by requiring $p_{\mathrm{T}}^{j3} > 40$ GeV; and 3-jet and $|\Delta\eta_{jj}| < 3.8$: requirement both $|\Delta\eta_{jj}| < 3.8$ and $p_{\mathrm{T}}^{j3} > 30$ GeV. Contributions from W and Z are normalized to data-driven estimates. The W and Z uncertainties include MC statistics from both the selected region and the corresponding control region, and the number of data events in the control regions. The other numbers are evaluated using Monte Carlo and their uncertainties indicate only statistical uncertainty.

Process	3-jet	3-jet and $\lvert\Delta\eta_{jj}\rvert < 3.8$
ggF Signal	6.2 ± 3.1	-
VBF Signal	19.9 ± 1.4	4.7 ± 0.6
$Z \to \nu\nu$+jets	97.2 ± 10.0	111 ± 10
$W \to \ell\nu$+jets	78.5 ± 6.5	73.2 ± 10.1
Mulijets	19.9 ± 21.8	-
Other Backgrounds	2.2 ± 0.3	0.5 ± 0.1
Total	198 ± 25	185 ± 14
Data	212	195

6.3.2 Estimations of $Z(\to \nu\nu)$+jets and $W(\to \ell\nu)$+jets

The $Z(\to \ell\ell)$+jets and $W(\to \ell\nu)$+jets control regions are defined by the decay products which are di-electron (di-muon), a lepton with a neutrino (considering e and μ) of the respective Z and W bosons. Electrons and muons are required to be isolated. For electrons, the normalized calorimeter isolation energy is required

to be less than 0.28, and the normalized track isolation is required to be less than 0.1. Muons must have a normalized calorimeter isolation less than 0.3 (or < 0.18 if $p_{\mathrm{T}} < 25$ GeV) and a normalized track isolation less than 0.12. Electrons and muons are also required to point back to the primary vertex. The transverse impact parameter significance must be less than 3σ for both electrons and muons, while the longitudinal impact parameter must be $< 0.4(1.0)$ mm for electrons (muons). There are some differences in the selections for the control regions corresponding to SR1 and SR2, so the description below mentions that explicitly when it is applicable.

The $Z(\rightarrow ee/\mu\mu)$+jets control region is defined by selecting events containing two same-flavour, oppositely charged leptons with $p_{\mathrm{T}} > 20$ GeV and $|m_{\ell\ell} - m_Z| < 25$ GeV, where $m_{\ell\ell}$ and m_Z are the di-lepton invariant mass and the Z-boson mass, respectively. Those requirements are asked to make sure that the leptons come from a Z boson decay. In the Z control sample corresponding to SR1 selection, the leading lepton is required to have $p_{\mathrm{T}} > 30$ GeV. Triggers requiring a single electron or muon with $p_{\mathrm{T}} > 24$ GeV are used to select the control samples. The inefficiency of the lepton trigger with respect to offline requirements is negligible in these events. In order to emulate the effect of the offline missing energy selection used in the signal region, the $E_{\mathrm{T}}^{\mathrm{miss}}$ quantity is corrected by adding in vectorially the electron (SR1 and SR2) and muon momentum (SR1 only). All the $Z(\rightarrow ee/\mu\mu)$+jets events are then required to pass the other signal region selections. Backgrounds from processes other than $Z(\rightarrow ee/\mu\mu)$+jets are small in this control region; the contribution from non-Z backgrounds are estimated from MC. For $Z \rightarrow ee$ ($Z \rightarrow \mu\mu$), the non-Z background is at a level of 1.6% (0.9%) of the sample. There is 50% uncertainty (mainly due to limited MC events) on the non-Z background contamination in the Z control region. The observed yield in the SR1 Z control region, shown in Table 6.3, is larger than the expected yield by 16% but is compatible within the combined statistical uncertainties of MC and data. In the SR2 Z control regions, the observed and expected yields differ by 10% as shown in Table 6.4 but are compatible within the total statistical and systematic uncertainties (see Section 6.4). The $E_{\mathrm{T}}^{\mathrm{miss}}$ distributions in the Z control regions are shown in Figs. 6.4 and 6.5 for SR1 and SR2 respectively.

The $W(\rightarrow e\nu/\mu\nu)$+jets control regions are similarly defined by selecting events containing one lepton with transverse momentum $p_{\mathrm{T}} > 30$ GeV (25 GeV) in the case of SR1 (SR2), and no additional leptons with $p_{\mathrm{T}} > 20$ GeV. The $E_{\mathrm{T}}^{\mathrm{miss}}$ is emulated in the same way as for the $Z \rightarrow ee/\mu\mu$ control region and events are required to pass the signal region selections on jets and $E_{\mathrm{T}}^{\mathrm{miss}}$. Different from the Z control regions where other backgrounds are negligible, the W control regions have large background from QCD multijet events which fake leptons (this is different from the QCD multijet events which fake $E_{\mathrm{T}}^{\mathrm{miss}}$ in the signal regions). For SR1, four W control regions are considered using different charge samples for $W^+/W^- \rightarrow e\nu/\mu\nu$ to exploit the charge-asymmetry which presents in $W(\rightarrow \ell\nu)$+jets but in QCD mutijet shown in Table 6.5, whereas in SR2, only two control regions $W(\rightarrow e\nu/\mu\nu)$+jets are used as

Table 6.3: Expected and observed yields for the SR1 $Z(\rightarrow ee/\mu\mu)$+jets control sample in 20.3 fb^{-1} of 2012 data. Expected contributions are evaluated using Monte Carlo, and the uncertainties are statistical only.

	SR1	
Background	$Z(\rightarrow ee)$+jets	$Z(\rightarrow \mu\mu)$+jets
QCD $Z \rightarrow \ell\ell$	10.4 ± 1.5	14.0 ± 1.5
EW $Z \rightarrow \ell\ell$	7.4 ± 0.8	8.2 ± 0.8
Other Backgrounds	0.3 ± 0.2	0.2 ± 0.1
Total	18.1 ± 1.7	22.4 ± 1.7
Data	22	25

Table 6.4: Expected and observed yields for the SR2 $Z(\rightarrow ee/\mu\mu)$+jets control sample in 20.3 fb^{-1} of 2012 data. Expected contributions are evaluated using Monte Carlo, and the uncertainties are statistical only.

	SR2a		SR2b	
Background	$Z(\rightarrow ee)$+jets	$Z(\rightarrow \mu\mu)$+jets	$Z(\rightarrow ee)$+jets	$Z(\rightarrow \mu\mu)$+jets
$Z \rightarrow \ell\ell$	133 ± 4	138 ± 4	44 ± 2	44 ± 2
Other Backgrounds	8 ± 1	10 ± 2	2 ± 1	3± 1
Total	141 ± 4	148 ± 4	44 ± 3	47 ± 2
Data	159	139	33	38

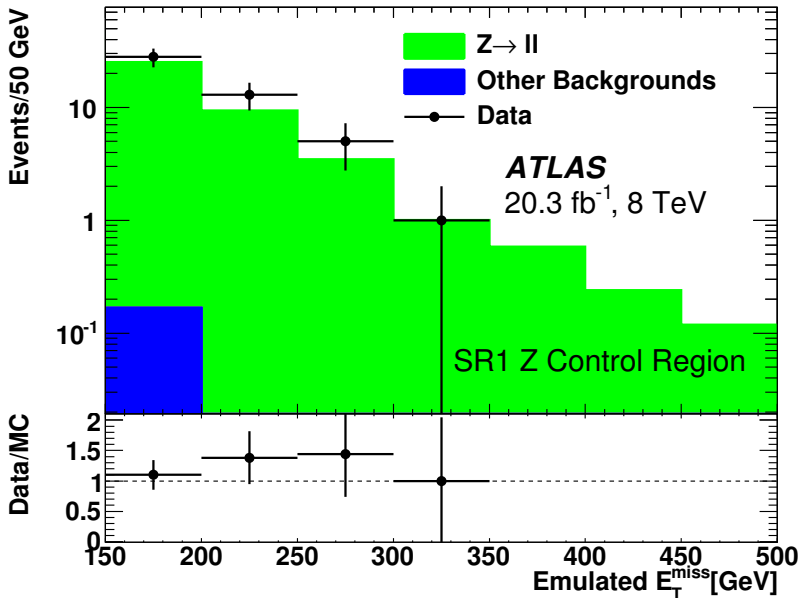

Figure 6.4: Data and MC distributions of the emulated $E_{\mathrm{T}}^{\mathrm{miss}}$ (as described in the text) in the SR1 $Z(\rightarrow ee/\mu\mu)$+jets control region.

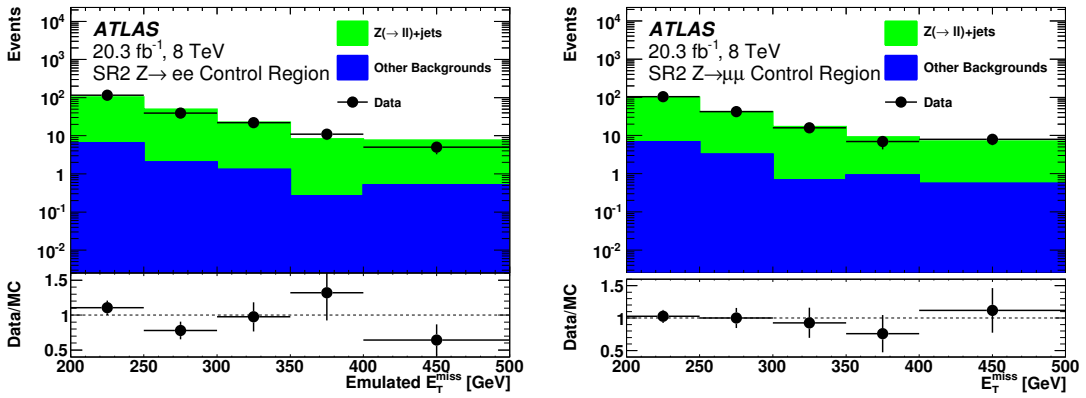

(a) (b)

Figure 6.5: Data and MC distributions of the $E_{\mathrm{T}}^{\mathrm{miss}}$ (as described in the text) in the SR2 Z+jets control regions (a) $Z(\rightarrow ee)$+jets and (b) $Z(\rightarrow \mu\mu)$+jets.

shown in Table 6.6.

Table 6.5: Expected and observed yields for the SR1 $W \to \ell\nu$ control sample, after all requirements in 20.3 fb^{-1} of 2012 data. The multijet background is estimated using the data-driven method described in the text; all other contributions are evaluated using Monte Carlo. Only the statistical uncertainties are shown.

	SR1			
Background	$W^+ \to e\nu$	$W^- \to e\nu$	$W^+ \to \mu\nu$	$W^- \to \mu\nu$
$Z \to \ell\ell$	5.87 ± 0.68	7.33 ± 0.96	9.11 ± 1.14	8.25 ± 0.93
QCD W	92.3 ± 7.2	55.1 ± 5.3	85.5 ± 7.0	43.8 ± 4.55
EW W	99.4 ± 4.0	52.5 ± 2.9	81.9 ± 3.7	39.1 ± 2.53
Multijet	28.0 ± 6.8	28.0 ± 6.8	1.61 ± 2.55	1.61 ± 2.55
Other	4.02 ± 0.73	1.80 ± 0.43	3.23 ± 0.69	0.96 ± 0.32
Total	230 ± 11	145 ± 9	181 ± 8.41	93.7 ± 5.88
Data	225	141	182	98

Table 6.6: Expected and observed yields for the SR2 $W(\to e\nu/\mu\nu)$+jets control sample in 20.3 fb^{-1} of 2012 data. Expected contributions are evaluated using Monte Carlo, and the uncertainties are statistical only.

	SR2a		SR2b	
Background	$W(\to e\nu)$+jets	$W(\to \mu\nu)$+jets	$W(\to e\nu)$+jets	$W(\to \mu\nu)$+jets
$W \to \ell\nu$	743 ± 13	1120 ± 16	243 ± 6	385 ± 8
$Z \to \ell\ell$	6 ± 1	25 ± 2	2 ± 0	7 ± 1
Multijet	13 ± 3	0 ± 0	3 ± 1	0 ± 0
Other	44 ± 4	78 ± 7	13 ± 2	19 ± 3
Total	806 ± 14	1223 ± 17	261 ± 6	411 ± 9
Data	783	1209	224	295

In the $W(\to e\nu/\mu\nu)$+jets control regions corresponding to the SR1 selection, a

fit to the transverse mass

$$m_{\mathrm{T}} = \sqrt{2p_T^{\ell} E_{\mathrm{T}}^{\mathrm{miss}} \left[1 - \cos(\Delta\phi_{\ell, E_{\mathrm{T}}^{\mathrm{miss}}})\right]}$$

of the lepton and $E_{\mathrm{T}}^{\mathrm{miss}}$ is used to estimate the multijet background. No requirements are made on $E_{\mathrm{T}}^{\mathrm{miss}}$ and m_{T} in order to obtain an explicit measurement and uncertainty for the background from multijets. Because the multijet background does not have a prompt neutrino, the $E_{\mathrm{T}}^{\mathrm{miss}}$ tends to be lower and to point in the direction of the jet that has been misidentified as a lepton. As a results, the multijet background tends to have significantly lower m_{T} than the W+jets contribution. Control samples modeling the jets misidentified as leptons in multijet events are constructed by selecting events that pass all the W+jets control region selection, except for certain lepton identification criteria: for electrons, some of the EM calorimeter shower shape requirements are loosened and fully identified electrons are removed, while for muons, the transverse impact parameter (d_0) requirement which suppresses muons originating from heavy flavour jets is reversed. To obtain the normalization of the multijet background in the W+jets control region, templates of the m_{T} distribution for processes with prompt leptons are taken from Monte Carlo. Shape templates for the backgrounds from multijet events are constructed by summing the observed yields in control samples obtained by inverting the lepton identification and d_0 requirements, and subtracting the expected contributions from W+jets and Z+jets events using MC. Since the misidentified-jet samples are expected to be charge-symmetric, the same shape template and normalization factor is used to model both charge categories of a given lepton flavour (e or μ). To determine the $W(\to \ell\nu)$+jets background normalization, a fit to the transverse mass m_{T} of the lepton and $E_{\mathrm{T}}^{\mathrm{miss}}$ is used. The $W(\to \ell\nu)$+jets contribution, however, is not charge-symmetric, so the different charge samples are kept separate in the simultaneous fit to four m_{T} distributions, one for each lepton flavour and charge combination shown in Fig. 6.6. There are three free normalizations in the fit: one for events with a prompt lepton, one for events where a jet is misidentified as an electron, and one for events where a jet is misidentified as a muon. The normalization factor for the prompt leptons in the m_{T} fit is 0.95 ± 0.05 (stat).

In the $W \to \ell\nu$ control regions corresponding to the SR2 selections, the background from multijet events, where a jet has been misidentified as a lepton and the measured $E_{\mathrm{T}}^{\mathrm{miss}}$ is not due to a prompt neutrino, is rejected by requiring that the uncorrected $E_{\mathrm{T}}^{\mathrm{miss}}$ be larger than 25 GeV and that the transverse mass be in the range $40 < m_{\mathrm{T}} < 100$ GeV. For the $W \to \mu\nu$ control region, an attempt is made to estimate residual multijet background using a control sample with inverted muon isolation. The residual background from multijet events is negligible, lower than the uncertainty on the final estimate. In the case of the $W \to e\nu$ control region, the tight control region-specific requirements (tight electron isolation and $E_{\mathrm{T}}^{\mathrm{miss}}$ requirements) largely reduces the multijet background relative to the other backgrounds. The residual multijet background in the $W \to e\nu$ control region is at the level of

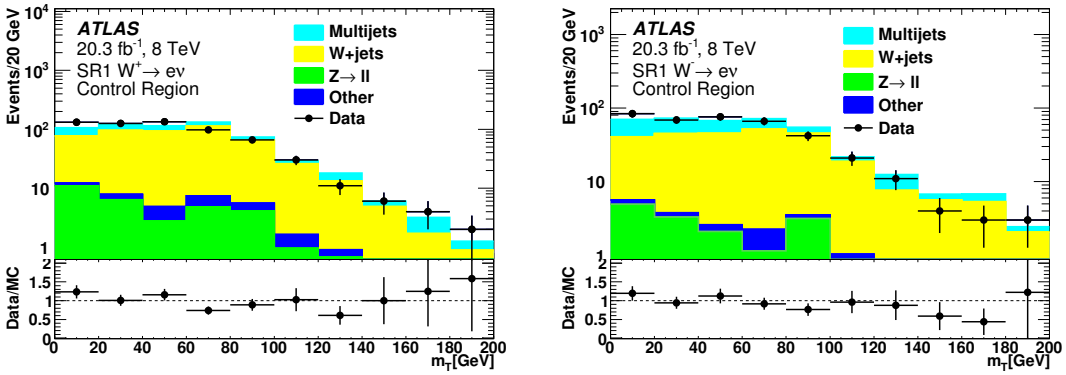

(a)

(b)

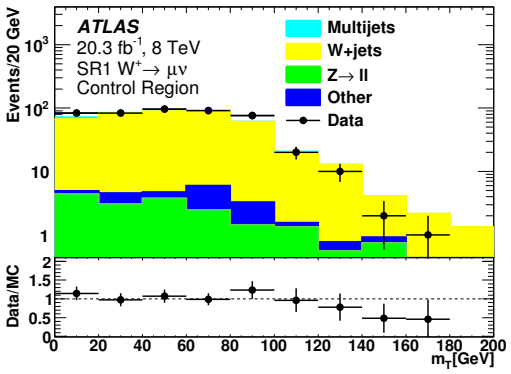

(c)

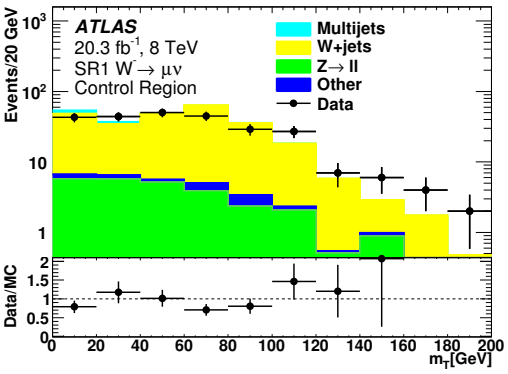

(d)

Figure 6.6: The transverse mass distributions used in the SR1 W+jets control region after all requirements except for the $E_T^{miss} > 150$ GeV requirement: (a) the $W^+ \to e^+\nu$, (b) $W^- \to e^-\nu$, (c) $W^+ \to \mu^+\nu$ and (d) $W^- \to \mu^-\nu$.

1% of the total control region background, with an uncertainty of 100%. Figure 6.7 shows the m_{T} distributions in the SR2 W+jets control region.

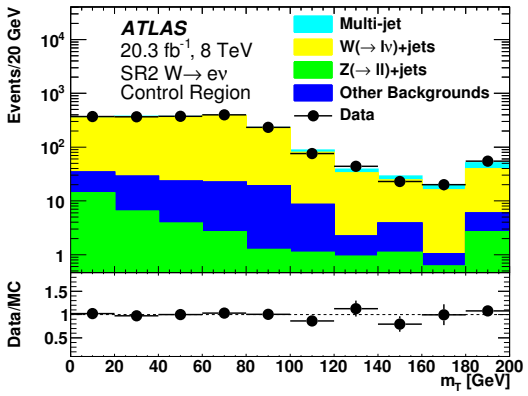

(a)

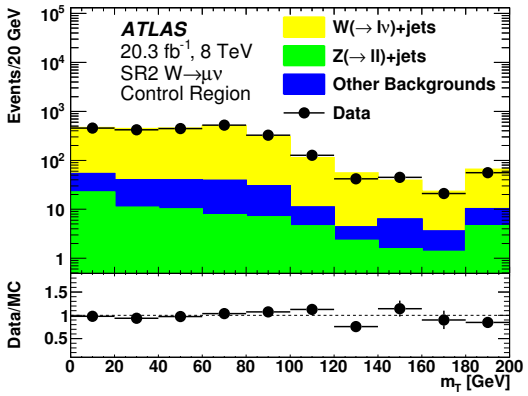

(b)

Figure 6.7: The transverse mass distributions in the SR2 W+jets control region after all requirements: (a) the $W \to e\nu$ and (b) $W \to \mu\nu$.

Table 6.2 shows the validation of Z+jets and W+jets background estimations for SR1 in two signal-depleted neighboring regions of phase space described in Section 6.3.1.

6.4 Systematic Uncertainties

There are different sources of systematics uncertainties which affect the determinations of backgrounds and signals events. They come from theoretical calculation for the cross sections or describing kinematically the events for different processes as well as the experimental systematics which affect the calibration or reconstruction efficiencies of physics objects. The considered uncertainties are described in details below.

The experimental uncertainties on the Monte Carlo prediction for signal and background are dominated by uncertainties in the jet energy scale (JES) and resolution (JER) [60]. This includes effects such as the η dependence of the energy scale calibration and the dependence of the energy response on the jet flavour and event flavour composition, where flavour refers to the originating gluon or light quark. Uncertainties related to the lepton identification in the control regions and lepton vetoes are negligible. Luminosity uncertainties [97] are applied to the signal and background yields that are obtained from MC.

Theoretical uncertainties on the W+jets and Z+jets contributions to both the signal and control regions are assessed using SHERPA, and cross-checked with MCFM [94] and VBFNLO [83] for the EW and QCD processes respectively, and by a comparison between SHERPA and ALPGEN [98] for the latter process. In all cases, the uncertainties are determined by independently varying the factorization and renormalization scales by factors of 2 and 1/2, keeping their ratio within 0.5-2.0. The parton distribution function uncertainties are evaluated with the CT10 error sets [99]. The uncertainty on the ggF yield due to the jet selection is evaluated using the Stewart-Tackmann method [100]. Uncertainty in the p_{T} distribution of the Higgs boson in ggF is evaluated with the re-summation improved the Stewart-Tackmann method, after re-weighting the p_{T} distribution as mentioned in Chapter 1. Electroweak radiative corrections to the VBF signal yield are estimated using HAWK. To assess the level of theoretical uncertainty on the jet veto, we measure the variation in the predicted VBF cross section with respect to shifts in the renormalization and factorization scales as well as with respect to parton-shower using POWHEG-BOX NLO generator matched to PYTHIA and to HERWIG. The effect of the parton shower on the QCD W+jets and Z+jets background estimations is obtained by comparing simulated samples with different parton shower models. As shown in Table 6.7, where the main systematic uncertainties are summarized, using the MC predictions of $Z_{\mathrm{SR}}/W_{\mathrm{CR}}$ and $W_{\mathrm{SR}}/W_{\mathrm{CR}}$ ratios reduces the systematics uncertainties in the final Z+jets and W+jets background estimates. We checked the $Z(\to \ell\ell)$+jets/$W(\to \ell\nu)$+jets ratio in data and MC, and no discrepancy larger than 10% was observed, consistent with the residual theory uncertainties on the $Z_{\mathrm{SR}}/W_{\mathrm{CR}}$ shown in Table 6.7.

Table 6.7: Detector and theory uncertainties (%) after all SR or CR selections. For each source of uncertainty, where relevant, the first and second rows correspond to the uncertainties in SR1 and SR2 respectively. The ranges of uncertainties in the Z or W column correspond to uncertainties in the Z+jets and W+jets MC yields in the SR or CR. The search uses the uncertainties in the ratios of SR to CR yields shown in the last column.

Uncertainty	VBF	ggF	Z or W	$Z_{\mathrm{SR}}/W_{\mathrm{CR}}$ or $W_{\mathrm{SR}}/W_{\mathrm{CR}}$
JES	16	43	17–33	3–5
	9	12	0–11	1–4
JER	Negligible	Negligible	Negligible	Negligible
	3.1	3.2	0.2–7.6	0.5–5.8
Luminosity	2.8	2.8	2.8	Irrelevant
QCD scale	0.2	7.8	5–36	7.8–12.1
			7.5–21	1–2
PDF	2.3	7.5	3–5	1–2
	2.8		0.1-2.6	
Parton shower	4.4	41	9–10	5
Veto on third jet		29	Negligible	Negligible
Higgs boson p_{T}	Negligible	9.7	Irrelevant	Irrelevant
MC statistics	2	46	2.3–6.4	3.3–6.6
	0.6	13	0.8–4.5	

6.5 Results

Figures 6.8 and 6.9 show the $E_{\mathrm{T}}^{\mathrm{miss}}$ and the m_{jj} distributions after imposing the requirements of SR1 and SR2 respectively. There is good agreement between the data and the background expectations from the SM, and no statistically significant excess is observed in data. The limit on the branching fraction of $H \to$ invisible

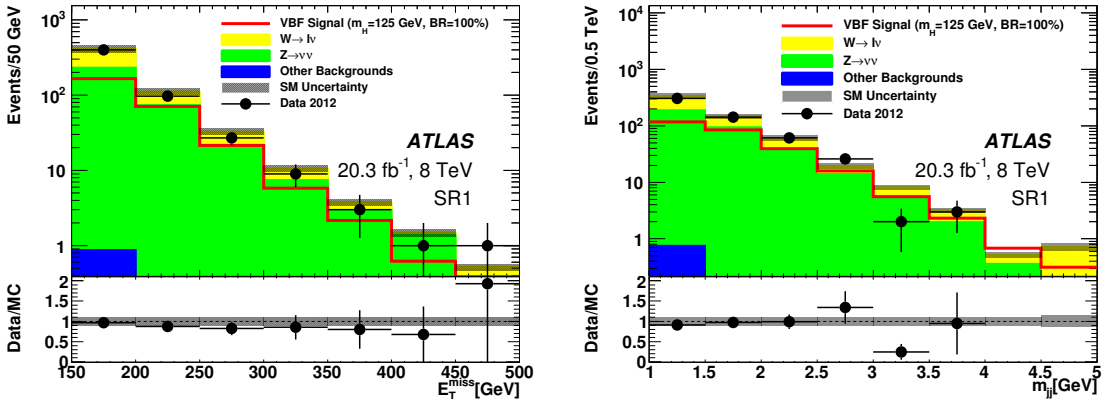

(a) $E_{\mathrm{T}}^{\mathrm{miss}}$ distribution

(b) m_{jj} distribution

Figure 6.8: Data and MC distributions after all the requirements in SR1 for (a) $E_{\mathrm{T}}^{\mathrm{miss}}$ and (b) the dijet invariant mass m_{jj}. The background histograms are normalized to the values in Table 6.8. The VBF signal (red histogram) is normalized to the SM VBF Higgs boson production cross section with BF($H \to$ invisible) = 100%.

is computed using a maximum-likelihood fit to the yields in the signal regions and the $W(\to e\nu/\mu\nu)$+jets and $Z(\to ee/\mu\mu)$+jets control regions following the CL_S modified frequentist formalism [101] with a profile likelihood-ratio test statistic [23]. Expected signal and background probability distributions in the signal and control regions are determined from MC predictions, with the exception of the multijet backgrounds, which use the data-driven methods described in Section 6.3. Systematic uncertainties are parameterized as Gaussian constrained nuisance parameters. The nuisance parameter for each individual source of uncertainty is shared among the expected yields so that its correlated effect is taken into account. The relative weight of the $Z(\to ee/\mu\mu)$+jets and $W(\to e\nu/\mu\nu)$+jets in the control regions is determined by the maximization of the likelihood function.

One global likelihood function including all three signal regions and the six corresponding control regions is constructed with only the signal yields and correlated uncertainties coupling the search regions. The theoretical uncertainties are taken to be uncorrelated between the EW and QCD processes and uncorrelated with the scale uncertainty on the signal. The uncertainties which are treated as correlated between the regions are:

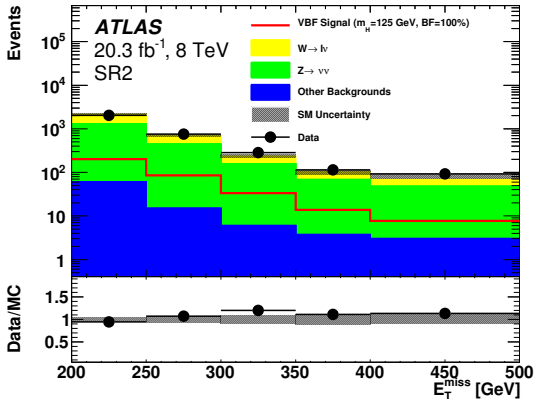

(a) $E_{\mathrm{T}}^{\mathrm{miss}}$ distribution

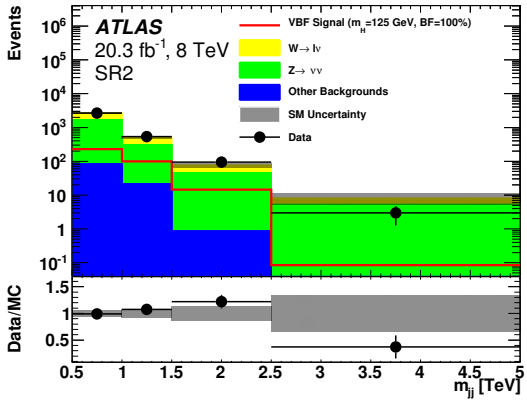

(b) m_{jj} distribution

Figure 6.9: Data and MC distributions after all the requirements in SR2 for (a) $E_{\mathrm{T}}^{\mathrm{miss}}$ and (b) the dijet invariant mass m_{jj}. The background histograms are normalized to the values in Table 6.8. The VBF signal is normalized to the SM VBF Higgs boson production cross section with BF($H \rightarrow$ invisible) = 100%.

- Uncertainty in the luminosity measurements. This impacts the predicted rates of the signals and the backgrounds that are estimated using MC simulation, namely ggF and VBF signals, and $t\bar{t}$, single top, and diboson backgrounds.
- Uncertainties in the absolute scale and resolution of the reconstructed jet energy.
- Uncertainties in the modelling of the parton shower.
- Uncertainties in renormalization and factorization scales.

The global likelihood can be summarized as

$$\begin{aligned}\mathcal{L} = \{\Pi_c\, \Pi_r\ P(\, N_{c,r}\ &|\, \mu \left(S_{c,r}^{VBF}\, \Pi_s(1+\alpha_s \Delta S_{c,r,s}^{VBF}) + S_{c,r}^{ggH}\, \Pi_s(1+\alpha_s \Delta S_{c,r,s}^{ggH})\right) \\ &+ k_c \left(W_{c,r}\, \Pi_s(1+\alpha_s \Delta W_{c,r,s}) + Z_{c,r}\, \Pi_s(1+\alpha_s \Delta Z_{c,r,s})\right) \\ &+ M_{c,r}\, \Pi_s(1+\alpha_s \Delta M_{c,r,s}) + O_{c,r}\, \Pi_s(1+\alpha_s \Delta O_{c,r,s})\ )\} \times \{\Pi_s e^{-\alpha_s^2}\}\end{aligned} \tag{6.1}$$

where the indices are: c is the category including the SR1, SR2a, SR2b, r is the signal or control region (SR, WCR, or ZCR), and s is a systematic. The first term enclosed by curly braces is the Poisson probability of the observed yields for a category and region combination $N_{c,r}$ given the expectations. Here $P(N_{c,r}|X)$ indicates the Poisson probability of observed $N_{c,r}$ events where X are expected. The second term implements the Gaussian constrains on the systematics uncertainties. Floating in the fit are the signal yield normalized to 100% branching fraction μ, the W+jets

and Z+jets normalization factors k_c, and all the systematic uncertainty nuisance parameters α_s. The nominal yields in each combination of category and region are $S_{c,r}^{VBF}$ and $S_{c,r}^{VBF}$ for the signal (assuming 100% BR), $W_{c,r}$ for the W+jets, $Z_{c,r}$ for the Z+jets, $M_{c,r}$ for the multijet background, and $O_{c,r}$ for the other backgrounds. The impact of a systematic on the expected yield from a process in a region is written with the Δ symbols; for example, $\Delta W_{c,r,s}$ is the effect of systematic s on the expected contribution from the W+jets process in the region r of the c category search.

This likelihood only couples the signal yield and the correlated systematic uncertainties between the searches. The W+jets and Z+jets normalization factors k_c should only minimally be affected by the combination of channels through the signal and the correlated systematic uncertainties.

Table 6.8 shows signal, background and data events after the global fit including the effects of systematic uncertainties, MC statistical uncertainties in the control and signal regions, and the data statistical uncertainties in the control regions. The post-fit values of the Z+jets and W+jets background normalization scale factors k_c, discussed in Section 6.3, are 0.95 ± 0.21, 0.87 ± 0.17 and 0.74 ± 0.12 for SR1, SR2a and SR2b and their control regions, respectively. As shown in Table 6.8, the signal-to-background ratio is 0.5 in SR1, and 0.06 and 0.18 in SR2a and SR2b respectively, for BF($H \rightarrow$ invisible) = 100%. Fits to the likelihood function are performed separately for each signal region and their combination, and the 95% CL limits on BF($H \rightarrow$ invisible) are shown in Table 7.1.

There are validation plots (Figures 6.10, 6.12, 6.11) for the fitting procedure done in this analysis. They provide the information that there are no weird constraints on the nuisance parameters and the fit is stable.

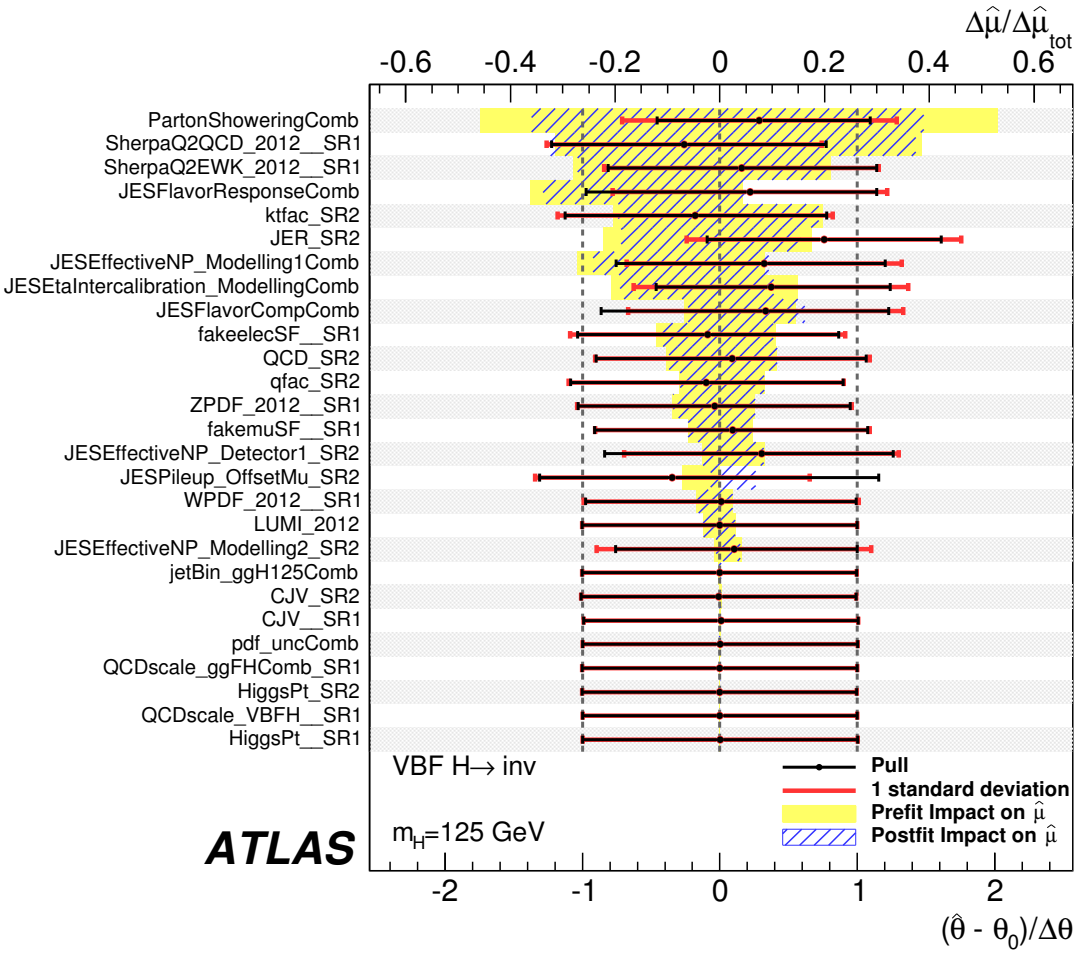

Figure 6.10: Ranking and the pull distributions of the nuisance parameters used in the fit for the VBF analysis.

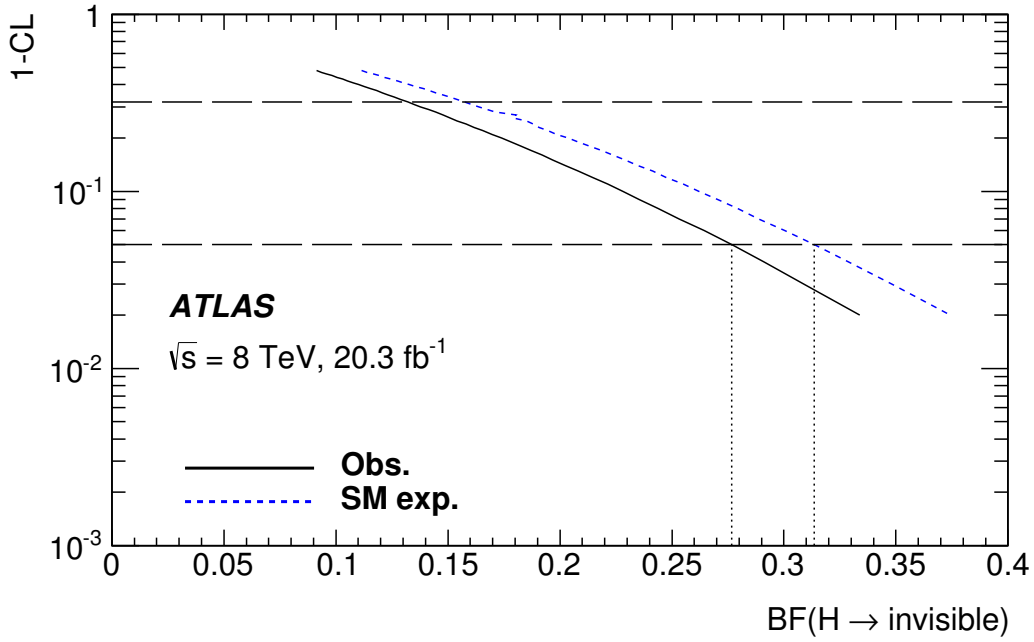

Figure 6.11: The $(1 - \mathrm{CL})$ versus BR($h \to$ invisible) scan for the search for VBF to invisible Higgs boson decays. The horizontal dashed lines refer to the 68% and 95% confidence levels. The vertical dashed lines indicate the observed and expected upper bounds at the 95% CL on BR($h \to$ invisible).

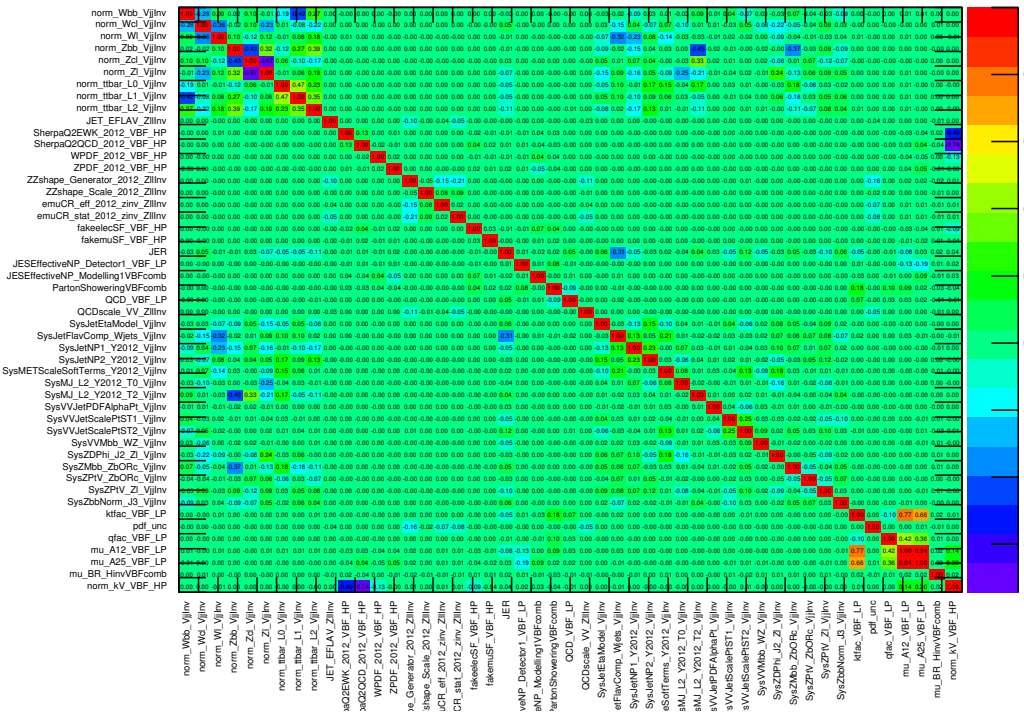

Figure 6.12: The correlations among the nuisance parameters and normalization factors in the fit performed in the search for VBF to invisible Higgs boson decays.

Table 6.8: Estimates of the expected yields and their total uncertainties for SR1 and SR2 in 20.3 fb^{-1} of 2012 data. The $Z(\to \nu\nu)$+jets, $W(\to \ell\nu)$+jets, and multijet background estimates are data-driven. The other backgrounds and the ggF and VBF signals are determined from MC simulation. The expected signal yields are shown for $m_H = 125$ GeV and are normalized to BF($H \to$ invisible) = 100%. The W+jets and Z+jets statistical uncertainties result from the number of MC events in each signal and corresponding control region, and from the number of data events in the control region.

Signal region	SR1	SR2a	SR2b
Process			
ggF signal	20± 15	58± 22	19± 8
VBF signal	286± 57	182± 19	105±15
$Z(\to \nu\nu)$+jets	339± 37	1580± 90	335±23
$W(\to \ell\nu)$+jets	235± 42	1010± 50	225±16
Multijet	2± 2	20± 20	4± 4
Other backgrounds	1±0.4	64± 9	19± 6
Total background	577± 62	2680±130	583±34
Data	539	2654	636

Table 6.9: Summary of limits on BF($H \to$ invisible) for 20.3 fb^{-1} of 8 TeV data in the individual search regions and their combination, assuming the SM cross section for $m_H = 125$ GeV.

Results	Expected	$+1\sigma$	-1σ	$+2\sigma$	-2σ	Observed
SR1	0.35	0.49	0.25	0.67	0.19	0.30
SR2	0.60	0.85	0.43	1.18	0.32	0.83
Combined Results	0.31	0.44	0.23	0.60	0.17	0.28

6.6 Model Independent limits

The agreement between the data and the background expectations in SR1 is also expressed as a model-independent 95% CL upper limit on the fiducial cross section

$$\sigma_{\text{fid}} = \sigma \times \text{BF} \times \mathcal{A}, \tag{6.2}$$

$$= \frac{N}{\mathcal{L} \times \epsilon}, \tag{6.3}$$

where the acceptance $\mathcal{A}$ is the fraction of events within the fiducial phase space defined at the MC truth level using the SR1 selections in Section 6.2, N the accepted number of events, $\mathcal{L}$ the integrated luminosity and ϵ the selection efficiency defined as the ratio of selected events to those in the fiducial phase space. Only the systematic uncertainties on the backgrounds and the integrated luminosity are taken into account in the upper limit on σ_{fid}, shown in Table 6.10. In SR1, the acceptance

Table 6.10: Model-independent 95% CL upper limit on the fiducial cross section for non-SM processes σ_{fid} in SR1.

SR1	Expected	$+1\sigma$	-1σ	$+2\sigma$	-2σ	Observed
Fiducial cross section [fb]	4.78	6.32	3.51	8.43	2.53	3.93

and the event selection efficiency, estimated from simulated VBF $H \to ZZ \to 4\nu$ events, are $(0.89 \pm 0.04)\%$ and $(94 \pm 15)\%$ respectively. The uncertainties have been divided such that the theory uncertainties are assigned to the acceptance and the experiment uncertainties are assigned to the efficiency.

Chapter 7

Combined limit on Higgs Boson Invisible Decays

This chapter presents the determination of the Higgs boson invisible branching ratio using direct searches for Higgs boson decays to invisible particles in events with dileptons or dijets with large missing transverse momentum, $E_{\mathrm{T}}^{\mathrm{miss}}$. These inputs include the search for a Higgs boson, produced through VBF and thus accompanied by dijets, that decays invisibly and results in missing transverse momentum (VBF $\rightarrow jj + E_{\mathrm{T}}^{\mathrm{miss}}$) [11]; the search for a Higgs boson, which subsequently decays invisibly, produced in association with a Z boson that decays to dileptons ($ZH \rightarrow \ell\ell + E_{\mathrm{T}}^{\mathrm{miss}}$ [15]); and the search for a Higgs boson, which afterwards decays invisibly, produced together with a W or Z boson that decays hadronically ($W/ZH \rightarrow jj + E_{\mathrm{T}}^{\mathrm{miss}}$ [16]). Each search channel is designed to be mostly sensitive to the product of a Higgs boson production cross section and decay branching ratio. They classify candidate events into exclusive categories based on the expected kinematics of different Higgs boson production processes. This allows both to improve the sensitivity as well as to enable discrimination between different Higgs boson production modes. These searches are based on up to 4.8 fb^{-1} of pp collision data at $\sqrt{s} = 7$ TeV and up to 20.3 fb^{-1} at $\sqrt{s} = 8$ TeV. This analysis is inside a bigger project "Constraints on New Phenomena via Higgs Boson Couplings and Invisible Decays with the ATLAS Detector" [12].

The analysis procedure is described in Section 7.1, the combination of direct searches for invisible Higgs boson decays is discussed in Section 7.2, the interpretation in Higgs-portal dark matter scenario is expressed in Section 7.3. My main contribution for this analysis: providing the result limit and validation of the fitting methods.

7.1 Analysis Procedure

The statistical treatment of the data is described in Refs. [102–106]. Confidence intervals use the test statistic $t_{\boldsymbol{\alpha}} = -2\ln\Lambda(\boldsymbol{\alpha})$, which is based on the profile likelihood ratio [107]:

$$\Lambda(\boldsymbol{\alpha}) = \frac{L\big(\boldsymbol{\alpha}\,,\,\hat{\hat{\boldsymbol{\theta}}}(\boldsymbol{\alpha})\big)}{L(\hat{\boldsymbol{\alpha}},\hat{\boldsymbol{\theta}})} \quad . \tag{7.1}$$

The likelihood in Eq. 7.1 depends on one or more parameters of interest $\boldsymbol{\alpha}$, such as the Higgs boson production times branching ratio strength μ. Systematic uncertainties and their correlations [102] are modelled by introducing nuisance parameters $\boldsymbol{\theta}$. The treatment of systematic uncertainties is the same as that used in the Higgs boson coupling measurements [108]. The single circumflex in the denominator of Eq. 7.1 denotes the unconditional maximum likelihood estimate of a parameter. The double circumflex in the numerator denotes the "profiled" value, namely the conditional maximum likelihood estimate for given fixed values of the parameters of interest $\boldsymbol{\alpha}$.

For each production mode j and the invisible decay mode, μ is the production cross section times invisible branching ratio normalized to the total SM rate for the production mode in question, then the SM is recovered at $\mu = 0$:

$$\mu = \frac{\sigma_j}{\sigma_{j,SM}} \times \mathrm{BR}_{\mathrm{inv}} \quad . \tag{7.2}$$

The parameters of interest characterise each particular scenario studied-Higgs boson invisible branching ratio $\mathrm{BR}_{\mathrm{inv}}$ for the studies of Higgs boson invisible decays (Section 7.2).

It is assumed that there are no new production modes beyond the SM ones; however, the possibility of new decay modes is left open. The couplings associated with Higgs boson production and decays through loops are not resolved, but rather left as effective couplings.

In the combination of direct searches for invisible Higgs boson decays, confidence intervals in $\mathrm{BR}_{\mathrm{inv}}$ are defined using the CL_S procedure [109] in order to be consistent with the convention used in those individual searches. The limit obtained with the CL_S method is consistent to two significant figures with the limit based on the log likelihood ratio.

7.2 Direct Searches for Invisible Decays

In the SM, the process $H \to ZZ \to 4\nu$ is an invisible decay of the Higgs boson, but the branching ratio is 1.2×10^{-3} [46], which is small compared to the sensitivities of the aforementioned direct searches. In direct searches, no excess of events has been found and upper bounds have been set on the Higgs boson production cross section times the $H \to$ invisible branching ratio. Assuming that the Higgs boson production cross sections are unchanged relative to the SM expectations, upper bounds on the branching ratio of invisible Higgs boson decays have been obtained from the $\sigma \times$ BR measurements [15, 16, 110].

A statistical combination of the following direct searches for invisible Higgs boson decays is performed:

(1) The Higgs boson is produced in the VBF process and decays invisibly [110]. The signature of this process is two jets with a large separation in pseudo-rapidity, forming a large invariant dijet mass, together with large $E_{\mathrm{T}}^{\mathrm{miss}}$.

(2) The Higgs boson is produced in association with a Z-boson, where $Z \to \ell\ell$ and the Higgs boson decays to invisible particles [15]. The signature in this search is two opposite-sign and same-flavor leptons (electrons or muons) with large missing transverse momentum.

(3) The Higgs boson is produced in association with a vector boson V (W or Z), where $V \to jj$ and the Higgs boson decays to invisible particles [16]. The signature in this search is two jets whose invariant mass m_{jj} is consistent with the V mass, together with large missing transverse momentum.

The ATLAS and CMS Collaborations have set upper limits at the 95% CL of 26% [110] and 57% [53] respectively on the branching ratio for invisible Higgs decays by searching for vector boson fusion production of a Higgs boson that decays invisibly. Using the $ZH \to \ell\ell + E_{\mathrm{T}}^{\mathrm{miss}}$ signature, weaker bounds were obtained by both ATLAS and CMS, giving upper limits of 75% [15] and 83% [14], respectively. By combining the searches in $Z(\ell\ell)H$ and $Z(b\bar{b})H$, CMS obtained an upper limit of 81% [14]. A combination of the searched in VBF and ZH was carried out by CMS, giving a combined upper limit of 47% [53]. Using the associated production with a vector boson, VH, where $V = W$ or Z, $V \to jj$, and $H \to$ invisible, ATLAS has set an upper bound of 78% [16]. Other searches for invisible Higgs decays in events with large $E_{\mathrm{T}}^{\mathrm{miss}}$ in association with one or more jets have also been performed [17, 18, 20, 111], but these searches are less sensitive to Higgs-mediated interactions.

To combine the measurements, the searches need to be performed in non-overlapping regions of phase space or the combination must account for the overlap in phase space. The $ZH \to \ell\ell + E_{\mathrm{T}}^{\mathrm{miss}}$ search does not overlap with the other searches for $H \to E_{\mathrm{T}}^{\mathrm{miss}}$ since a veto on events containing jets was required. The overlap due to possible inefficiency in the veto requirements is negligible. The VBF $\to jj + E_{\mathrm{T}}^{\mathrm{miss}}$

and the $W/ZH \to jj + E_{\mathrm{T}}^{\mathrm{miss}}$ searches also do not overlap in their phase spaces since the former requires a large dijet invariant mass (above $m_{jj} > 500$ GeV) and latter imposes the requirement that the dijet invariant mass must be consistent with the associated vector boson mass within $50 < m_{jj} < 100$ GeV and imposes a veto on forward jets. The same overlap removal requirements were applied in data to both signal and control regions in the various searches, making the control regions used for background estimation non-overlapping.

The following nuisance parameters are treated as being fully correlated across the individual searches, with the rest being uncorrelated:

- Uncertainty in the luminosity measurements. This impacts the predicted rates of the signals and the backgrounds that are estimated using Monte Carlo simulation, namely ggF, VBF, and Vh signals, and $t\bar{t}$, single top, and diboson backgrounds.

- Uncertainties in the absolute scale of the jet energy calibration and on the resolution of the jet energy calibration.

- Uncertainties in the modeling of the parton shower.

- Uncertainties in renormalization and factorization scales, as well as parton distribution functions. This affects the expected numbers of signal events in the ggF, VBF and VH production channels.

The uncertainty in the soft component of the missing transverse momentum has a significant impact in the $W/ZH \to jj + E_{\mathrm{T}}^{\mathrm{miss}}$ channel. Its impact is much smaller in the other searches and not included as a nuisance parameter. This uncertainty is therefore not correlated across all the searches.

Assuming the SM production cross sections of the Higgs boson, the limit on the branching ratio of $H \to$ invisible, defined in Eq. 7.2, is computed using a maximum likelihood fit to the event counts in the signal regions and the data control samples following the CL_s modified frequentist formalism with a profile likelihood test statistic [107]. Expected event counts for the signals, backgrounds and control regions are taken from Monte Carlo predictions. Systematic uncertainties are included as Gaussian-constrained nuisance parameters, centered at their nominal values with the widths of one-sigma deviations. The nuisance parameters for each individual source of uncertainty are applied on the relevant expected number of events so that the correlated effects of the uncertainties are taken into account.

Table 7.1 summarizes the results of the limits from direct searches for invisible Higgs boson decays and their combination. Figure 7.1 shows the CL_S scan as a function of $\mathrm{BR}(H \to \text{invisible})$ for the combination of direct searches for invisible Higgs boson decays.

There are validation plots (Figures 7.2, 7.3) for the fitting procedure done in this analysis. They provide the information that there are no weird constraints on the nuisance parameters and the fit is stable.

BR($H \to$ inv.) at the 95% CL	Obs.	-2σ	-1σ	Exp.	$+1\sigma$	$+2\sigma$
VBF H	0.28	0.17	0.23	0.31	0.44	0.60
$Z(\to \ell\ell)H$	0.75	0.33	0.45	0.62	0.86	1.19
$V(\to jj)H$	0.78	0.46	0.62	0.86	1.19	1.60
Combined Results	0.25	0.14	0.19	0.27	0.37	0.50

Table 7.1: Summary of upper bounds on BR($H \to$ invisible) at the 95% CL for the Run 1 data in the individual searches and their combination. The Higgs boson production rates via VBF and VH associated production are assumed to be equal to their SM values. The numerical bounds larger than 1 can be interpreted as an upper bound on σ/σ_{SM}, where σ_{SM} is the Higgs boson production cross section in the Standard Model.

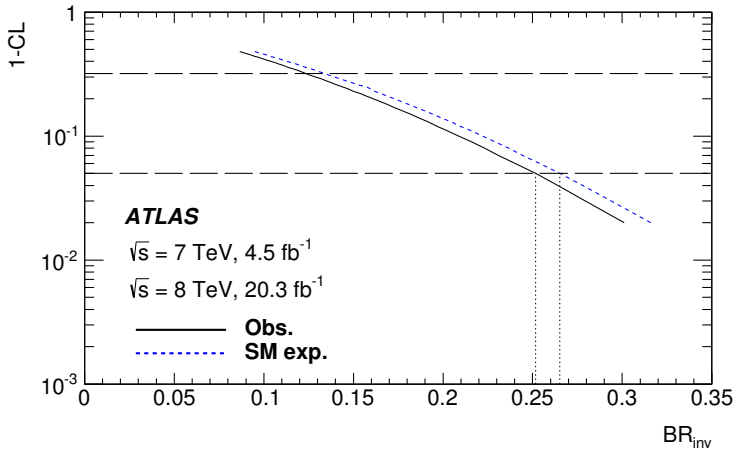

Figure 7.1: The $(1 - \mathrm{CL})$ versus BR($h \to$ invisible) scan for the combined search for invisible Higgs boson decays. The horizontal dashed lines refer to the 68% and 95% confidence levels. The vertical dashed lines indicate the observed and expected upper bounds at the 95% CL on BR($h \to$ invisible) for the combined search.

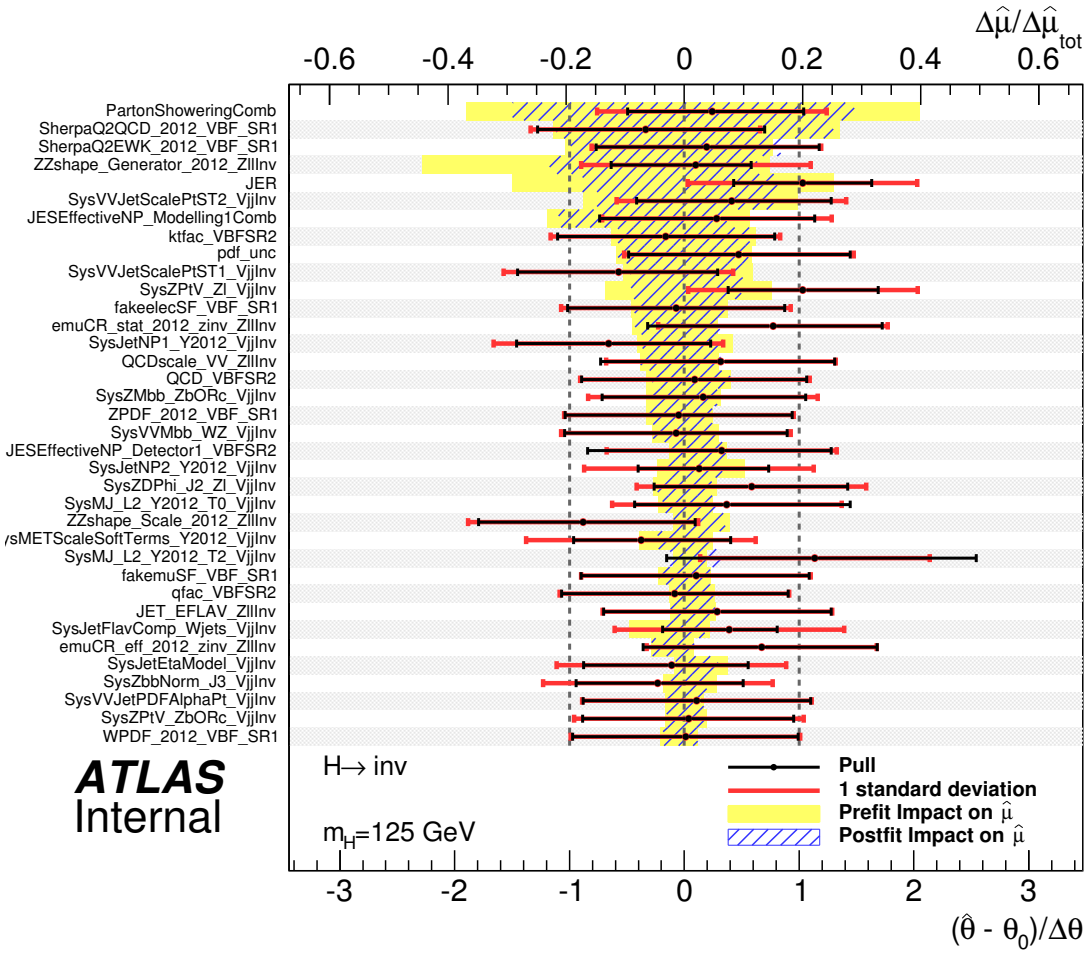

Figure 7.2: Ranking and the pull distributions of the nuisance parameters used in the fit for the analysis of combination all the Higgs to invisible channels.

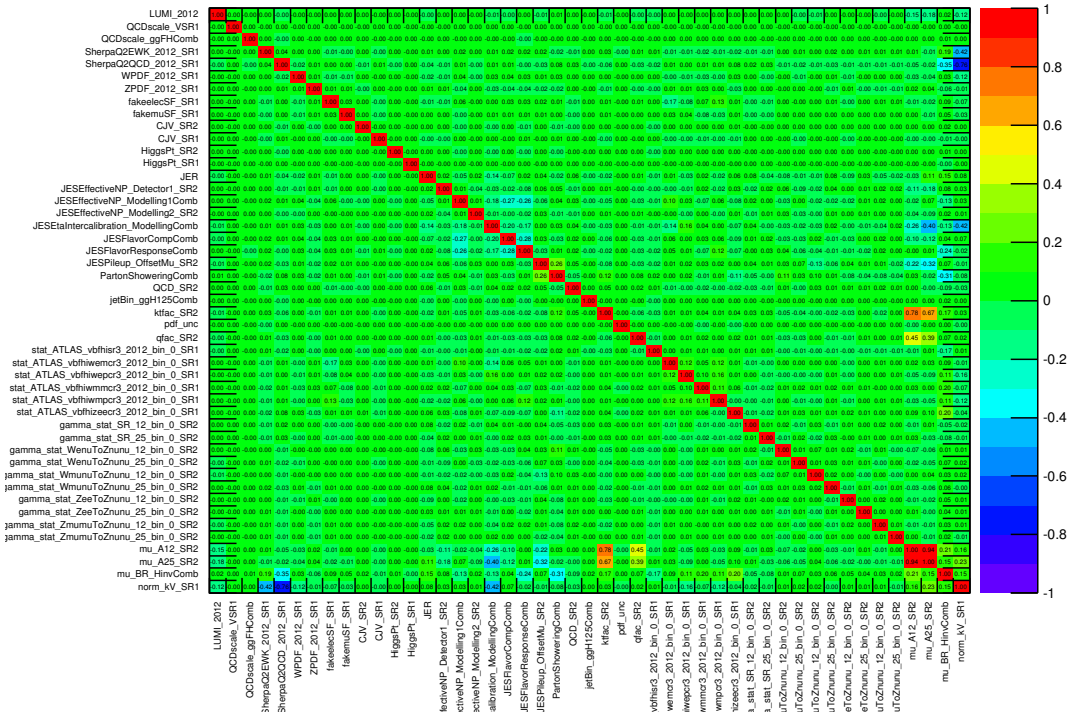

Figure 7.3: The correlations among the nuisance parameters and normalization factors in the fit performed in the combination of searches for invisible Higgs boson decays.

7.3 Model Interpretation

In the Higgs-portal dark matter scenario, a dark sector is coupled to the SM via the Higgs boson [7,8] by introducing a WIMP dark matter singlet that only couples to the SM Higgs doublet. In this model, assuming that the dark matter particle is lighter than half of the Higgs boson mass, one would search for Higgs boson decays to undetected (invisible) dark matter particles, e.g. $H \to \chi\chi$. The upper limits on the branching ratio to invisible particles directly define the maximum allowed decay width to the invisible particles

$$\Gamma^{\text{hinv}} = \frac{\text{BR}(H \to \text{ invisible})}{1 - \text{BR}(H \to \text{ invisible})} \times \Gamma_H, \tag{7.3}$$

where Γ_H is the total decay width of the Higgs boson. Adopting the formulas from Ref. [8], the decay width of the Higgs boson to the invisible particles can be written as

$$\Gamma^{\text{inv}}_{H\to SS} = \frac{\lambda^2_{HSS} v^2 \beta_S}{64\pi m_H}, \tag{7.4}$$

$$\Gamma^{\text{inv}}_{H\to VV} = \frac{\lambda^2_{HVV} v^2 m_H^3 \beta_V}{256\pi m_V^4}\left(1 - 4\frac{m_V^2}{m_H^2} + 12\frac{m_V^4}{m_H^4}\right), \tag{7.5}$$

$$\Gamma^{\text{inv}}_{H\to ff} = \frac{\lambda^2_{Hff} v^2 m_H \beta_f^3}{32\pi\Lambda^2}, \tag{7.6}$$

for the scalar, vector and Majorana fermion Dark Matter, respectively. The parameters λ_{HSS}, λ_{HVV}, λ_{Hff}/Λ are the corresponding coupling constants, v is the vacuum expectation value of the SM Higgs doublet, m_χ ($\chi = S$, V, f) is the dark matter particle mass and $\beta_\chi = \sqrt{1 - 4m_\chi^2/m_H^2}$. Furthermore, one can also write the spin-independent WIMP-nucleon cross sections for all three cases as

$$\sigma^{SI}_{SN} = \frac{\lambda^2_{HSS}}{16\pi m_H^4}\frac{m_N^4 f_N^2}{(m_S + m_N)^2}, \tag{7.7}$$

$$\sigma^{SI}_{VN} = \frac{\lambda^2_{HVV}}{16\pi m_H^4}\frac{m_N^4 f_N^2}{(m_V + m_N)^2}, \tag{7.8}$$

$$\sigma^{SI}_{fN} = \frac{\lambda^2_{Hff}}{4\pi\Lambda^2 m_H^4}\frac{m_N^4 m_f^2 f_N^2}{(m_f + m_N)^2}, \tag{7.9}$$

$$\tag{7.10}$$

where m_N is the nucleon mass and f_N parametrizes the Higgs-nucleon coupling. The numerical values for all the parameters in the equations above are given in Table 7.2.

In the project of "Constraints on New Phenomena via Higgs Boson Couplings and Invisible Decays with the ATLAS Detector" [12], the combination of the visible

Table 7.2: Parameters in the Higgs-portal dark-matter model.

Vacuum expectation value	$v/\sqrt{2}$	174 GeV
Higgs boson mass	m_H	125 GeV
Higgs boson width	Γ_H	4.07 MeV
Nucleon mass	m_N	939 MeV
Higgs–nucleon coupling form factor	f_N	$0.33^{+0.30}_{-0.07}$

and invisible Higgs boson decay channels was performed and resulted the limit on $BR(h \to invisible)$ at 95% CL of 0.23. The result is very close to the mentioned result in Section 7.2 of 0.25. To compare with these direct searches for DM, the observed upper limit combining all the visible and invisible Higgs boson decay channels is calculated at the 90% CL: this gives $BR(h \to invisible) < 0.22$. It is translated into the upper bound on the scattering cross section between nucleons and dark matter, are shown in Fig. 7.4 compared to the results from direct detection experiments. The WIMP-nucleon cross section limits resulting from searches for invisible Higgs boson decays extend from low WIMP mass to half the Higgs boson mass, and are complementary to the results provided by direct detection experiments that have limited sensitivity to WIMP particles with mass at the order of 1 GeV and lower [26, 28–32, 34].

For all three scenarios, the ATLAS limits are stronger than the exclusion limits by the direct detection experiments for $M_{WIMP} \lesssim 10$ GeV. This is expected as the LHC has no limitations for the production of low mass particles, whereas the recoil energies produced in the interactions of sub-relativistic WIMP particles with nuclei in an apparatus of a direct detection experiment are often below the sensitivity threshold for light WIMP masses. Both fermion and vector WIMP in the Higgs-portal scenario give stronger limits than the limits by LUX [30]. In case of the scalar dark matter, the LUX results are more stringent than the Higgs portal limits for $M_{WIMP} \gtrsim 10$ GeV.

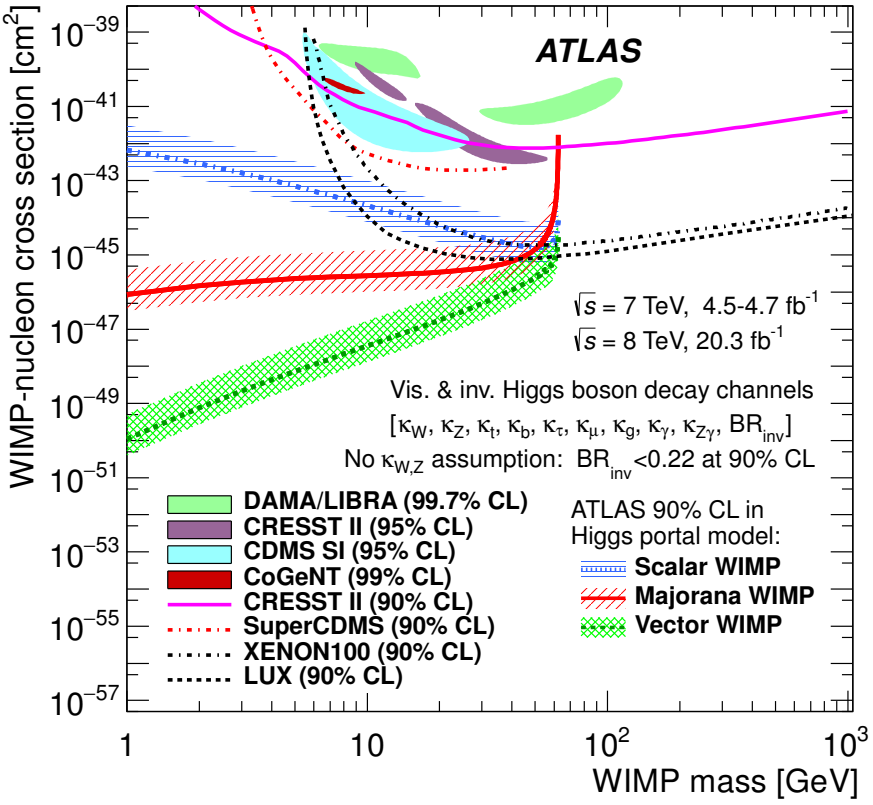

Figure 7.4: ATLAS upper limit at the 90% CL on the WIMP–nucleon scattering cross section in a Higgs portal model as a function of the mass of the dark-matter particle, shown separately for a scalar, Majorana fermion, or vector-boson WIMP. It is determined using the limit at the 90% CL of $\mathrm{BR_{inv}} < 0.22$ derived using both the visible and invisible Higgs boson decay channels. The hashed bands indicate the uncertainty resulting from varying the form factor f_N by its uncertainty. Excluded and allowed regions from direct detection experiments at the confidence levels indicated are also shown [26, 28, 30, 31, 33, 34, 112–114]. These are spin-independent results obtained directly from searches for nuclei recoils from elastic scattering of WIMPs, rather than being inferred indirectly through Higgs boson exchange in the Higgs portal model.

Chapter 8

Conclusions

A search for Higgs boson decays to invisible particles has been presented. The search uses data events with two forward jets and large missing transverse momentum, collected with the ATLAS detector at $\sqrt{s} = 8$ TeV at the LHC. Assuming the SM production cross section, acceptance and efficiency of 125 GeV mass Higgs boson, a 95% CL upper bound is set on the BR($H \rightarrow$ invisible) at 0.28. The results are interpreted in the Higgs portal dark matter model where the 90% CL limit on the BR($H \rightarrow$ invisible) is converted into upper bounds on the WIMP-nucleon scattering cross section as function of the WIMP mass, and compared to results from the direct dark matter detection experiments.

In addition to that, the combination of all direct searches for Higgs boson decays to invisible particles is done. The results are based on up to 4.8 fb^{-1} of pp collision data at $\sqrt{s} = 7$ TeV and 20.3 fb^{-1} at $\sqrt{s} = 8$ TeV recorded by the ATLAS experiment at the LHC. Direct searches for invisible Higgs boson decays in the VBF, $Z(\ell\ell)H$, and $V(jj)H$ production modes have been combined to set an upper bound on the Higgs boson invisible branching ratio of 0.25.

The LHC started its Run II at 13 TeV centre-of-mass energy with stable beam on June 3rd, 2015. Run II promises to provide a high amount of integrated luminosity (100 fb^{-1} then 300 fb^{-1}) of data. That can allow us to eventually see a significant number of beyond SM events where the Higgs bosons decay into invisible particles if the process really exists in nature. Otherwise it can help us to set more stringent limit on the BR($H \rightarrow$ invisible). Moreover, a large amount of different beyond SM searches and precision measurements will be performed at the LHC with the expectation of seeing something new and obtaining more precise measurements.

Bibliography

[1] D. Clowe *et al.*, *A direct empirical proof of the existence of dark matter*, Astrophys.J. **648** (2006) L109–L113, arXiv:astro-ph/0608407 [astro-ph].

[2] ATLAS Collaboration, *Observation of a new particle in the search for the standard model Higgs boson with the ATLAS detector at the LHC*, Phys. Lett. **B716** (2012) 1–29, arXiv:1207.7214 [hep-ex].

[3] CMS Collaboration, *Observation of a new boson at a mass of 125 GeV with the CMS experiment at the LHC*, Phys. Lett. **B716** (2012) 30–61, arXiv:1207.7235 [hep-ex].

[4] I. Antoniadis, M. Tuckmantel, and F. Zwirner, *Phenomenology of a leptonic goldstino and invisible Higgs boson decays*, Nucl.Phys. **B707** (2005) 215–232, arXiv:hep-ph/0410165 [hep-ph].

[5] N. Arkani-Hamed, S. Dimopoulos, G. Dvali, and J. March-Russell, *Neutrino masses from large extra dimensions*, Phys.Rev. **D65** (2002) 024032, arXiv:hep-ph/9811448 [hep-ph].

[6] A. Datta, K. Huitu, J. Laamanen, and B. Mukhopadhyaya, *Invisible Higgs in theories of large extra dimensions*, Phys.Rev. **D70** (2004) 075003, arXiv:hep-ph/0404056 [hep-ph].

[7] S. Kanemura, S. Matsumoto, T. Nabeshima, and N. Okada, *Can WIMP Dark Matter overcome the Nightmare Scenario?*, Phys.Rev. **D82** (2010) 055026, arXiv:1005.5651 [hep-ph].

[8] A. Djouadi, O. Lebedev, Y. Mambrini, and J. Quevillon, *Implications of LHC searches for Higgs–portal dark matter*, Phys.Lett. **B709** (2012) 65–69, arXiv:1112.3299 [hep-ph].

[9] LHC Higgs cross section working group, S. Dittmaier, C. Mariotti, G. Passarino, and R. Tanaka (Eds.), *Handbook of LHC Higgs cross sections: 1. Inclusive observables*, 2011. arXiv:1101.0593 [hep-ph], https://cds.cern.ch/record/1318996. CERN-2011-002.

[10] LHC Higgs cross section working group, S. Dittmaier, C. Mariotti, G. Passarino, and R. Tanaka (Eds.), *Handbook of LHC Higgs Cross Sections: 2. Differential distributions*, 2012. arXiv:1201.3084 [hep-ph], https://cds.cern.ch/record/1416519. CERN-2012-002.

[11] ATLAS Collaboration, G. Aad et al., *Search for invisible decays of a Higgs boson using vector-boson fusion in pp collisions at $\sqrt{s} = 8$ TeV with the ATLAS detector*, arXiv:1508.07869 [hep-ex].

[12] ATLAS Collaboration, G. Aad et al., *Constraints on new phenomena via Higgs boson couplings and invisible decays with the ATLAS detector*, arXiv:1509.00672 [hep-ex].

[13] ATLAS Collaboration, *The ATLAS experiment at the CERN Large Hadron Collider*, JINST **3** (2008) S08003.

[14] CMS Collaboration, *Search for invisible decays of Higgs bosons in the vector boson fusion and associated ZH production modes*, Eur.Phys.J. **C74** (2014) 2980, arXiv:1404.1344 [hep-ex].

[15] ATLAS Collaboration, *Search for Invisible Decays of a Higgs Boson Produced in Association with a Z Boson in ATLAS*, arXiv:1402.3244 [hep-ex].

[16] ATLAS Collaboration, *Search for invisible decays of the Higgs boson produced in association with a hadronically decaying vector boson in pp collisions at $\sqrt{s} = 8$ TeV with the ATLAS detector*, arXiv:1504.04324 [hep-ex].

[17] ATLAS Collaboration, *Search for new phenomena in final states with an energetic jet and large missing transverse momentum in pp collisions at $\sqrt{s} = 8$ TeV with the ATLAS detector*, arXiv:1502.01518 [hep-ex]. http://cds.cern.ch/record/1985260.

[18] CMS Collaboration, *Search for dark matter, extra dimensions, and unparticles in monojet events in proton-proton collisions at $\sqrt{s} = 8$ TeV*, arXiv:1408.3583 [hep-ex].

[19] ATLAS Collaboration, *Search for dark matter in events with a hadronically decaying W or Z boson and missing transverse momentum in pp collisions at 8 TeV with the ATLAS detector*, Phys. Rev. Lett. **112** (2014) 041802, arXiv:1309.4017 [hep-ex].

[20] A. Djouadi, A. Falkowski, Y. Mambrini, and J. Quevillon, *Direct Detection of Higgs-Portal Dark Matter at the LHC*, Eur.Phys.J. **C73** (2013) no. 6, 2455, arXiv:1205.3169 [hep-ph].

[21] ATLAS Collaboration, *Updated coupling measurements of the Higgs boson with the ATLAS detector using up to 25 fb^{-1} of proton-proton collision data*, ATLAS-CONF-2014-009 (2014) . https://cds.cern.ch/record/1670012.

[22] CMS Collaboration, *Precise determination of the mass of the Higgs boson and tests of compatibility of its couplings with the standard model predictions using proton collisions at 7 and 8 TeV*, arXiv:1412.8662 [hep-ex].

[23] G. Cowan, K. Cranmer, E. Gross, and O. Vitells, *Asymptotic formulae for likelihood-based tests of new physics*, European Physical Journal C **71** (2011) 1554, arXiv:1007.1727 [physics.data-an].

[24] B. Patt and F. Wilczek, *Higgs-field portal into hidden sectors*, arXiv:hep-ph/0605188.

[25] P. J. Fox, R. Harnik, J. Kopp, and Y. Tsai, *Missing Energy Signatures of Dark Matter at the LHC*, arXiv:1109.4398 [hep-ph].

[26] CRESST-II Collaboration, *Results on low mass WIMPs using an upgraded CRESST-II detector*, Eur.Phys.J. **C74** (2014) no. 12, 3184, arXiv:1407.3146 [astro-ph.CO].

[27] SuperCDMS Collaboration, R. Agnese et al., *Search for Low-Mass Weakly Interacting Massive Particles Using Voltage-Assisted Calorimetric Ionization Detection in the SuperCDMS Experiment*, Phys.Rev.Lett. **112** (2014) no. 4, 041302, arXiv:1309.3259 [physics.ins-det].

[28] SuperCDMS Collaboration, *Search for Low-Mass Weakly Interacting Massive Particles with SuperCDMS*, Phys.Rev.Lett. **112** (2014) no. 24, 241302, arXiv:1402.7137 [hep-ex].

[29] XENON100 Collaboration, *Limits on spin-dependent WIMP-nucleon cross sections from 225 live days of XENON100 data*, Phys.Rev.Lett. **111** (2013) no. 2, 021301, arXiv:1301.6620 [astro-ph.CO].

[30] LUX Collaboration, *First results from the LUX dark matter experiment at the Sanford Underground Research Facility*, Phys.Rev.Lett. **112** (2014) 091303, arXiv:1310.8214 [astro-ph.CO].

[31] DAMA Collaboration, *First results from DAMA/LIBRA and the combined results with DAMA/NaI*, Eur.Phys.J. **C56** (2008) 333–355, arXiv:0804.2741 [astro-ph].

[32] C. E. Aalseth *et al.*, *Maximum Likelihood Signal Extraction Method Applied to 3.4 years of CoGeNT Data*, arXiv:1401.6234 [astro-ph.CO].

[33] G. Angloher *et al.*, *Results from 730 kg days of the CRESST-II Dark Matter Search*, Eur.Phys.J. **C72** (2012) 1971, arXiv:1109.0702 [astro-ph.CO].

[34] CDMS Collaboration, CDMS Collaboration, *Silicon Detector Dark Matter Results from the Final Exposure of CDMS II*, Phys.Rev.Lett. **111** (2013) 251301, arXiv:1304.4279 [hep-ex].

[35] ATLAS Collaboration, *Search for Invisible Decays of a Higgs Boson Produced in Association with a Z Boson in ATLAS*, Phys.Rev.Lett. **112** (2014) 201802, arXiv:1402.3244 [hep-ex].

[36] UA1 Collaboration, G. Arnison et al., *Experimental Observation of Isolated Large Transverse Energy Electrons with Associated Missing Energy at s**(1/2) = 540-GeV*, Phys. Lett. **B122** (1983) 103–116.

[37] UA2 Collaboration, M. Banner et al., *Observation of Single Isolated Electrons of High Transverse Momentum in Events with Missing Transverse Energy at the CERN anti-p p Collider*, Phys. Lett. **B122** (1983) 476–485.

[38] UA1 Collaboration, G. Arnison et al., *Experimental Observation of Lepton Pairs of Invariant Mass Around 95-GeV/c**2 at the CERN SPS Collider*, Phys. Lett. **B126** (1983) 398–410.

[39] CDF Collaboration, F. Abe et al., *Observation of top quark production in $\bar{p}p$ collisions*, Phys. Rev. Lett. **74** (1995) 2626–2631, arXiv:hep-ex/9503002 [hep-ex].

[40] ATLAS Collaboration, G. Aad et al., *Observation of a new particle in the search for the Standard Model Higgs boson with the ATLAS detector at the LHC*, Phys. Lett. **B716** (2012) 1–29, arXiv:1207.7214 [hep-ex].

[41] CMS Collaboration, S. Chatrchyan et al., *Observation of a new boson at a mass of 125 GeV with the CMS experiment at the LHC*, Phys. Lett. **B716** (2012) 30–61, arXiv:1207.7235 [hep-ex].

[42] ATLAS Collaboration, *The ATLAS Experiment at the CERN Large Hadron Collider*, JINST **3** (2008) S08003.

[43] K. O. et al. (Particle Data Group) Chin. Phys. C **38** (2014) 090001.

[44] J. W. H. J. M. Campbell and W. J. Stirling, *Hard Interactions of Quarks and Gluons: A Primer for LHC Physics*, Rept. Prog. Phys. **70** (2007) 89.

[45] A. Djouadi, *The anatomy of electro-weak symmetry breaking. I: The Higgs boson in the Standard Model*, Phys. Rept. **457** (2008) 1.

[46] LHC Higgs Cross Section Working Group Collaboration, LHC Higgs cross section working group, S. Dittmaier, C. Mariotti, G. Passarino, S. Heinemeyer, and R. Tanaka (Eds.), *Handbook of LHC Higgs Cross Sections: 3. Higgs Properties*, arXiv:1307.1347 [hep-ph].

[47] ATLAS Collaboration, *Study of the spin and parity of the Higgs boson in diboson decays with the ATLAS detector*, arXiv:1506.05669 [hep-ex].

[48] CMS Collaboration, *Constraints on the spin-parity and anomalous HVV couplings of the Higgs boson in proton collisions at 7 and 8 TeV*, arXiv:1411.3441 [hep-ex].

[49] ATLAS Collaboration, *Measurements of Higgs boson production and couplings in diboson final states with the ATLAS detector at the LHC*, Phys. Lett. **B 726** (2013) 88, arXiv:1307.1427 [hep-ex].

[50] ATLAS and CMS Collaborations, *Combined Measurement of the Higgs Boson Mass in pp Collisions at $\sqrt{s} = 7$ and 8 TeV with the ATLAS and CMS Experiments*, Phys. Rev. Lett. **114** (2015) 191803, arXiv:1503.07589 [hep-ex].

[51] ATLAS Collaboration, G. Aad et al., *Measurements of the Higgs boson production and decay rates and coupling strengths using pp collision data at $\sqrt{s} = 7$ and 8 TeV in the ATLAS experiment*, arXiv:1507.04548 [hep-ex].

[52] CMS Collaboration, *Precise determination of the mass of the Higgs boson and tests of compatibility of its couplings with the standard model predictions using proton collisions at 7 and 8 TeV*, Eur. Phys. J. **C75** (2015) no. 5, 212, arXiv:1412.8662 [hep-ex].

[53] CMS Collaboration, *Search for invisible decays of Higgs bosons in the vector boson fusion production mode*, Tech. Rep. CMS-PAS-HIG-14-038, 2015. https://cds.cern.ch/record/2007270/.

[54] CMS Collaboration, *Search for invisible decays of a Higgs produced in association with a Z boson*, Tech. Rep. CMS-PAS-HIG-13-018, CERN, Geneva, Jul, 2013. http://cds.cern.ch/record/1561758.

[55] ATLAS Collaboration, *Search for invisible decays of the Higgs boson produced in association with a hadronically decaying vector boson in pp collisions at $\sqrt{8}$ TeV with the ATLAS Detector*, arXiv:1504.04324 [hep-ex]. http://cds.cern.ch/record/2010107.

[56] ATLAS Collaboration, *Electron performance measurements with the ATLAS detector using the 2010 LHC proton-proton collision data*, Eur.Phys.J. **C72** (2012) 1909, arXiv:1110.3174 [hep-ex].

[57] ATLAS Collaboration, *Measurement of the muon reconstruction performance of the ATLAS detector using 2011 and 2012 LHC protonproton collision data*, Eur.Phys.J. **C74** (2014) no. 11, 3130, arXiv:1407.3935 [hep-ex].

[58] ATLAS Collaboration, *Identification and energy calibration of hadronically decaying tau leptons with the ATLAS experiment in pp collisions at $\sqrt{s}$=8 TeV*, arXiv:1412.7086 [hep-ex].

[59] M. Cacciari, G. P. Salam, and G. Soyez, *Anti-k_t Jet Clustering Algorithm*, JHEP **04** (2008) 063, arXiv:0802.1189 [hep-ex].

[60] ATLAS Collaboration, *Jet energy measurement and its systematic uncertainty in proton-proton collisions at $\sqrt{s} = 7$ TeV with the ATLAS detector*, Eur.Phys.J. **C75** (2015) no. 1, 17, arXiv:1406.0076 [hep-ex].

[61] ATLAS Collaboration, *Jet energy measurement with the ATLAS detector in proton-proton collisions at $\sqrt{s} = 7$ TeV*, Eur.Phys.J. **C73** (2013) 2304, arXiv:1112.6426 [hep-ex].

[62] ATLAS Collaboration, *Performance of Missing Transverse Momentum Reconstruction in ATLAS studied in Proton-Proton Collisions recorded in 2012 at 8 TeV*, ATLAS-CONF-2013-082 (2013) . https://cds.cern.ch/record/1570993.

[63] D. Ghosh, R. Godbole, M. Guchait, K. Mohan, and D. Sengupta, *Looking for an Invisible Higgs Signal at the LHC*, Phys.Lett. **B725** (2013) 344–351, arXiv:1211.7015 [hep-ph].

[64] GEANT4 Collaboration, *GEANT4: A simulation toolkit*, Nucl. Instrum. Meth. **A506** (2003) 250–303.

[65] Sjöstrand, Torbjorn and Mrenna, Stephen and Skands, Peter Z., *A brief introduction to PYTHIA 8.1*, Comput. Phys. Commun. **178** (2008) 852–867, arXiv:0710.3820 [hep-ph].

[66] P. Nason, *A new method for combining NLO QCD with shower Monte Carlo algorithms*, JHEP **11** (2004) 040, arXiv:hep-ph/0409146.

[67] S. Frixione, P. Nason, and C. Oleari, *Matching NLO QCD computations with parton shower simulations: the POWHEG method*, JHEP **11** (2007) 070, arXiv:0709.2092 [hep-ph].

[68] S. Alioli, P. Nason, C. Oleari, and E. Re, *A general framework for implementing NLO calculations in shower Monte Carlo programs: the POWHEG BOX*, JHEP **06** (2010) 043, arXiv:1002.2581 [hep-ph].

[69] S. Alioli, P. Nason, C. Oleari, and E. Re, *NLO Higgs boson production via gluon fusion matched with shower in POWHEG*, JHEP **04** (2009) 002, arXiv:0812.0578 [hep-ph].

[70] P. Nason and C. Oleari, *NLO Higgs boson production via vector-boson fusion matched with shower in POWHEG* [POWHEG-BOX r1655], JHEP **02** (2010) 037, arXiv:0911.5299 [hep-ph].

[71] E. Bagnaschi, G. Degrassi, P. Slavich, and A. Vicini, *Higgs production via gluon fusion in the POWHEG approach in the SM and in the MSSM*, JHEP **02** (2012) 088, arXiv:1111.2854 [hep-ph].

[72] H.-L. Lai et al., *New parton distributions for collider physics*, Phys.Rev. **D 82** (2010) 074024, arXiv:1007.2241 [hep-ph].

[73] M. Ciccolini, A. Denner, and S. Dittmaier, *Electroweak and QCD corrections to Higgs production via vector-boson fusion at the LHC*, Phys. Rev. D **77** (2003) 013002, arXiv:0710.4749 [hep-ex].

[74] ATLAS Collaboration, *Measurement of Higgs boson production in the diphoton decay channel in pp collisions at center-of-mass energies of 7 and 8 TeV with the ATLAS detector*, Phys.Rev. **D90** (2014) no. 11, 112015, arXiv:1408.7084 [hep-ex].

[75] ATLAS Collaboration, *Observation and measurement of Higgs boson decays to WW^* with the ATLAS detector*, arXiv:1412.2641 [hep-ex].

[76] K. Hamilton, P. Nason, and G. Zanderighi, *MINLO: Multi-Scale Improved NLO*, JHEP **1210** (2012) 155, arXiv:1206.3572 [hep-ph].

[77] D. de Florian, G. Ferrera, M. Grazzini, and D. Tommasini, *Transverse-momentum resummation: Higgs boson production at the Tevatron and the LHC*, JHEP **11** (2011) 064, arXiv:1109.2109 [hep-ph].

[78] T. Gleisberg *et al.*, *Event generation with SHERPA 1.1*, JHEP **02** (2009) 007, arXiv:0811.4622 [hep-ph].

[79] S. Höche, F. Krauss, S. Steffen, and F. Siegert, *QCD matrix elements and truncated showers*, JHEP **2009** (2009) no. 05, 053, arXiv:0903.1219.

[80] ATLAS Collaboration, *Measurement of the electroweak production of dijets in association with a Z-boson and distributions sensitive to vector boson fusion in proton-proton collisions at $\sqrt{s} = 8$ TeV using the ATLAS detector*, JHEP **1404** (2014) 031, arXiv:1401.7610 [hep-ex].

[81] K. Melnikov and F. Petriello, *Electroweak gauge boson production at hadron colliders through $O(\alpha(s)^2)$*, Phys. Rev. **D74** (2006) 114017, arXiv:hep-ph/0609070.

[82] C. Anastasiou, L. J. Dixon, K. Melnikov, and F. Petriello, *High precision QCD at hadron colliders: electroweak gauge boson rapidity distributions at NNLO*, Phys. Rev. **D69** (2004) 094008, arXiv:hep-ph/0312266 [hep-ph].

[83] K. Arnold *et al.*, *VBFNLO: a parton level Monte Carlo for processes with electroweak bosons*, Comput. Phys. Commun. **180** (2009) 1661–1670, arXiv:0811.4559 [hep-ph].

[84] S. Frixione, E. Laenen, P. Motylinski, and B. R. Webber, *Single-top production in MC@NLO*, JHEP **0603** (2006) 092, arXiv:hep-ph/0512250 [hep-ph].

[85] S. Frixione, E. Laenen, P. Motylinski, B. R. Webber, and C. D. White, *Single-top hadroproduction in association with a W boson*, JHEP **0807** (2008) 029, arXiv:0805.3067 [hep-ph].

[86] B. P. Kersevan and E. Richter-Was, *The Monte Carlo event generator AcerMC version 1.0 with interfaces to PYTHIA 6.2 and HERWIG 6.3*, Comput. Phys. Commun. **149** (2003) 142, arXiv:hep-ph/0201302 [hep-ph].

[87] ATLAS Collaboration, *ATLAS tunes of PYTHIA 6 and PYTHIA 8 for MC11*, ATLAS-PHYS-PUB-2011-009 (2011) . http://cdsweb.cern.ch/record/1363300.

[88] J. Pumplin et al., *New generation of parton distributions with uncertainties from global QCD analysis*, JHEP **0207** (2002) 012, arXiv:hep-ph/0201195 [hep-ph].

[89] M. Czakon and A. Mitov, *Top++: A Program for the Calculation of the Top-Pair Cross-Section at Hadron Colliders*, Comput. Phys. Commun. **185** (2014) 2930, arXiv:1112.5675 [hep-ph].

[90] M. Czakon, P. Fiedler, and A. Mitov, *Total Top-Quark Pair-Production Cross Section at Hadron Colliders Through $O(\frac{4}{S})$*, Phys. Rev. Lett. **110** (2013) 252004, arXiv:1303.6254 [hep-ph].

[91] N. Kidonakis, *Two-loop soft anomalous dimensions for single top quark associated production with a W- or H-*, Phys. Rev. **D 82** (2010) 054018, arXiv:1005.4451 [hep-ph].

[92] G. Corcella *et al.*, *HERWIG 6: An event generator for hadron emission reactions with interfering gluons (including supersymmetric processes)*, JHEP **01** (2001) 010, arXiv:hep-ph/0011363.

[93] J. Butterworth, J. Forshaw and M. Seymour, *Multiparton interactions in photoproduction at HERA*, Z. Phys. **C72** (1996) 637–646, arXiv:hep-ph/9601371.

[94] J. M. Campbell, R. K. Ellis, and C. Williams, *Vector boson pair production at the LHC*, JHEP **07** (2011) 018, arXiv:1105.0020 [hep-ph].

[95] ATLAS Collaboration, *Calibration of the performance of b-tagging for c and light-flavour jets in the 2012 ATLAS data*, ATLAS-CONF-2014-046 (2014) . https://cds.cern.ch/record/1741020.

[96] ATLAS Collaboration, *Search for squarks and gluinos with the ATLAS detector in final states with jets and missing transverse momentum using 4.7 fb^{-1} of $\sqrt{s} = 7$ TeV proton-proton collision data*, Phys.Rev. **D87** (2013) no. 1, 012008, arXiv:1208.0949 [hep-ex].

[97] ATLAS Collaboration, *Improved luminosity determination in pp collisions at $\sqrt(s) = 7$ TeV using the ATLAS detector at the LHC*, Eur.Phys.J. **C73** (2013) no. 8, 2518, arXiv:1302.4393 [hep-ex].

[98] M. Mangano *et al.*, *ALPGEN, a generator for hard multiparton processes in hadronic collisions*, J. High Energy Phys. **0307** (2003) 001, arXiv:hep-ph/0206293 [hep-ph].

[99] H.-L. Lai *et al.*, *New parton distributions for collider physics*, Phys. Rev. **D 82** (2010) 074024, arXiv:1007.2241 [hep-ph].

[100] I. W. Stewart and F. J. Tackmann, *Theory uncertainties for Higgs and other searches using jet bins*, Phys. Rev. **D85** (2012) 034011, arXiv:1107.2117 [hep-ph].

[101] A. L. Read, *Presentation of search results: The CL(s) technique*, J.Phys.G **G28** (2002) 2693–2704.

[102] ATLAS Collaboration, *Combined search for the Standard Model Higgs boson in pp collisions at $\sqrt{s}$=7 TeV with the ATLAS detector*, Phys. Rev. **D86** (2012) 032003, arXiv:1207.0319 [hep-ex].

[103] ATLAS and CMS Collaborations, *Procedure for the LHC Higgs boson search combination in Summer 2011*, ATL-PHYS-PUB-2011-011, CERN-CMS-NOTE-2011-005 (2011) . http://cdsweb.cern.ch/record/1375842.

[104] L. Moneta et al., *The RooStats project*, PoS **ACAT2010** (2010) 057, arXiv:1009.1003 [physics.data-an].

[105] K. Cranmer, G. Lewis, L. Moneta, A. Shibata, and W. Verkerke, *HistFactory: A tool for creating statistical models for use with RooFit and RooStats*, CERN-OPEN-2012-016 (Jan, 2012) . http://cdsweb.cern.ch/record/1456844.

[106] W. Verkerke and D. Kirkby, *The RooFit toolkit for data modelling*, arXiv:physics/0306116v1 [physics.data-an].

[107] G. Cowan, K. Cranmer, E. Gross, and O. Vitells, *Asymptotic formulae for likelihood-based tests of new physics*, Eur. Phys. J. **C71** (2011) 1554.

[108] ATLAS Collaboration, *Measurements of the Higgs boson production and decay rates and coupling strengths using pp collision data at $\sqrt{s}$ = 7 and 8 TeV in the ATLAS experiment*, ATLAS-CONF-2015-007 (2015) . https://cds.cern.ch/record/2002212. ***Placeholder for paper***.

[109] A.L. Read, *Presentation of search results: the CL_s technique*, J. Phys. G **28** (2002) 2693.

[110] ATLAS Collaboration, *Search for an Invisibly Decaying Higgs Boson Produced via Vector Boson Fusion using ATLAS detector*, ATLAS-CONF-2015-004 (2015) . http://cds.cern.ch/record/1993851.

[111] ATLAS Collaboration, *Search for dark matter in events with a hadronically decaying W or Z boson and missing transverse momentum in pp collisions at $\sqrt{s}$=8 TeV with the ATLAS detector*, Phys. Rev. Lett. **112** (2014) 041802, arXiv:1309.4017 [hep-ex].

[112] J. Angle et al., *A search for light dark matter in XENON10 data*, Phys. Rev. Lett. **107** (2011) 051301, arXiv:1104.3088 [astro-ph.CO].

[113] E. Aprile et al., *Dark Matter Results from 225 Live Days of XENON100 Data*, Phys. Rev. Lett. **109** (2012) 181301, arXiv:1207.5988 [astro-ph.CO].

[114] C. Aalseth et al., *Search for an Annual Modulation in a P-type Point Contact Germanium Dark Matter Detector*, Phys. Rev. Lett. **107** (2011) 141301, arXiv:1106.0650 [astro-ph.CO].